

Biomass-Derived Boron Carbide Nanowires: Growth Mechanisms, Properties, and Applications

A Dissertation

Submitted to

the Faculty of the School of Engineering and Applied Science

University of Virginia

In Partial Fulfillment

of the Requirements for the Degree

of

Doctor of Philosophy

By

Ningning Song

August 2019

Approval Sheet

This Dissertation is submitted in partial fulfillment of the requirements

for the degree of

Doctor of Philosophy

Ningning Song, Author

This dissertation has been read and approved by the examining Committee:

Xiaodong (Chris) Li, Advisor

Baoxing Xu, Committee Chair

Esfarjani, Keivan, Committee Member

Green, David L., Committee Member

Zhou, Bicheng, Committee Member

Accepted for the School of Engineering and Applied Science:

Craig H. Benson, Dean

School of Engineering and Applied Science

August 2019

Dedicated to my parents Min and Guoquan, and my beloved husband Naidi,

for their unfaltering support and unconditional love

Acknowledgements

I consider myself very fortunate to have had Prof. Xiaodong (Chris) Li as my advisor for his constant mentorship throughout my PhD journey. His continuous guidance and encouragement have been a major driving force behind this thesis. His infectious enthusiasm for scientific research will continue to inspire me in my future career. I would also like to express my deepest appreciation to other committee members, Prof. Keivan Esfarjani, Prof. David L. Green, Prof. Baoxing Xu and Prof. Bicheng Zhou for their valuable time to guide and support my dissertation work.

I would also like to thank all the members of Prof. Li's lab past and present for their supports, encouragements, and friendships, including Jamison Bartlett, Kenny Brown, Clifton Bumgardner, Diana Burden, Ruoxi Chen, Jianchao Chen, Dr. Brendan Croom, Tyler Daspit, Dr. Zan Gao, Oliver Hammond, Jiajun He, Michael Heim, Alex Jarama, Dr. Dalai Jin, Dr. Haoze Li, Dr. Guojun Ma, Dr. Yellapu Murty, David Roache, Yosyp Schwab, Victor Shen, Dr. Yong Sun, Dr. Yang Sun, Dr. Yingchao Yang, Yunya Zhang, Dr. Liwen Zhang, Yucheng Zhou, Dr. Jiadeng Zhu, *et al.* It has been a great pleasure to be a part of such a dynamic and friendly group of people. In particular, Dr. Yingchao Yang has been very helpful with easing my transition to PhD life. Dr. Gao Zan has always been very supportive for my electrochemistry studies.

This dissertation study would not be possible without financial supports from the U.S. National Science Foundation (NSF) CMMI-1418696, CMMI-1537021, and CMMI-1728042.

Lastly, I dedicate my thesis to my family. Thanks to my parents Min and Guoquan who always love me unconditionally, and constantly support me of all my choices. I would also like to give my special thanks to my beloved husband Naidi for his support, his encouragement and his love. He is my best friend, my happy place, and my everything.

Abstract

Boron carbide, one of the third hardest materials known in nature, is distinguished from other materials by its appealing physical and mechanical properties. Particularly, boron carbide at reduced dimensions, especially one-dimensional, often exhibits novel properties such as large specific surface area and high mechanical strength close to its theoretical value. These properties make the boron carbide nanowire a promising material for numerous applications, such as high-strength lightweight material applications in which they are exposed to extreme chemical and thermal conditions, including applications in thermo-electric energy conversion systems, neutron absorbers, and ceramic armors. To date, however, the growth mechanisms of boron carbide nanowires remain, to a large extent, unknown due to the complex crystal structure and widely varied composition of boron carbide. The lack of knowledge of boron carbide nanowire growth mechanisms largely hinders the development of nanowire synthesis techniques and increases the production cost. Furthermore, the outstanding mechanical properties make the multiscale structural design and hierarchical morphology control of boron carbide difficult, thereby restricting the exploration of boron carbide nanowire-based novel devices.

This dissertation studies the growth mechanism, properties, and applications of biomass-derived boron carbide nanowires. Specifically, in Chapter 2, it is demonstrated that the transformation between polytypic boron carbide phases promotes boron migration in the nanowire growth. An atomistic mass transport model was developed to explain such volume-diffusion-induced nanowire growth which cannot be explained by the conventional surface diffusion model alone. With the proposed growth mechanism, various biomass materials were explored as raw materials to synthesize boron carbide nanowires. In

Chapter 3, we report that shear-mixing enabled graphene wrapped B₄C nanowires (graphene@B₄C-NWs) empowered exceptional dispersion of nanowires in polymer matrix and superlative nanowire-matrix bonding. The graphene@B₄C-NW reinforced epoxy composites exhibited simultaneous enhancements in strength, elastic modulus, and ductility. Tailoring the composite interfaces with graphene enabled effective utilization of the nano-fillers, resulting in 2 times increase in load transfer efficiency. Molecular dynamics simulations unlocked the shear-mixing graphene/nanowire self-assembly mechanism. In Chapter 4, we demonstrate multiscale structural design and hierarchical morphology control of boron carbide. A new type of micro/nano hybrid filler was synthesized by an unconventional cotton aided method, which has boron carbide microplatelet as the core and radially aligned boron carbide nanowires as the shell. Such multiscale reinforcement design remarkably enhanced the load carrying efficiency of boron carbide. In Chapter 5, an unusual cathode configuration for lithium-sulfur (Li-S) batteries was constructed, employing boron carbide nanowires (BC-NWs) as a skeleton, porous activated textile (ACT) as a flexible carbon scaffold, and reduced graphene oxide (rGO) as a self-adaptive protective shell. This BC-NW@ACT/S/rGO cathode achieved superlative sulfur confinement and exceptional electrochemical performance. These findings significantly advance our understanding of biomass-derived boron carbide nanowire growth processes and provide new guidelines for the design of nanowire-structured composites and energy storage devices.

Table of content

| | |
|---|-------------|
| Acknowledgements | i |
| Abstract | ii |
| Table of content | iv |
| List of Figures | viii |
| List of Tables | xv |
| Chapter 1 Introduction | 1 |
| 1.1 Background and motivation | 1 |
| 1.2 Overview of boron carbide..... | 4 |
| 1.3 Synthesis and properties of boron carbide nanowires | 6 |
| 1.4 Overview of the dissertation..... | 9 |
| Reference..... | 11 |
| Chapter 2 Polytype transformation assisted growth mechanism in boron carbide nanowires | 18 |
| 2.1 Introduction | 18 |
| 2.2 Lattice distortion measurements in boron carbide nanowires | 19 |
| 2.2.1 Experimental methods | 19 |
| 2.2.2 Results and discussion..... | 21 |
| 2.3 Polytypic boron carbide transformation in nanowires..... | 25 |
| 2.4 Polytypic phase transformation enabled boron carbide nanowire growth..... | 29 |

| | |
|--|----|
| 2.4.1 Surface-diffusion induced nanowire growth | 29 |
| 2.4.2 Volume-diffusion induced nanowire growth..... | 31 |
| 2.5 Biomass-derived boron carbide nanowire growth..... | 37 |
| 2.5.1 Experimental methods | 37 |
| 2.5.2 Results and discussion | 38 |
| 2.6 Conclusion..... | 43 |
| Reference..... | 45 |

Chapter 3 Tailoring nanocomposite interfaces with graphene to achieve high strength and toughness..... 49

| | |
|---|----|
| 3.1 Introduction | 49 |
| 3.2 Synthesis and characterizations of graphene@B ₄ C-NWs | 50 |
| 3.2.1 Experimental methods | 50 |
| 3.2.2 Results and discussion..... | 51 |
| 3.3 Mechanical characterizations of graphene@B ₄ C-NW composites | 57 |
| 3.3.1 Experimental methods | 57 |
| 3.3.2 Results and discussion..... | 58 |
| 3.4 Role of graphene as the tailoring agent of nano-fillers..... | 65 |
| 3.4.1 Methods | 65 |
| 3.4.2 Results and discussion..... | 67 |
| 3.5 Conclusion..... | 69 |
| Reference..... | 70 |

| | |
|---|------------|
| Chapter 4 Bioinspired, multiscale boron carbide filler reinforced composites..... | 73 |
| 4.1 Introduction | 73 |
| 4.2 Multiscale boron carbide nano-filler fabrication and surface functionalization | 75 |
| 4.2.1 Experimental methods | 75 |
| 4.2.2 Results and discussion | 76 |
| 4.3 Mechanical characterizations of boron carbide nano-filler reinforced composites | 80 |
| 4.3.1 Experimental methods | 80 |
| 4.3.2 Results and discussion | 81 |
| 4.4 Continuum mechanics study of multiscale reinforcements | 88 |
| 4.5 Conclusion | 98 |
| Reference | 100 |
| Chapter 5 Boron carbide nanoskeleton enabled, flexible lithium-sulfur batteries..... | 104 |
| 5.1 Introduction | 104 |
| 5.2 Synthesis and characterization of the electrode nanocomposite..... | 106 |
| 5.2.1 Experimental methods | 106 |
| 5.2.2 Results and discussion | 109 |
| 5.3 Battery assembly and electrochemical testing | 114 |
| 5.3.1 Experimental methods | 114 |
| 5.3.2 Results and discussion | 115 |
| 5.4 Role of BC-NWs and rGO in Li-S cell..... | 120 |
| 5.4.1 Methods | 120 |

| | |
|--|------------|
| 5.4.2 Results and discussion..... | 123 |
| 5.5 Flexible lithium-sulfur batteries with BC-NWs@ACT/S/rGO cathode..... | 127 |
| 5.6 Conclusion..... | 129 |
| Reference..... | 131 |
| Chapter 6 Summary and suggestions..... | 137 |
| 6.1 Summary of contributions and significance..... | 137 |
| 6.2 Suggestions for future research..... | 140 |
| Reference..... | 143 |

List of Figures

Fig. 1.1. Basic types of large-scale nanomaterials bulk forms. The filler materials, whether 0-D, 1-D, or 2-D nanomaterials are used to make film and bulk nanocomposites. Reprinted from Ashby *et al.* [4]

Fig. 1.2. Boron carbide lattice showing correlation between the rhombohedral (red) and the hexagonal (blue) unit cells. Inequivalent lattice sites are marked by arrows. Reprinted from Domnich *et al.* [34]

Fig. 1.3. Growth of 1D structures by VLS mechanism. Reprinted from Wagner *et al.* [75]

Fig. 2.1. Procedure of exploring input data for DIC calculation. (a) Ideal simulated HRTEM image of boron carbide with [010] as zone axis. (b) HRTEM image of boron carbide nanowires. (c-d) Atomic arrangements were extracted from (a) and (c) by morphological method, respectively. (e-f) Dotted patterns were created according to (c) and (d).

Fig. 2.2. Structural and chemical characterization of boron carbide nanowires. (a) SEM image and TEM image inset, showing the typical morphology of boron carbide nanowires. (b) XRD pattern of boron carbide nanowires, in good agreement with B₄C JCPDS No. 6-0555. (c) EELS pattern, showing that the nanowire is of composition B₁C_{0.29±0.041}, the inset shows the EELS elemental maps of boron (green), carbon (red) and nickel (blue). (d) Variation of composition in the boron carbide nanowire determined by EELS line profile along the length of the wire.

Fig. 2.3. Simulation by the multislice method (JEMS). (a) Atomic arrangement of the boron carbide super-cell, viewed down [010]; (b) A through-focal series of HRTEM contrast images with 10 nm defocus steps.

Fig. 2.4. HRTEM inspection and lattice distortion characterizations of boron carbide nanowires. (a) HRTEM image and corresponding FFT pattern of a boron carbide nanowire. (b) Close-up observation and the Bloch wave method (JEMS) simulated image of the nanowire. (c) Lattice strain fields obtained by DIC at the top and bottom regions of the nanowire, respectively. (d) Statistics of the interplanar spacing distribution around various regions of the nanowire.

Fig. 2.5. Interplanar spacing map obtained by DIC along axial direction of nanowire.

Fig. 2.6. The rhombohedral unit cell of boron carbide lattice contains polar sites (pink), equatorial sites (blue) and chain sites (gray).

Fig. 2.7. (a) Formation enthalpy of selected boron carbide polytypes at 0K calculated using first principles method. (b) Comparison of measured interplanar spacings with theoretical values.

Fig. 2.8. Schematic diagram depicting the model of surface diffusion during nanowire growth.

Fig. 2.9. (a) Energy pathways and (b) schematic diagrams of boron migrations through surface diffusion (D mode) and polytypes transformation (T mode).

Fig. 2.10. (a) Schematic diagram of VLS based volumetric mass transport in boron carbide nanowire growth. (b) Correlation between the growth rate and radius of nanowires, calculated using the kinetic model with different boron migration modes; the theoretical models are fitted to the experimental data.

Fig. 2.11. Digital images of biomass resources, including cotton, flour, corn silk, paper towel, and fallen leaf.

Fig. 2.12. SEM characterizations showing the morphology of boron carbide nanowires synthesized from biomass resources, including (a) cotton, (b) flour, (c) corn silk, (d) paper towel, and (e) fallen leaf. (f) XRD pattern of boron carbide nanowires, in good agreement with B₄C JCPDS No. 6-0555.

Fig. 2.13. Nickel nanoparticles, uniformly distributed on cotton textile, were characterized using (a-c) SEM under different magnifications and (d) XRD.

Fig. 2.14. (a) Schematic illustrations of samples treatments and arrangements in the tube furnace, and red and blue colors represent boron and nickel, respectively. (b) and (c) SEM images of B@Cotton samples. (d) XRD pattern of B@Cotton samples. (e) and (f) SEM images of Ni@Cotton samples. (g) XRD pattern of Ni@Cotton samples.

Fig. 2.15. Schematic illustrations of the process of biomass derived boron carbide nanowire growth.

Fig. 3.1. Schematic illustration of the synthesis process of graphene@B₄C-NWs nanofillers.

Fig. 3.2. Synthesis and characterizations of B₄C nanowires. (a) SEM image of B₄C nanowires grown on the carbon fiber cloth. (b) TEM image of an individual B₄C nanowire. (c) B 1s and (d) C 1s XPS spectra of B₄C nanowires.

Fig. 3.3. Synthesis of nano-fillers in dilute water by shear mixing. TEM images of (a) B₄C nanowires, (b) multi-layer graphene, and (c) graphene@B₄C-NWs. (d) Chronological digital photos of B₄C nanowires, graphene, and graphene@B₄C-NWs.

Fig. 3.4. Characterizations of graphene@B₄C-NWs. (a) TEM image, (b) XRD patterns, and (c) EELS of graphene@B₄C-NWs. (d) HRTEM image, (e) the corresponding FFT, and (f) background-corrected Raman spectra of the B₄C nanowires in graphene@B₄C-NWs. (g) HRTEM image, (h) the corresponding FFT, and (i) background-corrected Raman spectra of the monolayer graphene in graphene@B₄C-NWs.

Fig. 3.5. (a) Flexural stress-strain curves of epoxy and graphene@B₄C-NW reinforced composites. (b) Comparison of flexural strength, elastic modulus, and fracture strain for pure epoxy and graphene@B₄C-NW reinforced composites.

Fig. 3.6. (a) Flexural stress-strain curves of epoxy and B₄C nanowire reinforced composites. (b) Comparison of experimental measured and theoretically predicted elastic modulus.

Fig. 3.7. (a) Flexural stress-strain curves of epoxy and graphene reinforced composites. (b) Comparison of experimental measured and theoretically predicted elastic modulus.

Fig. 3.8. SEM images of the fracture surface of pure epoxy

Fig. 3.9. (a) SEM images of the fracture surface of graphene@B₄C-NW reinforced composites. (b) An epoxy covered graphene@B₄C NW protruded out from the composite fracture surface.

Fig. 3.10. Crack toughening mechanisms in graphene@B₄C-NW composites.

Fig. 3.11. (a) SEM images of the fracture surface of graphene reinforced composites. (b) Graphene agglomerations on the composite fracture surface.

Fig. 3.12. (a) SEM images of the fracture surface of B₄C nanowire reinforced composites. (b) B₄C

nanowire agglomerations on the composite fracture surface. (c) B₄C nanowires pulling out from the composite fracture surface.

Fig. 3.13. MD snapshots of the atomic configurations representing the process of wrapping graphene around the B₄C nanowire, and the initial structure for calculation the interaction energy.

Fig. 3.14. MD snapshots of the atomic configurations representing the process of aggregation of graphene sheets, and the initial structure for calculation the interaction energy of multi-layer graphene and B₄C nanowires.

Fig. 3.15. Interaction energy profiles between two nano-fillers (graphene/graphene, B₄C-NW/B₄C-NW, and graphene@B₄C-NW/ graphene@B₄C-NW).

Fig. 4.1. Schematic illustration of the synthesis details of B₄C nanowire/carbon fiber hybrid structure.

Fig. 4.2. (a) SEM image of the morphology of B₄C micro-/nano-fillers synthesized on carbon fibers. (b) TEM image of B₄C nanowires. (c) XRD pattern of the as-synthesized B₄C micro-/nano-fillers on carbon fibers. (d) TEM image of B₄C micro-/nano-fillers. (e) HRTEM of B₄C micro-/nano-fillers. (f) EELS of B₄C micro-/nano-fillers.

Fig. 4.3. Schematic illustrating the typical B₄C microplatelet/nanowire hybrid fillers grown on the carbon fiber substrate.

Fig. 4.4. (a) TEM image of PANI functionalized B₄C micro-/nano-fillers. (b) HRTEM image of PANI functionalized B₄C micro-/nano-fillers. (c) Background-corrected Raman spectra of B₄C micro-/nano-fillers excited with a 514-nm wavelength laser line. (d) Polymerization process of PANI and complexation mechanism between PANI and B₄C.

Fig. 4.5. A representative high-contrast CBS SEM image taken during *in situ* tensile test.

Fig. 4.6. (a) Schematic showing the detailed processes for fabricating PANI functionalized B₄C micro-/nano-filler reinforced epoxy composites. (b-d) DIC strain maps of (b) pure epoxy, (c) unfunctionalized B₄C micro-/nano-filler reinforced composite, and (d) PANI functionalized B₄C micro-/nano-filler

reinforced composite. (e) Line profiles of the strains extracted from (b-d) along the tensile direction.

Fig. 4.7. (a) Samples for mechanical testing ((i) epoxy control sample, (ii) unfunctionalized B₄C micro-/nano-filler reinforced composite, (iii) PANI functionalized B₄C micro-/nano-filler reinforced composite). (b) SEM image of the fracture surface of pure epoxy resin. (c) and (e) SEM images of the fracture surface of unfunctionalized B₄C micro-/nano-filler reinforced composite. (d) and (f) SEM images of the fracture surface of PANI functionalized B₄C micro-/nano-filler reinforced composite.

Fig. 4.8. (a) AFM height image of the fracture surface of pure epoxy resin. (b) AFM height image of the fracture surface of unfunctionalized B₄C micro-/nano-filler reinforced composite. (c) SEM image showing pulling-out of B₄C micro-/nano-fillers in the PANI functionalized B₄C composite. (d) SEM image showing B₄C micro-/nano-filler bridging a crack in the PANI functionalized B₄C composite.

Fig. 4.9. Reinforcing effects of unfunctionalized and functionalized B₄C micro-/nano-fillers (a) Stress-strain curves of untreated B₄C micro-/nano-filler reinforced composites. (b) Stress-strain curves of PANI functionalized B₄C micro-/nano-filler reinforced composites. (c) and (d) Comparison of the mechanical properties of 1 wt.% B₄C composites with other typical polymer composites containing different reinforcements.

Fig. 4.10. Schematic diagram showing the cross section of the three-phase representative volume element (RVE) for the composites.

Fig. 4.11. Theoretically calculated normal strain distributions of the RVE for three cases: (a) pure epoxy, (b) Phase I is B₄C and Phase II is pure epoxy, and (c) Phase I is B₄C and Phase II is B₄C nanowire reinforced epoxy composite. Half of the strain distributions of the RVE is displayed, due to the symmetry.

Fig. 4.12. (a) Interfacial shear stress between Phase I and Phase II in B₄C micro-/nano-filler. (b) Average axial normal stress in Phase I.

Fig. 4.13. The effective length of B₄C fillers associated with different volume fractions of B₄C nanowires in Phase II.

Fig. 5.1. Thermogravimetric analysis (TGA) spectrum of the BC-NWs@ACT/S/rGO composite.

Fig. 5.2. (a) Schematic illustration of the design principle and synthesis process of BC-NWs@ACT/S/rGO hybrid structure. (b,c,d) Digital images of cotton textile, BC-NWs@ACT and BC-NWs@ACT/S/rGO samples. The corresponding samples under folded state are also imaged, as shown in the inset.

Fig. 5.3. Synthesis and characterization of BC-NWs@ACT composite. (a) Low-magnification SEM image of BC-NWs@ACT and TEM image inset of a B₄C nanowire. (b) Nitrogen adsorption/desorption isothermal curves of the BC-NWs@ACT composite.

Fig. 5.4. Synthesis and characterization of BC-NWs@ACT/S composite. (a) Low-magnification SEM image of BC-NWs@ACT/S. (b) TEM image of BC-NW/S (EDS sulfur map and corresponding SEM image of BC-NWs/S in the inset). (d) HRTEM image and close-up observations of B₄C and sulfur, and (e) the corresponding FFT of BC-NW/S.

Fig. 5.5. Characterization of BC-NWs@ACT/S composite. (a) XRD patterns of sulfur powders, BC-NWs@ACT and BC-NWs@ACT/S. (b) EDX characterization of BC-NW and BC-NW/S. (c) Raman spectra of pure S powder, BC-NWs@ACT, BC-NWs@ACT/S, and BC-NWs@ACT/S/rGO. High-resolution (g) B 1s, (h) C 1s, and (i) S 2p XPS spectra of BC-NWs@ACT/S.

Fig. 5.6. Synthesis and characterization of BC-NWs@ACT/S/rGO composite. (a) SEM image of BC-NWs@ACT/S/rGO. (b) HRTEM image and close-up observations of B₄C, sulfur and rGO, and (c) the corresponding FFT of BC-NW/S/rGO. High-resolution (d) B 1s, (e) C 1s, and (f) S 2p XPS spectra of BC-NWs@ACT/S/rGO.

Fig. 5.7. Schematic illustration of a representative volume element of BC-NWs@ACT/S/rGO electrode.

Fig. 5.8. Electrochemical characterization of composite electrodes. (a) Galvanostatic discharge/charge profiles of ACT/S, ACT/S/rGO, and BC-NWs@ACT/S. (b) Galvanostatic discharge/charge profiles of BC-NWs@ACT/S/rGO at the current density of 0.6 mA/cm².

Fig. 5.9. Electrochemical characterization of BC-NWs@ACT/S/rGO composite electrode. (a) Initial cyclic voltammogram profiles at a scan rate of 0.1 mV/s. (b) Rate performance at different current

densities.

Fig. 5.10. Electrochemical characterization of composite electrodes. (a) Cycling performance and correlated coulombic efficiency of BC-NWs@ACT/S/rGO. (b) Cycling performance of ACT/S, ACT/S/rGO, and BC-NWs@ACT/S.

Fig. 5.11. Nyquist plots and the equivalent circuit of the BC-NWs@ACT/S/rGO cathode at the 1st and 500th cycles.

Fig. 5.12. Atomic structures used in MD simulations of (a) Boron carbide, (b) Graphene, (c) 1,3-dioxolane (DIOX), (d) 1,2-dimethoxyethane (DME) and (e) Lithium polysulfides.

Fig. 5.13. MD models of polysulfide particle diffusion with and without B₄C.

Fig. 5.14. SEM images of (a,b) BC-NWs@ACT/S and (c,d) ACT/S electrodes after cycling. (e) Photographs of Li₂S₆ polysulfide absorption test with ACT and BC-NWs@ACT.

Fig. 5.15. MD snapshots of the atomic configurations representing a cross-section of the BC-NWs/S/graphene cylindrical structure in a cycle of charge/discharge process.

Fig. 5.16. Electrochemical performance and mechanical characterization of the flexible BC-NWs@ACT/S/rGO composite electrode. (a) Cyclic performance of the flexible battery cell under normal and bent states. (b) The charge/discharge voltage profiles under normal (1st, 2nd and 3rd cycles) and bent (25th, 26th, and 27th cycles) states. (c) The photograph of soft package Li-S cell lightening up a light-emitting diode (LED) in normal and bent states. (d) Nanoindentation load-displacement curves of BC-NWs before and after cycling.

List of Tables

Table 1.1. Fabrication methods and experimental parameters of boron carbide nanowires

Table 2.1. Lattice constants and corresponding interplanar spacings calculated by DFT

Table 4.1. Mechanical properties of unfunctionalized B₄C micro/nano-filler reinforced epoxy composites

Table 4.2. Mechanical properties of PANI functionalized B₄C micro/nano-filler reinforced epoxy composites

Chapter 1 Introduction

1.1 Background and motivation

With the development of technology, new materials and novel forms (shape, dimension and architecture) of materials are urgently needed to meet continuously increasing demand of energy consumptions, and to address the environmental issues. It is widely acknowledged that natural materials often excel over engineered materials. The exceptional multifunctional performance benefits from their hybrid constituents, nanosized building blocks, and perfect unification of hierarchical structure [1–3]. To mimic natural materials, a great deal of effort has been made to develop nanomaterials, and build things the way nature does, atom by atom and molecule by molecule [4]. With some dimensions confined in the nanoscale range (< 100 nm), nanomaterials usually possess unique properties and excellent performance [5], which can be applied in a diverse range of fields, including energy-storage systems [6-10], environmental applications [11-13], electronics [14-16], healthcare [17-20], and among many others [21]. As shown in Fig. 1.1, nanomaterials can be classified as zero-dimensional, one-dimensional and two-dimensional based on geometry, and nanocomposites can be constructed with various configurations using nanomaterials as fillers [4]. The discovery of carbon nanotubes largely stimulated the researchers' interest in one-dimensional nanomaterials [22]. Among numerous materials, carbide compounds continue to spur significant academic interest due to their chemical and mechanical stabilities [23,24].

Boron carbide, one of the third hardest materials known in nature, [25] is distinguished from other materials by its eminent physical and mechanical properties such as low density (2.5 g/cm^3), high melting point (exceeding $2400 \text{ }^\circ\text{C}$), extreme hardness ($27.4 - 37.7 \text{ GPa}$), high elastic modulus (460 GPa),

chemical inertness, high thermal stability, and a high capture section for neutrons. [25,26] Furthermore, armed with a unique rhombohedral crystal structure, boron carbide at reduced dimensions, especially 1-dimensional, often exhibits novel properties such as large specific surface area and high mechanical strength close to its theoretical value. [27] In addition, boron carbide nanowires are ductile, without cracking when being bent to an included angle of 70°. [28] Such exceptional properties make boron carbide nanowire a promising material for numerous applications such as lightweight armor sustaining extreme conditions, abrasives, electronics, energy-storage systems, and neutron absorbers in nuclear

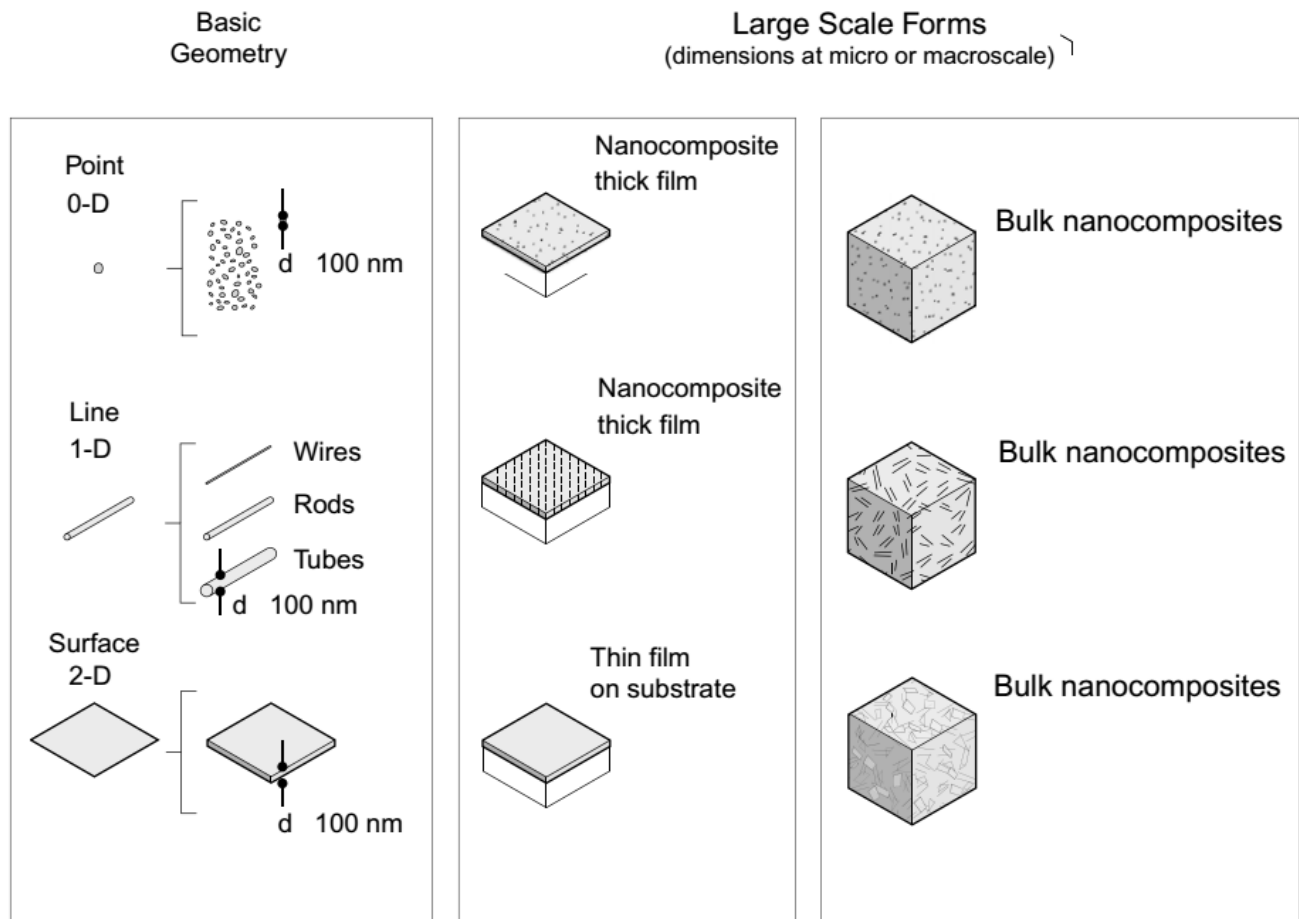


Fig. 1.1. Basic types of nanomaterials. The filler materials, whether 0-D, 1-D, or 2-D nanomaterials are used to make film and bulk nanocomposites. Reprinted from Ashby *et al.* [4]

reactors. [29,30] Numerous techniques have been used to synthesize boron carbide nanowires, such as chemical vapor deposition (CVD), [31] Plasma-enhanced chemical vapor deposition (PECVD), [32] and carbothermal reduction (CTR). [33] However, these techniques normally require complex instruments, high temperature, expensive raw materials, and strict experimental conditions, which will significantly increase the production cost, hindering the large-scale industrial productions. Furthermore, the outstanding mechanical performance makes the multiscale structural design and hierarchical morphology control of boron carbide difficult, largely limiting the application of boron carbide nanowires in the various devices. To solve these problems, understanding the growth mechanisms of boron carbide nanowires is urgently needed, which remain, to a large extent, unknown due to the complex crystal structure and widely varied composition of boron carbide. The primary structural unit cell of boron carbide is a rhombohedral arrangement, consisting of 12-atom icosahedra and 3-atom linear chains, with several distinct crystallographic sites in icosahedral clusters (polar and equatorial) and atomic chains [34-36] The complex atomic configuration and variety in chemical bonding endow boron carbide with exceptional properties; yet these features also make the characterization of boron carbide difficult [37], especially at the atomic level. Furthermore, due to the similarity in electrical and nuclear scattering cross sections between boron and carbon [34,38], there are many boron carbide polytypes with different stoichiometric ratios, making the study of boron carbide nanowire growth mechanisms even more challenging. Therefore, there are many challenges in studying boron carbide nanowires, which need urgently to be tackled to realize the large-scale industrial production of boron carbide nanowires.

In my dissertation, the work mainly focuses on studying the growth mechanisms of boron carbide

nanowires and based on which, synthesis techniques and applications are further explored to expand the scope of application.

1.2 Overview of boron carbide

Boron carbide has a rhombohedral structure consisting of 6 polar sites (icosahedron-icosahedron), 6 equatorial sites (icosahedron-chain) and 3 chain sites (chain-chain) (Fig. 1.2). Within an individual icosahedron, polar and equatorial sites are chemically distinctive. The boron carbide structure can also be described in terms of a hexagonal lattice [34], in which [0001] hexagonal direction corresponds to the [111] rhombohedral direction. The rhombohedral lattice parameters ($R\bar{3}m$ space group) of boron carbide are $a = 5.16\text{\AA}$ and $\alpha = 65.7^\circ$ with minor variations due to the existence of a wide range of stoichiometry

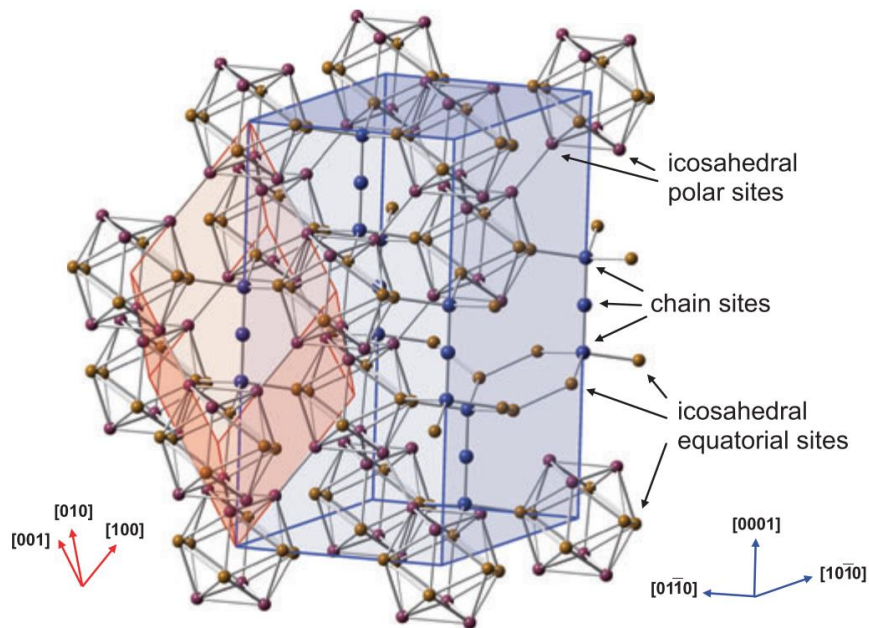


Fig. 1.2. Boron carbide lattice showing correlation between the rhombohedral (red) and the hexagonal (blue) unit cells. Inequivalent lattice sites are marked by arrows. Reprinted from Domnich *et al.* [34]

ratios. Boron carbide could nonetheless be composed of different polytypes with varied stoichiometry [35,38] due to the random occupations of boron and carbon atoms, which are difficult to distinguish because of the fact that ^{11}B and ^{12}C have similar atomic volumes and electronic scattering cross-sections [39,40]. The range of an atomic fraction of carbon extends from ~ 8 at. % to ~ 20 at.% [41,42].

Boron carbide, one of the third hardest materials known in nature (behind diamond and cubic boron nitride), is distinguished from other materials by its eminent physical and mechanical properties such as low density (2.5 g/cm^3), high melting point ($2763 \text{ }^\circ\text{C}$), chemical inertness, high thermal stability, and a high capture section for neutrons. [25,26] Especially, the densely localized covalent bonds make boron carbide exhibit extreme hardness and high stiffness. The mechanical properties of boron carbide, including hardness, Young's modulus, and strength, vary in a wide range, depending on the carbon content. For example, the Young's modulus obtained from experimental data reported so far spans the range from 319 GPa to 472 GPa, and shear modulus lies in the range of 132 GPa – 200 GPa [34,43-46]. Hardness is respectively measured as ~ 30 GPa (Knoop hardness) [41], ~ 47 GPa (Vickers hardness) [47], and ~ 42 GPa (Berkovich hardness) [48,49]. Due to the exceptional properties, boron carbide can be widely used in the fields of sparging, machinery, sealing, drawing, armor, casting, abrasives, nuclear industry, *et. al.* The common methods of boron carbide synthesis can be classified as vapor phase reactions, carbothermic reduction, magnesiothermic reduction, synthesis from elements, synthesis from polymer precursors, liquid-phase reactions, ion beam method, and vapor-liquid-solid growth [50].

1.3 Synthesis and properties of boron carbide nanowires

Boron carbide at reduced dimensions, especially one-dimensional, continues to spur significant academic interest to utilize the outstanding properties of boron carbide in nanocomposites. A variety of methods has been applied to synthesize boron carbide nanomaterials, including carbothermal reductions (CTR) [31,33,51-57], CNT template-mediated growth [58-61], plasma-enhanced CVD (PECVD) [32,62-64], chemical vapor deposition (CVD) [27,65-70], electrostatic spinning [71], a porous alumina template-mediate technique [72], and the annealing process [73]. The vapor-liquid-solid (VLS), vapor-solid (VS),

Table 1.1. Fabrication methods and experimental parameters of boron carbide nanowires

| Fabrication methods | Carbon source | Boron source | Catalyst | Growth temperature (°C) | Ref. |
|---|--|----------------------------------|--|-------------------------|------------|
| CTR | Carbon black | B, B ₂ O ₃ | Fe ₃ O ₄ nanoparticles | 1100 | [31,51-54] |
| | | B, B ₂ O ₃ | N/A | 1650 | [33,55] |
| | | B ₂ O ₃ | Co, Ni, Fe | 1200-1800 | [56] |
| | | B ₂ O ₄ | Co, Ni, Fe | 1200-1800 | [57] |
| CNT template-mediated growth | CNT | B | Ni(NO ₃) ₂ ·6H ₂ O | 1200 | [58] |
| | | B | N/A | 1150 | [59] |
| | | B ₂ O ₃ | N/A | 1100 | [60] |
| | | B ₂ O ₂ | N/A | 1400 | [61] |
| PECVD | C ₂ B ₁₀ H ₁₂ | | Fe | 1100-1200 | [32,62-64] |
| VLS | Cotton | B | Ni(NO ₃) ₂ ·6H ₂ O | 1150-1160 | [27,65] |
| | Organic binder | B | Fe ₃ O ₄ , BaO | 1100 | [66,67] |
| VS | CH ₄ | B ₂ H ₆ | Ni, Fe | 950-1050 | [68,69] |
| SLS | Activated carbon | B | Ni _x Co _y B _z | 1150 | [70] |
| Electrostatic spinning | Poly (norbornenyldeca-borane) | | N/A | 1300-1650 | [71] |
| Porous alumina template-mediate technique | 6,6'-(CH ₂) ₆ (B ₁₀ H ₁₃) ₂ | | N/A | 1025 | [72] |
| Annealing | B ₄ C powder | | Fe(NO ₃) ₃ , Si | 1300 | [73] |

and solid-liquid-solid (SLS) mechanisms have been widely used to explain how one-dimensional nanostructures grow using CVD methods. Table 1.1 summarizes the various fabrication methods and different experimental parameters of boron carbide nanowires.

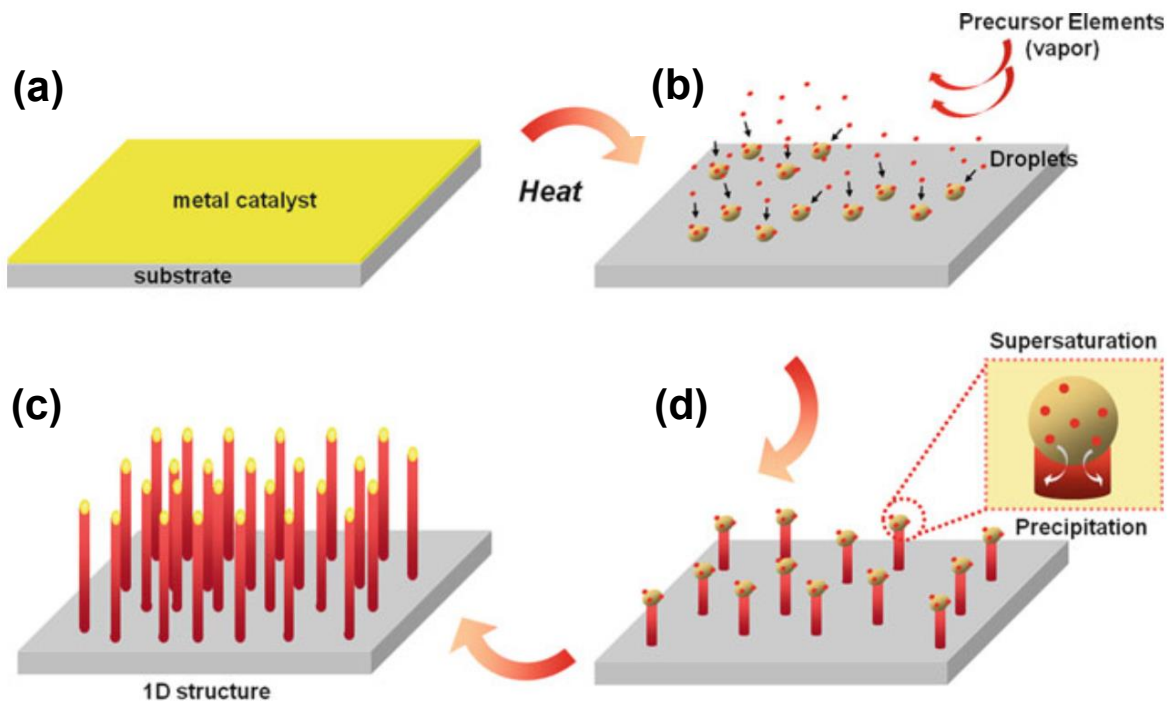


Fig. 1.3. Growth of 1D nano-structures by VLS mechanism. Reprinted from Wagner *et al.* [75]

In various fabrication methods, catalyst-assisted VLS has gradually generated intense scientific interest for one-dimensional nanostructure synthesis, due to its simplicity and versatility, since it was proposed by Wagner in 1964 [74,75]. As shown in Fig. 1.3, three phases coexist in the VLS growth process: (1) vapor phase (precursor); (2) liquid phase (catalyst); (3) solid phase (precipitated nanowires). VLS method can greatly lower the reaction energy, correspondingly decreasing the reaction temperature.

Boron carbide nanowires, with the unique crystal structure and high surface area, possess

extraordinary field emission, thermoelectric, catalytic, and mechanical properties. Tian *et al.* [51] measured the field emission current of an individual boron carbide nanowire by using the focused ion beam system, and an enhancement factor of 10^6 was observed, suggesting that boron carbide nanowires are suitable for electron emission nanodevices. Kirihara *et al.* [65] have reported the electrical transport and thermoelectric properties of boron carbide nanowires, which achieved a maximum Seebeck coefficient of $+350 \mu\text{V K}^{-1}$ and power factor of $264 \mu\text{W m}^{-1}\text{K}^{-2}$ at $T \sim 435 \text{ K}$, higher than bulk boron carbide. Guan *et al.* [69] reported that the thermal conductivity of individual boron carbide nanowires was diameter-dependent with lower thermal conductivity for smaller diameter wires, suggesting that nanowires significantly enhanced thermoelectric properties compared to corresponding bulk boron carbide. Luo *et al.* [58] used a boron carbide nanowire/CNT composite as the cathode material for lithium-oxygen (Li-O) batteries. Due to the efficient catalytic activity and abundant catalytic sites, boron carbide nanowires worked as the efficient bifunctional catalyst for oxygen reduction and evolution reactions in Li-O batteries, with high energy density, favorable rechargeability, and high round-trip efficiency (76%). Tao *et al.* [27] measured the elastic modulus of boron carbide nanowires to be $428.1 \pm 9.3 \text{ GPa}$ using AFM bending tests. Boron carbide is brittle in nature, but at the nanoscale, exhibits a ductile feature. Tao *et al.* [27] observed that boron carbide nanowire had a reversible bending deformation upon unloading with a maximum strain of 45% (a sharp included angle of 53°), and no crack was generated. Such ductility of boron carbide was also observed by Ref. [28] (bent to an angle of 70°) and Ref. [31] (bent to an angle of 160°).

1.4 Overview of the dissertation

In this dissertation, the primary objectives are as follows: (1) study the mass transportation process during the nanowire growth with the goal to thoroughly explain the growth mechanisms of boron carbide nanowires via coupled experimental characterization and theoretical analysis; (2) develop and simplify the synthesis techniques of boron carbide nanowires; (3) explore the low-cost raw materials for boron carbide nanowire production, such as biomass; (4) tailor the surface of boron carbide nanowires for various applications; (5) design and fabricate devices with boron carbide nanowires for the applications of structural materials and energy storage systems.

In Chapter 2, a polytype transformation assisted growth mechanism was proposed in boron carbide nanowires. The growth mechanism of boron carbide nanowires remains, to a large extent, unknown due to the complex crystal structure and widely varied composition. To thoroughly study the growth mechanism in boron carbide nanowires, boron transport during growth process was described using a polytype transformation assisted volume-diffusion model, which was consistent with the experimental characterization. Based on the mechanisms of nanowire growth, more biomass materials were explored to reduce the nanowire production cost with the goal to achieve large-scale production.

In Chapter 3, a graphene interface engineering technique was reported which glued B₄C nanowires with epoxy, enabling exceptionally enhancements in both strength and toughness. In specific, high-density B₄C nanowires were obtained via a vapor-liquid-solid (VLS) process. High-quality graphene sheets were converted directly from graphite and simultaneously wrapped onto the B₄C nanowires by shear-mixing. The as-obtained graphene wrapped B₄C-nanowires (graphene@B₄C-NWs) exhibited

excellent dispersion in water. Graphene@B₄C-NWs were dispersed into epoxy resin to fabricate nanocomposites in order to investigate the effect of nano-filler surface treatment on the mechanical performance of the nanocomposites. Such graphene edited B₄C nano-fillers largely improved the dispersion performance, and enhanced the load transfer efficiency of the reinforcements, leading to the overall improved mechanical performance of the composites.

In Chapter 4, lightweight yet strong and tough multiscale hybrid boron carbide fillers were used to reinforce epoxy. Multiscale boron carbide fillers were designed and synthesized. Epoxy composites reinforced by multiscale boron carbide fillers were fabricated and characterized by tensile testing, scanning electron microscopy (SEM) and digital image correlation (DIC). Furthermore, an analytical model was built to describe the multiscale reinforced performance of boron carbide.

In Chapter 5, boron carbide nanoskeleton enabled, flexible lithium-sulfur batteries were fabricated and characterized, extending the application of boron carbide nanowires to the field of energy storage. In this chapter, we successfully fabricated a flexible, free-standing cathode with hierarchical structures for Li-S batteries with the flexible activated cotton textile (ACT) cloth as the substrate, boron carbide nanowires as the skeleton, reduced graphene oxide (rGO) as the protective skin. The BC-NW@ACT/S/rGO cathode demonstrated the combined advantages of ACT, boron carbide nanowires and rGO, yielding a significant improvement of electrochemical performance for batteries.

Reference

- [1] Liu, Y., He, K., Chen, G., Leow, W. R. & Chen, X. Nature-inspired structural materials for flexible electronic devices. *Chem. Rev.* **117**, 12893–12941 (2017).
- [2] Nieh, M.-P. et al. Biomimetic nanocoatings with exceptional mechanical, barrier, and flame-retardant properties from large-scale one-step coassembly. *Sci. Adv.* **3**, e1701212 (2017).
- [3] Ming, P. et al. Bioinspired highly electrically conductive graphene–epoxy layered composites. *RSC Adv.* **5**, 22283–22288 (2015).
- [4] Ashby, M. F., Ferreira, P. J. & Schodek, D. L. *Nanomaterials, nanotechnologies and design.* **47**, (Elsevier, 2009).
- [5] Roduner, E. Size matters: Why nanomaterials are different. *Chem. Soc. Rev.* **35**, 583-592 (2006).
- [6] Song, N. N., Gao, Z., Zhang, Y. Y. & Li, X. D. B₄C nanoskeleton enabled, flexible lithium-sulfur batteries. *Nano Energy* **58**, 30–39 (2019).
- [7] Gao, Z. et al. Carbon nanotubes derived from yeast-fermented wheat flour and their energy storage application. *ACS Sustain. Chem. Eng.* **6**, 11386–11396 (2018).
- [8] Gao, Z., Schwab, Y., Zhang, Y., Song, N. N. & Li, X. D. Ferromagnetic nanoparticle–assisted polysulfide trapping for enhanced lithium–sulfur batteries. *Adv. Funct. Mater.* **28**, 1–9 (2018).
- [9] Gao, Z. et al. Cotton-textile-enabled flexible self-sustaining power packs via roll-to-roll fabrication. *Nat. Commun.* **7**, 11586 (2016).
- [10] Zhang, Q., Uchaker, E., Candelaria, S. L. & Cao, G. Nanomaterials for energy conversion and storage. *Chem. Soc. Rev.* **42**, 3127 (2013).
- [11] Lahann, J. Nanomaterials clean up. *Nat. Nanotechnol.* **3**, 320–321 (2008).
- [12] Perreault, F., Fonseca De Faria, A. & Elimelech, M. Environmental applications of graphene-based nanomaterials. *Chem. Soc. Rev.* **44**, 5861–5896 (2015).

- [13] Mauter, M. S. & Elimelech, M. Environmental applications of carbon-based nanomaterials. *Environ. Sci. Technol.* **42**, 5843–5859 (2008).
- [14] Teo, B. K. & Sun, X. H. Silicon-based low-dimensional nanomaterials and nanodevices. *Chem. Rev.* **107**, 1454–1532 (2007).
- [15] Kamyshny, A. & Magdassi, S. Conductive nanomaterials for 2D and 3D printed flexible electronics. *Chem. Soc. Rev.* **48**, 1712–1740 (2019).
- [16] Jariwala, D., Sangwan, V. K., Lauhon, L. J., Marks, T. J. & Hersam, M. C. Carbon nanomaterials for electronics, optoelectronics, photovoltaics, and sensing. *Chem. Soc. Rev.* **42**, 2824–2860 (2013).
- [17] Biju, V. Chemical modifications and bioconjugate reactions of nanomaterials for sensing, imaging, drug delivery and therapy. *Chem. Soc. Rev.* **43**, 744–764 (2014).
- [18] Cheng, C., Li, S., Thomas, A., Kotov, N. A. & Haag, R. Functional Graphene Nanomaterials Based Architectures: Biointeractions, Fabrications, and Emerging Biological Applications. *Chem. Rev.* **3**, 1826–1914 (2017).
- [19] Chen, A. & Chatterjee, S. Nanomaterials based electrochemical sensors for biomedical applications. *Chem. Soc. Rev.* **42**, 5425 (2013).
- [20] Hubbell, J. A. & Chilkoti, A. Nanomaterials for Drug Delivery. *Science* **337**, 303–305 (2012).
- [21] Baglioni, P., Carretti, E. & Chelazzi, D. Nanomaterials in art conservation. *Nat. Nanotechnol.* **10**, 287–290 (2015).
- [22] Baughman, R. H., Zakhidov, A. A. & De Heer, W. A. Carbon nanotubes - The route toward applications. *Science (80-.)*. **297**, 787–792 (2002).
- [23] Xin, L. *et al.* Strengthening behavior in SiC nanowires reinforced pure Al composite. *J. Alloys Compd.* **695**, 2406–2412 (2017).
- [24] Xu, Z. *et al.* In situ Al₄C₃ nanorods and carbon nanotubes hybrid-reinforced aluminum matrix composites prepared by a novel two-step ball milling. *J. Mater. Res.* **34**, 1248–1257 (2019).

- [25] Lazzari, R., Vast, N., Besson, J. M., Baroni, S. & Dal Corso, A. Atomic structure and vibrational properties of icosahedral B₄C boron carbide. *Phys. Rev. Lett.* **83**, 3230–3233 (1999).
- [26] Gu, Y., Chen, L., Qian, Y., Zhang, W. & Ma, J. Synthesis of nanocrystalline boron carbide via a solvothermal reduction of CCl₄ in the presence of amorphous boron powder. *J. Am. Ceram. Soc.* **88**, 225–227 (2005).
- [27] Tao, X. *et al.* B₄C-nanowires/carbon-microfiber hybrid structures and composites from cotton T-shirts. *Adv. Mater.* **22**, 2055–2059 (2010).
- [28] Tao, X. *et al.* Internal electron tunneling enabled ultrasensitive position/force peapod sensors. *Nano Lett.* **15**, 7281–7287 (2015).
- [29] Reddy, K. M., Liu, P., Hirata, A., Fujita, T. & Chen, M. W. Atomic structure of amorphous shear bands in boron carbide. *Nat Commun* **4**, (2013).
- [30] Mauri, F., Vast, N. & Pickard, C. J. Atomic structure of icosahedral boron carbide from a first principles analysis of NMR spectra. *Phys. Rev. Lett.* **87**, 85506 (2001).
- [31] Huang, Y. *et al.* Fabrication of patterned boron carbide nanowires and their electrical, field emission, and flexibility properties. *Nano Res.* **5**, 896–902 (2012).
- [32] McIlroy, D. N. *et al.* Electronic and dynamic studies of boron carbide nanowires. *Phys. Rev. B* **60**, 4874–4879 (1999).
- [33] Ma, R. & Bando, Y. High purity single crystalline boron carbide nanowires. *Chem. Phys. Lett.* **364**, 314–317 (2002).
- [34] Domnich, V., Reynaud, S., Haber, R. A. & Chhowalla, M. Boron carbide: structure, properties, and stability under stress. *J. Am. Ceram. Soc.* **94**, 3605–3628 (2011).
- [35] Duncan, T. M. The distribution of carbon in boron carbide: A ¹³C nuclear magnetic resonance study. *J. Am. Chem. Soc.* **106**, 2270–2275 (1984).
- [36] Tallant, D. R., Aselage, T. L., Campbell, A. N. & Emin, D. Boron carbide structure by Raman

spectroscopy. *Phys. Rev. B* **40**, 5649–5656 (1989).

[37] Bouchacourt, M. & Thevenot, F. Analytical investigations in the B-C system. *J. Less Common Met.* **82**, 219–226 (1981).

[38] Fanchini, G., McCauley, J. W. & Chhowalla, M. Behavior of disordered boron carbide under stress. *Phys. Rev. Lett.* **97**, 1–4 (2006).

[39] Jiménez, I. *et al.* Photoemission and x-ray-absorption study of boron carbide and its surface thermal stability. *Phys. Rev. B* **57**, 13167–13174 (1998).

[40] Morosin, B., Kwei, G. H., Lawson, A. C., Aselage, T. L. & Emin, D. Neutron powder diffraction refinement of boron carbides nature of intericosahedral chains. *J. Alloys Compd.* **226**, 121–125 (1995).

[41] Thévenot, F. Boron carbide—A comprehensive review. *J. Eur. Ceram. Soc.* **6**, 205–225 (1990).

[42] Gosset, D. & Colin, M. Boron carbides of various compositions: An improved method for X-rays characterisation. *J. Nucl. Mater.* **183**, 161–173 (1991).

[43] Nelmes, R. J. *et al.* Observation of inverted-molecular compression in boron carbide. *Phys. Rev. Lett.* **74**, 2268–2271 (1995).

[44] Schwetz, K. a. & Grellner, W. The influence of carbon on the microstructure and mechanical properties of sintered boron carbide. *J. Less Common Met.* **82**, 37–47 (1981).

[45] Murthy, S. R. Elastic properties of boron carbide. *J. Mater. Sci. Lett.* **4**, 603–605 (1985).

[46] McClellan, K. J., Chu, F., Roper, J. M. & Shindo, I. Room temperature single crystal elastic constants of boron carbide. *J. Mater. Sci.* **36**, 3403–3407 (2001).

[47] Niihara, K., Nakahira, A. & Hirai, T. The Effect of Stoichiometry on Mechanical Properties of Boron Carbide. *J. Am. Ceram. Soc.* **67**, C-13-C-14 (2006).

[48] Domnich, V., Gogotsi, Y., Trenary, M. & Tanaka, T. Nanoindentation and Raman spectroscopy studies of boron carbide single crystals. *Appl. Phys. Lett.* **81**, 3783–3785 (2002).

- [49] Yan, X. Q., Li, W. J., Goto, T. & Chen, M. W. Raman spectroscopy of pressure-induced amorphous boron carbide. *Appl. Phys. Lett.* **88**, 86–89 (2006).
- [50] Suri, a K., Subramanian, C., Sonber, J. K. & Murthy, T. S. R. C. Synthesis and consolidation of boron carbide: A review. *Int. Mater. Rev.* **55**, (2010).
- [51] Tian, J. F. *et al.* Probing field emission from boron carbide nanowires. *Chinese Phys. Lett.* **25**, 3463–3466 (2008).
- [52] Tian, J. *et al.* Boron carbide and silicon oxide hetero-nanonecklaces via temperature modulation. *Cryst. Growth Des.* **8**, 3160–3164 (2008).
- [53] Luo, X. *et al.* Synthesis and photoluminescence property of silicon carbide nanowires via carbothermic reduction of silica. *Nanoscale Res. Lett.* **17**, 4585–4591 (2010).
- [54] Bao, L. H. *et al.* Single crystalline boron carbide nanobelts: Synthesis and characterization. *Chinese Phys. B* **17**, 4247–4252 (2008).
- [55] Ma, R. & Bando, Y. Investigation on the growth of boron carbide nanowires. *Chem. Mater.* **14**, 4403–4407 (2002).
- [56] Carlsson, M., García-García, F. J. & Johnsson, M. Synthesis and characterisation of boron carbide whiskers and thin elongated platelets. *J. Cryst. Growth* **236**, 466–476 (2002).
- [57] Johnsson, M. Synthesis of boride, carbide, and carbonitride whiskers. *Solid State Ion.* **172**, 365–368 (2004).
- [58] Luo, W. Bin, Chou, S. L., Wang, J. Z. & Liu, H. K. A B₄C nanowire and carbon nanotube composite as a novel bifunctional electrocatalyst for high energy lithium oxygen batteries. *J. Mater. Chem. A* **3**, 18395–18399 (2015).
- [59] Wei, J. *et al.* Straight boron carbide nanorods prepared from carbon nanotubes. *J. Mater. Chem.* **12**, 3121–3124 (2002).
- [60] Han, W., Bando, Y., Kurashima, K. & Sato, T. Boron-doped carbon nanotubes prepared through a

substitution reaction. *Chem. Phys. Lett.* **299**, 368–373 (1999).

[61] Dai, H., Wong, E. W., Lu, Y. Z., Fan, S. & Lieber, C. M. Synthesis and characterization of carbide nanorods. *Nature* **375**, 769–772 (1995).

[62] Zhang, D., Kempton, B. G., McIlroy, D. N., Geng, Y. & Norton, M. G. Synthesis of boron carbide nanowires and nanocrystal arrays by plasma enhanced chemical vapor deposition. *MRS Proc.* **536**, (1998).

[63] Zhang, D., Mcilroy, D. N., Geng, Y. & Norton, M. G. Growth and characterization of boron carbide nanowires. *J. Mater. Sci. Lett.* **18**, 349–351 (1999).

[64] McIlroy, D. N., Zhang, D., Kranov, Y. & Norton, M. G. Nanosprings. *Appl. Phys. Lett.* **79**, 1540–1542 (2001).

[65] Kirihara, K., Mukaida, M. & Shimizu, Y. Electrical transport and thermoelectric properties of boron carbide nanowires. *Nanotechnology* **28**, (2017).

[66] Fu, X., Jiang, J., Liu, C. & Yuan, J. Fivefold twinned boron carbide nanowires. *Nanotechnology* **20**, 365707 (2009).

[67] Fu, X. *et al.* Re-entrant-groove-assisted VLS growth of boron carbide five-fold twinned nanowires. *Chinese Phys. Lett.* **26**, 086110 (2009).

[68] Guan, Z. *et al.* Observation of ‘hidden’ planar defects in boron carbide nanowires and identification of their orientations. *Nanoscale Res. Lett.* **9**, 1–9 (2014).

[69] Guan, Z. *et al.* Boron carbide nanowires: low temperature synthesis and structural and thermal conductivity characterization. *J. Mater. Chem.* **22**, 9853–9860 (2012).

[70] Han, W. Q. Silicon doped boron carbide nanorod growth via a solid-liquid-solid process. *Appl. Phys. Lett.* **88**, 133118 (2006).

[71] Welna, D. T., Bender, J. D., Wei, X., Sneddon, L. G. & Allcock, H. R. Preparation of boron-carbide/carbon nanofibers from a poly(norbornenyldecaborane) single-source precursor via electrostatic spinning. *Adv. Mater.* **17**, 859–862 (2005).

- [72] Pender, M. J. & Sneddon, L. G. An efficient template synthesis of aligned boron carbide nanofibers using a single-source molecular precursor. *Chem. Mater.* **12**, 280–283 (2000).
- [73] Zhang, H. Z. *et al.* Boron carbide nanowires with uniform CN_x coatings. *New J. Phys.* **9**, 13 (2007).
- [74] Choi, Heon-Jin. "Vapor–liquid–solid growth of semiconductor nanowires." *Semiconductor Nanostructures for Optoelectronic Devices*. Springer, Berlin, Heidelberg, 2012. 1-36.
- [75] Wagner, R. S. & Ellis, W. C. Vapor-liquid-solid mechanism of single crystal growth. *Appl. Phys. Lett.* **4**, 89–90 (1964).

Chapter 2 Polytype transformation assisted growth mechanism in boron carbide nanowires

2.1 Introduction

Boron carbide nanowires continue to spur significant academic interest due to their versatility in a diverse range of applications. Particularly, boron carbide nanowires are highly suited for high-strength lightweight material applications in which they are exposed to extreme chemical and thermal conditions, including applications in thermoelectric energy conversion systems, neutron absorbers, and ceramic armors. [1-4] Although numerous techniques have been used to synthesize boron carbide nanowires, such as chemical vapor deposition (CVD) [5], plasma-enhanced chemical vapor deposition (PECVD) [6,7] and carbothermal reduction (CTR) [8], the growth mechanisms of boron carbide nanowires remain, to a large extent, unknown due to the complex crystal structure and widely varied composition of boron carbide. Surface diffusion [9-12] is considered the prominent atomic migration mechanism, enabling traditional vapor-liquid-solid (VLS) growth [13]. However, the boron transportation mechanism in boron carbide nanowire growth has not been unveiled experimentally. Boron possesses unique characteristics requiring further analysis; interestingly, boron was reported to be the only substitutional impurity element found in graphite. [14] In metals, boron was found to diffuse through a special vehicle-free direct-exchange (DE) mechanism. [15] Thus, conventional surface diffusion theory alone cannot explain boron carbide nanowire growth.

The primary structural unit cell of boron carbide is a rhombohedral arrangement, consisting of 12-atom icosahedra and 3-atom linear chains [16-18], with several distinct crystallographic sites in

icosahedral clusters (polar and equatorial) and atomic chains. The complex atomic configuration and variety in chemical bonding endow boron carbide with exceptional properties; yet these features also make the characterization of boron carbide difficult [19], especially at the atomic level. Furthermore, due to the similarity in electrical and nuclear scattering cross sections between boron and carbon [16,20], there are many boron carbide polytypes with different stoichiometric ratios, making the study of boron carbide nanowire growth mechanisms even more challenging.

In this chapter, boron carbide nanowire growth mechanisms were studied by coupled high-resolution transmission electron microscopy (HRTEM) and digital image correlation (DIC) techniques. Importantly, we demonstrate the direct evidence that boron carbide (B_xC_y) polytype transformations facilitate nanowire growth. The first-principles calculation further unveiled that boron atoms migrate in boron carbide nanowires through the polytypic phase transformation. A theoretical model of volume-diffusion-assisted nanowire growth was established to accommodate the observed phase transformation effect; the model was found to be in good agreement with experimental results. Based on the proposed growth mechanisms, various biomass was explored to grow boron carbide nanowires.

2.2 Lattice distortion measurements in boron carbide nanowires

2.2.1 Experimental methods

The synthesis of the boron carbide nanowire/substrate hybrid structure was performed by loading a boron source and the catalyst into the cotton textile via dipping and drying. Amorphous boron powders and cotton were used as boron and carbon sources, respectively. Firstly, a Ni-B emulsion was mixed by dissolving 7g of $Ni(NO_3)_2 \cdot 6H_2O$ and 4g of amorphous boron powders into 10ml of ethanol under

ultrasonic vibration. A piece of cotton textile was cut into a size of 1 cm × 2 cm and then immersed into the Ni-B emulsion. The as-dipped piece was dried at 70°C in a preheated oven for 3h. The boron carbide nanowires were synthesized in a horizontal alumina tube furnace (diameter: 60mm, length: 790mm). The nickel and boron-loaded cotton textile was placed in the middle of the tube furnace and heated to 1160°C with 300 sccm (standard cubic centimeter) continuous flow of argon at atmospheric pressure. The morphology and crystal structure of the as-synthesized and annealed samples were characterized using scanning electron microscopy (SEM; Quanta 650), transmission electron microscopy (TEM; 2000FX), high resolution transmission electron microscopy (HRTEM; FEI Titan 80), X-ray Diffraction (XRD; PANalytical X'Pert Pro MPD) and Raman spectroscopy (Raman; InVia Raman microscope, Renishaw). Lattice distortion was calculated using the digital image correlation technique (DIC).

Comparing “deformed” and “undeformed” images via the DIC method [21,22] allowed for the calculation of distortion in the lattice parameters of boron carbide. The analysis was performed using the Vic-2D software package (Correlated Solutions, South Carolina, USA). Here, the reference image (i.e. “undeformed” image) was obtained from the HRTEM image simulated by the multislice method (JEMS) [23], choosing $a = 5.16\text{\AA}$ and $\alpha = 65.7^\circ$ [24] as ideal rhombohedral lattice parameters, as shown in Fig. 2.1 (a). Both simulated and experimentally captured HRTEM images were operated by the morphological method to extract the atomic arrangements (Fig. 2.1 (c,d)). Depending on the measurement of atomic arrangements, the images with a dotted pattern (Fig. 2.1 (e,f)) were created, which were used as the input data for DIC calculations.

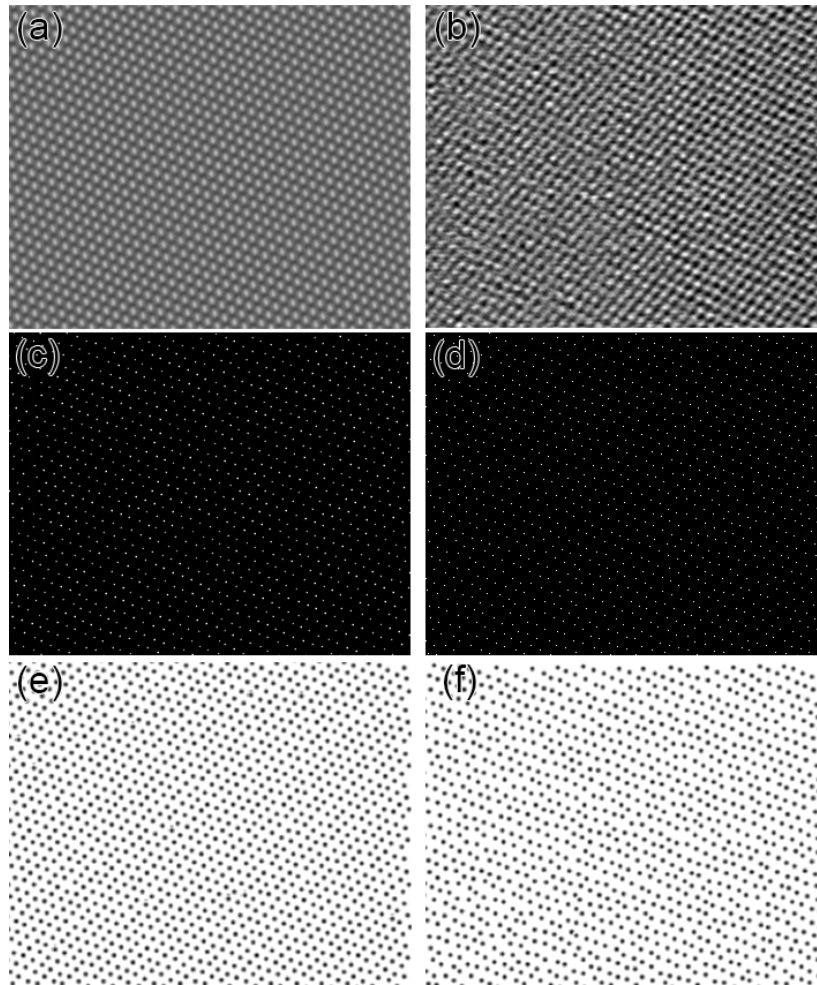


Fig. 2.1. Procedure of exploring input data for DIC calculation. (a) Ideal simulated HRTEM image of boron carbide with [010] as zone axis. (b) HRTEM image of boron carbide nanowires. (c-d) Atomic arrangements were extracted from (a) and (c) by morphological method, respectively. (e-f) Dotted patterns were created according to (c) and (d).

2.2.2 Results and discussion

High-density boron carbide nanowires were synthesized at 1160 °C utilizing amorphous boron powder as the boron source, carbonaceous gases generated from cotton as the carbon source and nickel(II) nitrate as the catalyst [25]. As shown in Fig. 2.2 (a), uniformly aligned boron carbide nanowires with catalytic particles on their tips were grown on cotton microfibers. Inspection by X-ray diffraction (XRD)

(Fig. 2.2 (b)) revealed that the nanowires were of rhombohedral boron carbide (JCPDS No. 6-0555) with nickel boride in the catalyst. Because of the small particle sizes and the addition of nickel in the as-prepared samples, peak broadening and shifting were observed. [26] The electron energy loss spectroscopy (EELS) of individual nanowires unveiled that the C(1s) K-edge fine structure exhibited a weak π^* peak, indicating that the majority of the carbon came from boron carbide nanowires. [27,28]

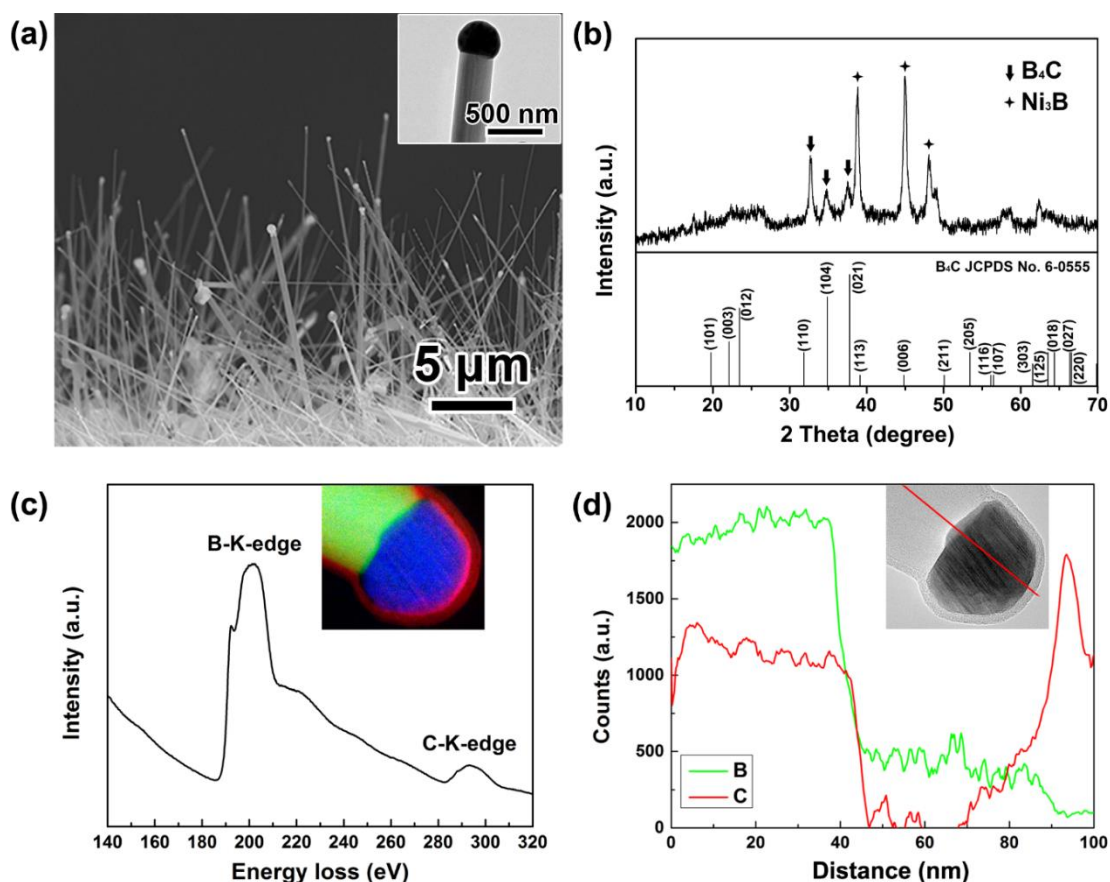


Fig. 2.2. Structural and chemical characterization of boron carbide nanowires. (a) SEM image and TEM image inset, showing the typical morphology of boron carbide nanowires. (b) XRD pattern of boron carbide nanowires, in good agreement with B₄C JCPDS No. 6-0555. (c) EELS pattern, showing that the nanowire is of composition B₁C_{0.29±0.041}, the inset shows the EELS elemental maps of boron (green), carbon (red) and nickel (blue). (d) Variation of composition in the boron carbide nanowire determined by EELS line profile along the length of the wire.

The average C/B atomic ratio of the nanowire was measured to be 0.29 ± 0.041 . The inset in Fig. 2.2 (c) presents the EELS elemental maps of boron (green), carbon (red) and nickel (blue), respectively. The EELS line profile along the nanowire (Fig. 2.2 (d)) revealed that boron atoms migrated into the nickel nanoparticle via the reaction with carbon in the vapor phase, promoting the growth of the nanowire.

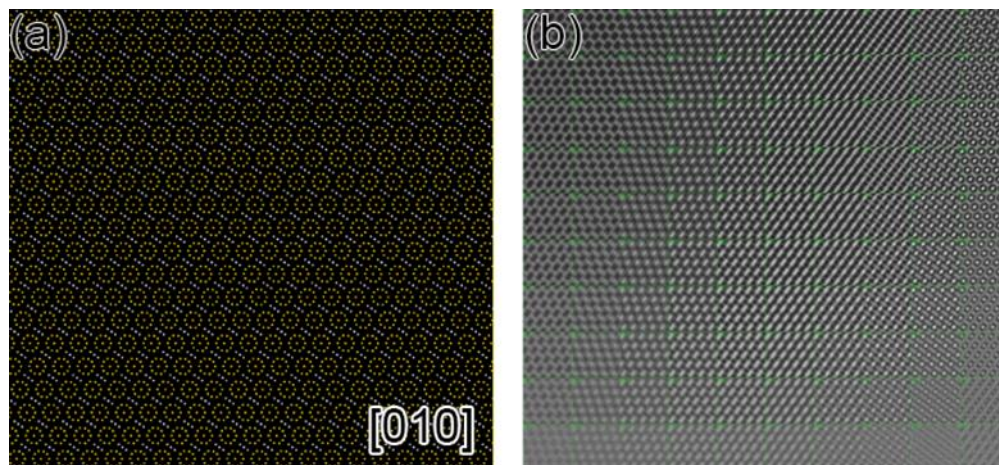


Fig. 2.3. Simulation by the multislice method (JEMS). (a) Atomic arrangement of the boron carbide super-cell, viewed down [010]; (b) A through-focal series of HRTEM contrast images with 10 nm defocus steps.

High-resolution transmission electron microscopy (HRTEM) revealed that the as-synthesized nanowires were single crystals with diameters less than 100nm through most of the wires. Compared with the multislice simulations of HRTEM contrast images (Fig. 2.3), Fig. 2.4 (a) shows a boron carbide nanowire with axial growth plane $(\bar{2}01)$ and the corresponding Fast Fourier Transform (FFT) pattern with a zone axis [010]. As displayed in Fig. 2.4 (b), the measured interplanar spacings of 0.45 nm and 0.43 nm point toward the $(\bar{1}00)$ and (001) planes of rhombohedral boron carbide. Careful examination of the HRTEM image (Fig. 2.4 (b)) unveiled that the measured spacings varied from one location to another, suggesting the presence of heterogeneous lattice strain in the nanowire. To reveal the

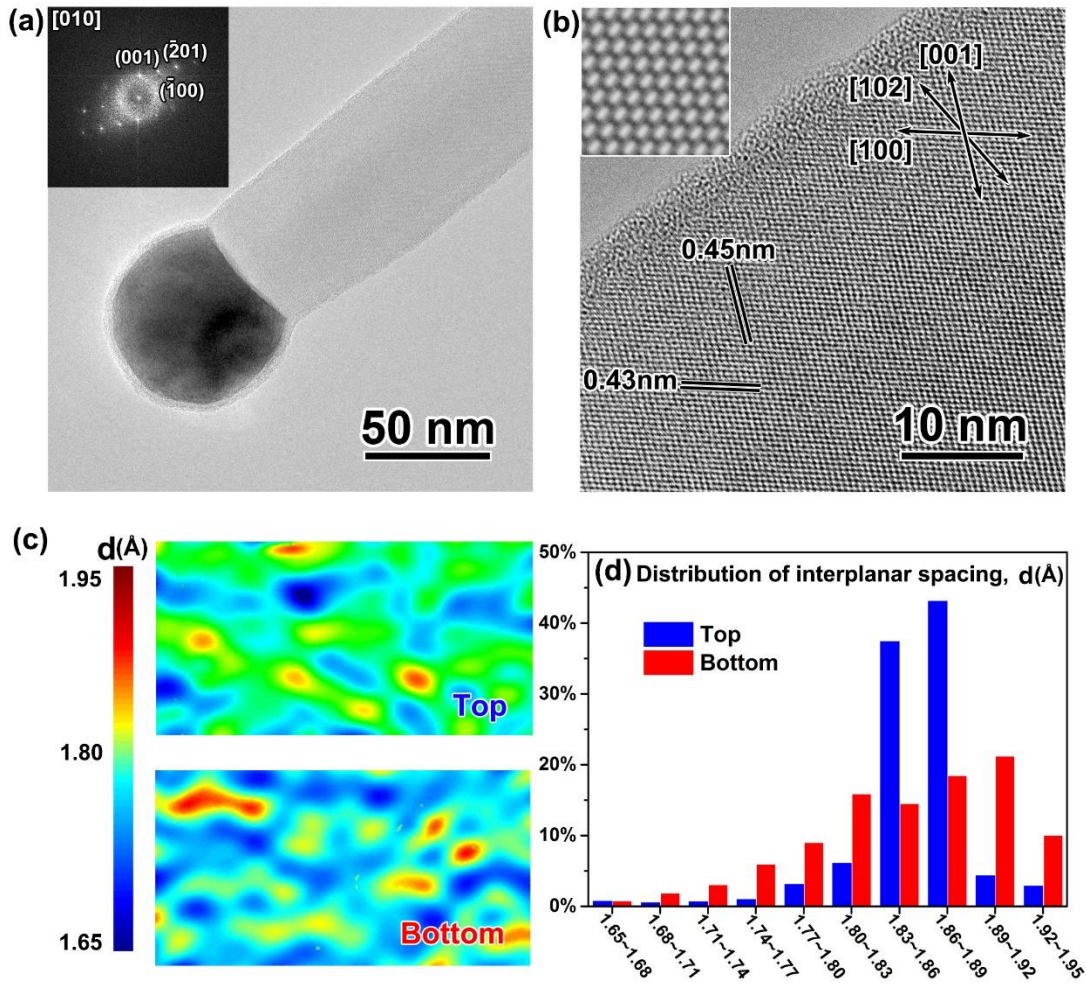


Fig. 2.4. HRTEM inspection and lattice distortion characterization of boron carbide nanowires. (a) HRTEM image and corresponding FFT pattern of a boron carbide nanowire. (b) Close-up observation and the Bloch wave method (JEMS) simulated image of the nanowire. (c) Lattice strain fields obtained by DIC at the top and bottom regions of the nanowire, respectively. (d) Statistics of the interplanar spacing distribution around various regions of the nanowire.

strain field in the nanowire, we processed the HRTEM image with reference to a perfect B₄C crystal lattice ($R\bar{3}m$ space group, $a = 5.16\text{Å}$ and $\alpha = 65.7^\circ$ [24,29]) via digital image correlation (DIC) (supplemental materials). Along the wire growth direction, the atomic strain fields at the top and bottom of the nanowire were calculated respectively, as shown in Fig. 2.4 (c). As obtained from the

corresponding strain fields, the distribution of interplanar spacings was displayed in Fig. 2.4 (d), revealing oscillatory lattice distortions lied in the range of 1.65-1.95 Å with a mean value of approximately 1.85 Å. However, the distribution of the interplanar spacing near the wire top (blue) was obviously more concentrated with a standard deviation (SD) of 0.0367, whereas the bottom area (red) exhibited a more scattered distribution with a SD of 0.0611, suggesting that at the bottom of the nanowire lattice distortions were more pronounced. Based on the strain mapping produced via DIC results, similar distortions of the (203) interplanar spacing were observed along the radial direction of the nanowire, as shown in Fig. 2.5, which was induced by different atomic arrangements.

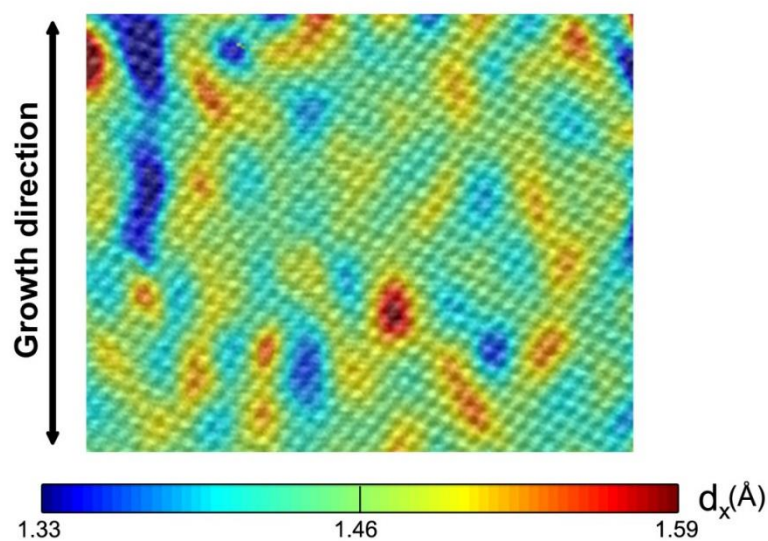


Fig. 2.5. Interplanar spacing map obtained by DIC along axial direction of nanowire.

2.3 Polytypic boron carbide transformation in nanowires

Why did such large lattice distortions arise during the boron carbide nanowire growth? It is noteworthy that the lattice parameters of boron carbide vary due to the wide compositional range possible

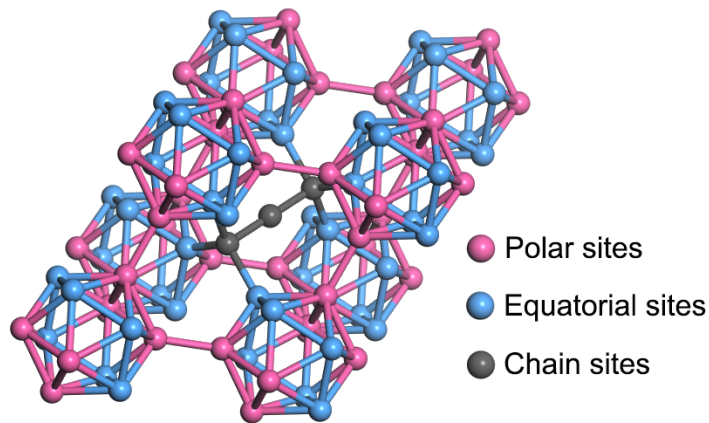


Fig. 2.6. The rhombohedral unit cell of boron carbide lattice contains polar sites (pink), equatorial sites (blue) and chain sites (gray).

in boron carbide [16,28]. The boron carbide crystal structure (Fig. 2.6) consists of 12-atom icosahedra and 3-atom chains, including 6 polar sites (icosahedron-icosahedron), 6 equatorial sites (icosahedron-chain) and 3 chain sites (chain-chain). Although our XRD and HRTEM inspections jointly revealed that the as-synthesized boron carbide nanowires are of a single rhombohedral phase [19], they could nonetheless be composed of different polytypes with varied stoichiometry [17,30] due to the random occupations of boron and carbon atoms, which are difficult to distinguish because of the fact that ^{11}B and ^{12}C have similar atomic volumes and electronic scattering cross-sections [20,29]. To fundamentally understand the atomic arrangements in the synthesized boron carbide nanowires, density functional theory (DFT) calculations were performed to obtain the formation enthalpies of possible polytypic boron carbides at 0K. All calculations in this section were performed using Cambridge Serial Total Energy Package (CASTEP) [31] based on density functional theory (DFT). Gradient-corrected approximation (PW 91 function) was selected to describe the exchange and correlation energy. The Broyden–Fletcher–Goldfarb–Shanno (BFGS) minimizer was used to perform cell optimization, and the convergence

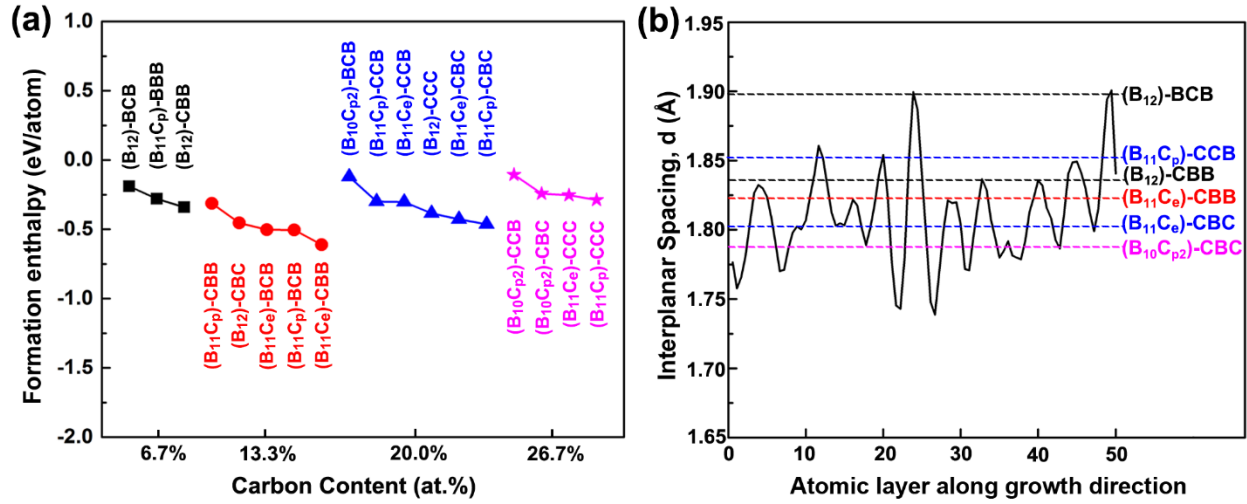


Fig. 2.7. (a) Formation enthalpy of selected boron carbide polytypes at 0K calculated using first principles method. (b) Comparison of measured interplanar spacings with theoretical values.

tolerance of total energy was set to be 5×10^{-7} eV/atom.

Polytypic boron carbides were noted as $(B_xC_{(e/p)y})$ -XXX. Where XXX represents the chain atoms, and e/p represents equatorial or polar sites that the carbon atom occupies. The unit formation enthalpy ($\Delta H_{B_mC_n}$, eV/atom) of boron carbide is defined as [32]:

$$\Delta H_{B_mC_n} = [H(B_mC_n) - mH(\alpha\text{-Boron}) - nH(\text{Graphite})] / (m + n), \quad (2.1)$$

As shown in Fig. 2.7 (a), all boron carbide polytypes have negative formation energies, indicating high stability. However, the formation enthalpies of different boron carbide polytypes are all slightly different (in the range of $-0.6 \sim -0.1$ eV) and are comparable in terms of kinetic energy ($k_B T$, $T=1433$ K). According to the Ostwald rule [33,34], the metastable boron carbide phase, as an intermediate product, forms first and subsequently transforms into a stable phase. Therefore, during boron carbide nanowire growth, all polytypes of boron carbide could form with some of them becoming stable. However, the difference in formation energies between boron carbide polytypes is so small that phase transformations

between polytypic boron carbides could easily occur at high temperature.

To study the influence of stoichiometric ratio on lattice distortion, the lattice parameters of polytypic boron carbides were optimized by DFT and the interplanar spacings of the $(\bar{2}01)$ crystal planes were calculated. The calculated lattice parameters and corresponding interplanar distance along the growth direction of the nanowires are shown in Table 2.1.

Table 2.1. Lattice constants and corresponding interplanar spacings calculated by DFT

| Crystal | Lattice constants | | | | | | Interplanar spacing | |
|--|-------------------|---------|---------|--------------|-------------|--------------|---------------------|-----------------|
| | a (Å) | b (Å) | c (Å) | α (°) | β (°) | γ (°) | $d_{(-201)}$ (Å) | $d_{(203)}$ (Å) |
| B ₁₂ -CBC | 5.19 | 5.19 | 5.19 | 65.87 | 65.88 | 65.88 | 1.83 | 1.47 |
| (B ₁₁ C _c)-BCB | 5.17 | 5.13 | 5.18 | 65.87 | 66.82 | 67.09 | 1.85 | 1.46 |
| (B ₁₁ C _c)-CBB | 5.08 | 5.13 | 5.07 | 66.01 | 67.58 | 66.09 | 1.82 | 1.43 |
| (B ₁₁ C _p)-BCB | 5.27 | 4.97 | 5.15 | 69.59 | 65.67 | 68.09 | 1.84 | 1.52 |
| (B ₁₁ C _p)-CBB | 5.22 | 5.00 | 5.21 | 67.63 | 65.97 | 67.62 | 1.84 | 1.50 |
| (B ₁₀ C _{p2})-BCB | 5.26 | 4.89 | 5.26 | 69.12 | 66.30 | 69.12 | 1.86 | 1.54 |
| (B ₁₁ C _c)-CBC | 5.20 | 5.17 | 5.20 | 65.07 | 65.04 | 65.07 | 1.80 | 1.46 |
| (B ₁₁ C _c)-CCB | 5.21 | 5.21 | 5.13 | 66.84 | 66.84 | 65.63 | 1.84 | 1.46 |
| (B ₁₁ C _p)-CBC | 5.20 | 5.06 | 5.20 | 66.14 | 65.40 | 66.15 | 1.82 | 1.48 |
| (B ₁₁ C _p)-CCB | 5.21 | 5.05 | 5.21 | 67.44 | 66.50 | 67.44 | 1.85 | 1.50 |
| (B ₁₂)-CCC | 5.18 | 5.18 | 5.18 | 66.26 | 66.26 | 66.26 | 1.83 | 1.47 |
| (B ₁₁ C _p)-BBB | 5.13 | 5.00 | 5.13 | 68.20 | 68.79 | 68.19 | 1.87 | 1.46 |
| (B ₁₂)-CBB | 5.14 | 5.14 | 5.14 | 66.90 | 66.91 | 66.91 | 1.84 | 1.46 |
| (B ₁₂)-BCB | 5.27 | 5.27 | 5.08 | 69.24 | 69.53 | 67.18 | 1.90 | 1.46 |
| (B ₁₀ C _{p2})-CBC | 5.21 | 4.87 | 5.20 | 66.88 | 64.22 | 67.22 | 1.79 | 1.50 |
| (B ₁₀ C _{p2})-CCB | 5.23 | 4.91 | 5.23 | 67.54 | 65.49 | 67.55 | 1.83 | 1.51 |
| (B ₁₁ C _c)-CCC | 5.13 | 5.20 | 5.20 | 64.48 | 65.34 | 65.35 | 1.80 | 1.45 |
| (B ₁₁ C _p)-CCC | 5.20 | 5.04 | 5.20 | 66.15 | 65.07 | 66.15 | 1.81 | 1.48 |

Based on the DFT calculations, the lattice parameters were shown to change according to the atomic arrangements. The calculated interplanar spacings are displayed by dashed lines in Fig. 2.7 (b) and are comparable with the experimental values (solid lines, extracted from the DIC strain maps (Fig. 2.4 (c))). Lattice parameters and the corresponding interplanar spacings of other polytypic boron carbides are presented in the supplemental material and are all in a reasonable range compared with the DIC results. Therefore, it can be concluded that the varied distribution of interplanar spacing observed in the synthesized nanowires was induced by the transformation of various polytypic boron carbides. An immediate question is: what role does the transformation of polytypic boron carbides play in the nanowire growth? To further understand the growth mechanisms, atomistic mass transport models were established in the next section.

2.4 Polytypic phase transformation enabled boron carbide nanowire growth

2.4.1 Surface-diffusion induced nanowire growth

In the traditional theoretical study [10,35-36] of nanowire growth, it is assumed that atoms are transported from bottom to top along nanowires by surface diffusion, as shown in Fig. 2.8. In order to calculate the growth rate of the nanowire, we should consider two steady-state surface diffusion equations for boron adatoms on the nanowire sidewall (n_w , per unit area) and the substrate (n_s , per unit area):

$$k_D \frac{d^2 n_w}{dz^2} - \frac{n_w}{\tau} = 0 \quad (2.2)$$

$$k_D \left[\frac{1}{r} \frac{d}{dr} \left(r \frac{dn_s}{dr} \right) \right] + \frac{C_\infty}{\tau} - \frac{n_s}{\tau} = 0 \quad (2.3)$$

Here, for sake of simplicity, it is assumed that boron atoms have the same diffusion distance on the

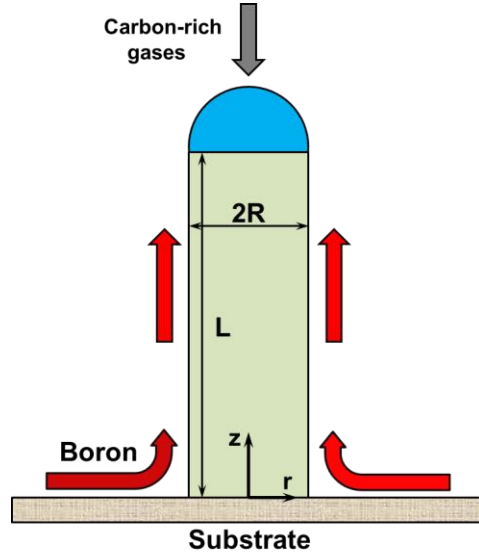


Fig. 2.8. Schematic diagram depicting the model of surface diffusion during nanowire growth.

substrate and along the nanowires ($\lambda_s = 200nm$). The boundary conditions are given by:

$$n_s(r \rightarrow \infty) = C_\infty, \quad n_s(r = R) = n_w(z = 0), \quad k_D \frac{dn_s}{dr} \Big|_{r=R} = -k_D \frac{dn_w}{dz} \Big|_{z=0} \quad \text{and} \quad n_w(z = L) = C_0.$$

Boron adatom diffusion-limited growth rate can be represented as:

$$\frac{\pi R^2}{\Omega} \left(\frac{dL}{dt} \right) = -\xi 2\pi R k_D \frac{dn_w}{dz} \Big|_{z=L} \quad (2.4)$$

The solutions of the diffusion equations are obtained as:

$$n_w(z) = b_1 \sinh(z/\lambda_s) + b_2 \cosh(z/\lambda_s) \quad (2.5)$$

$$n_s = C_\infty + b_3 K_0(r/\lambda_s) \quad (2.6)$$

with coefficients:

$$b_1 = \frac{[C_0 - C_\infty \cosh(L/\lambda_s)] K_1(R/\lambda_s)}{K_1(R/\lambda_s) \sinh(L/\lambda_s) + K_0(R/\lambda_s) \cosh(L/\lambda_s)}$$

$$b_2 = \frac{C_0 K_0(R/\lambda_s) + C_\infty K_1(R/\lambda_s) \sinh(L/\lambda_s)}{K_1(R/\lambda_s) \sinh(L/\lambda_s) + K_0(R/\lambda_s) \cosh(L/\lambda_s)}$$

$$b_3 = \frac{C_0 - C_\infty \cosh(L/\lambda_s)}{K_1(R/\lambda_s) \sinh(L/\lambda_s) + K_0(R/\lambda_s) \cosh(L/\lambda_s)} \quad (2.7)$$

Then the surface diffusion induced nanowire growth rate can be calculated as:

$$\left(\frac{dL}{dt}\right)_D = -\frac{2\Omega\xi k_D}{R\lambda_s} (b_1 \cosh(L/\lambda_s) + b_2 \sinh(L/\lambda_s)) \quad (2.8)$$

2.4.2 Volume-diffusion induced nanowire growth

The critical factor governing nanowire growth is mass transport. It is widely accepted that atoms are transferred from the bottom to top along the nanowire via surface diffusion; however, direct evidence that supports this assumption is still lacking. In our experiments, carbon-rich gases, α -boron and nickel (catalyst) were involved in the boron carbide nanowire synthesis. Because the synthesized boron carbide nanowires were uniform in terms of diameter, it is presumed that the carbon atoms transferred to the solid phase only through absorption on the surface of catalyst droplets while boron atoms diffused from the substrate to the top of the nanowire, forming boron carbide at the interface between the nanowire and the catalyst particle. [37] Here we utilized the Nudged Elastic Band (NEB) [38] method to perform a static calculation of the energetic barrier to atom-swapping in order to illustrate the pathways for boron migration in boron carbide nanowire growth. As shown in Fig. 2.7 (a), energetically favorable polytypes, $(B_{11}C_e)$ -CBC and $(B_{11}C_e)$ -CBB, are selected as basic structures. Two modes of boron migration are proposed: (i) atom diffusion (denoted as D mode), $(B_{11}C_e)$ -CBC + B \rightarrow $(B_{11}C_e)$ -CBC + B and (ii) polytypic phase transformations (denoted as T mode), $(B_{11}C_e)$ -CBC + B \rightarrow $(B_{11}C_e)$ -CBB + C. The various pathways (T₁, T₂) with the minimum energetic barrier for transitions of polytypic phases in the nanowire are efficiently searched, as shown in Fig. 2.9. The energy barriers were calculated to be 3.71

eV, 1.35eV and 1.13eV, for D, T₁ and T₂ pathways, respectively. The small energy difference between initial and transition states support the assumption that polytypic boron carbide transformation is preferential for boron migration in the nanowire growth. In addition, according to the results obtained from T₁ (inside of the nanowire) and T₂ (near the surface of the nanowire), the energy barriers for the T mode exhibited little change with various transformation sites in nanowires, illustrating that boron

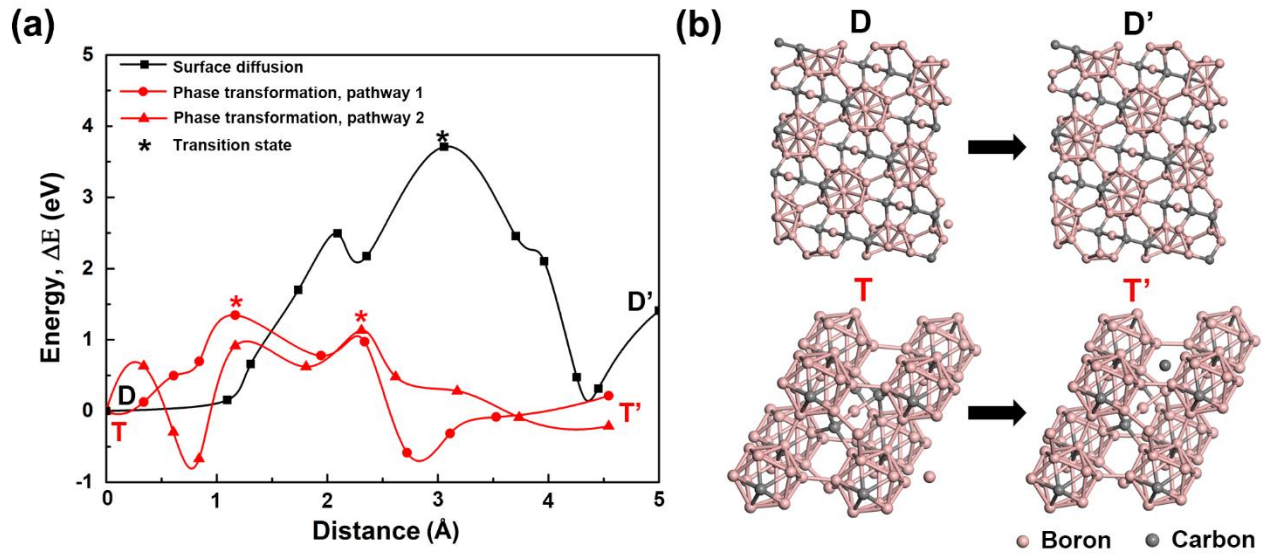


Fig. 2.9. (a) Energy pathways and (b) schematic diagrams of boron migrations through surface diffusion (D mode) and polytypes transformation (T mode).

migration could occur not only on the surface but also in the body of the nanowire.

The migration rate of boron atoms at a high temperature can be described using the Arrhenius relation [39] as:

$$k = k_0 \exp\left(\frac{-E_a}{k_B T}\right), \quad (2.9)$$

where E_a , k_B , and T represent activation energy, Boltzmann constant and growth temperature, respectively.

The pre-exponential factor, k_0 can be calculated [40] according to:

$$k_0 = f v^0 a^2 \exp\left(\frac{\Delta S}{k_B}\right), \quad (2.10)$$

where f is the correlation factor, v^0 is an attempt frequency, a is the lattice parameter, and ΔS is the diffusion entropy. Migration rates were calculated using the following parameters: $T = 1433$ K, $f = 1$, $v^0 = 10^{13}$ /s, $a = 0.52$ nm and $\Delta S = 10 k_B$ [41]. The migration rate of boron in the T mode (k_T) was calculated to be 1.07×10^{-2} cm²/s, at least eight orders of magnitude higher than that of the D mode ($k_D = 5.37 \times 10^{-11}$ cm²/s).

Based on the results obtained above, a universal kinetic growth model was developed to calculate the growth rate of the nanowire. The general assumptions are that (i) separations between the adjacent nanowires are relatively large and amorphous boron powders are supplied without interruption and are distributed uniformly in the entire substrate with atomic concentration C_∞ (per unit volume); (ii) atom migration occurs much faster than nanowire growth, thus the entire system is in steady state, i.e., $(\partial c / \partial t) = 0$; (iii) the substrate (cotton textile) was completely soaked with boron, boron atoms continuously diffuse in the substrate and move through volumetric migration along the nanowire; (iv) the desorption of boron atoms on the surface of the substrate is not obvious; and (v) the carbon source is sufficient, and the growth rate of the boron carbide nanowires is boron-limited, i.e., each boron atom, at top of the nanowire, can immediately find its carbon pair.

As illustrated in Fig. 2.10 (a), the number density of boron along the nanowires c_w (per unit volume), and in the substrate c_s (per unit volume), can be described as follows [42], using the steady-state diffusion equations in cylindrical and spherical coordinates, respectively.

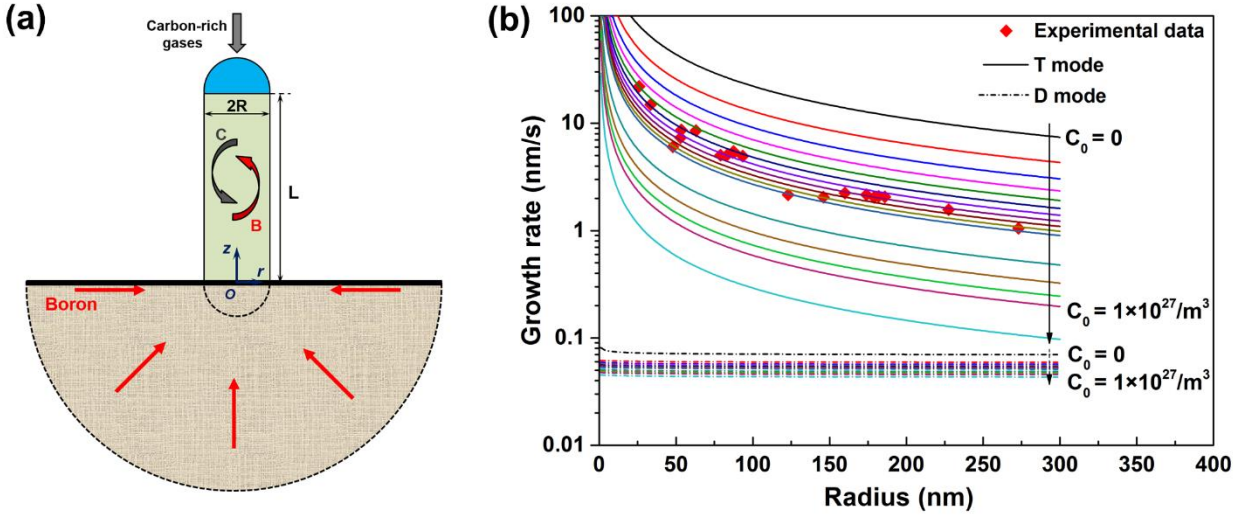


Fig. 2.10. (a) Schematic diagram of VLS based volumetric mass transport in boron carbide nanowire growth. (b) Correlation between the growth rate and radius of nanowires, calculated using the kinetic model with different boron migration modes; the theoretical models are fitted to the experimental data.

$$\frac{\partial c_w(r, z, t)}{\partial t} = k_T \left[\frac{1}{r} \frac{\partial}{\partial r} \left(r \frac{\partial c_w}{\partial r} \right) \right] + k_T \frac{\partial^2 c_w}{\partial z^2} = 0, \quad (2.11)$$

$$\frac{\partial c_s(r, t)}{\partial t} = k_D \left[\frac{1}{r^2} \frac{\partial}{\partial r} \left(r^2 \frac{\partial c_s}{\partial r} \right) \right] = 0 \quad (r \geq R), \quad (2.12)$$

Here, k_T and k_D are the migration rates of boron atoms via phase transformation and diffusion, respectively, and the subscripts “s” and “w” represent the substrate and nanowire, respectively. R is the radius of the nanowire, r and z are the radial and vertical coordinates, as shown in Fig. 2.10 (a). At the top of the nanowire, the average concentration of boron atoms C_0 (per unit volume), can be described using the following equation:

$$\frac{\int_0^R c_w(z=L) 2\pi r dr}{\pi R^2} = C_0, \quad (2.13)$$

where L represents the length of the nanowire. In addition, atom desorption occurs on the sidewall surface of the nanowire, therefore, when $r = R$, c_w also satisfies the following diffusion equation:

$$\left[k_T \nabla^2 c_w - \frac{c_w}{\tau} \right]_{r=R} = 0, \quad (2.14)$$

where τ is the average lifetime of a boron atom before desorption. At the bottom of the nanowire, the net diffusive exchange of boron atoms with the substrate occurs. The coupling conditions of mass conservation and chemical potential continuity lead to the following equations [9,43]:

$$\int_0^R \left[k_T \left(\frac{\partial c_w}{\partial z} \right)_{z=0} \right] 2\pi r dr = -k_D \left(\frac{dc_s}{dr} \right)_{r=R} 2\pi R^2, \quad (2.15)$$

$$\sigma_w c_w (r=R, z=0) = \sigma_s c_s (r=R), \quad (2.16)$$

Where σ_w and σ_s are the areas of elementary sites in the substrate and the nanowire, which are assumed to be the same. Additional boundary conditions are given by $c_s(r \rightarrow \infty) = C_\infty$ and $c_w(r=0) \neq \infty$.

Under these conditions, the solutions to Eq. (2.11) and (2.12) are:

$$c_w(r, z) = J_0(\alpha r) [a_1 \sinh(\alpha z) + a_2 \cosh(\alpha z)], \quad (2.17)$$

$$c_s(r) = C_\infty - a_3/r, \quad (r \geq R) \quad (2.18)$$

with coefficients:

$$\begin{aligned} \alpha &= \frac{1}{\sqrt{k_T \tau}} \\ a_1 &= \frac{\frac{1}{2} C_0 R \alpha J_0(\alpha R) / J_1(\alpha R) - C_\infty \cosh(\alpha L)}{\sinh(\alpha L) J_0(\alpha R) + \frac{k_T}{k_D} \cosh(\alpha L) J_1(\alpha R)} \\ a_2 &= \frac{\frac{1}{2} \frac{k_T}{k_D} C_0 R \alpha + C_\infty \sinh(\alpha L)}{\sinh(\alpha L) J_0(\alpha R) + \frac{k_T}{k_D} \cosh(\alpha L) J_1(\alpha R)} \\ a_3 &= \frac{C_\infty R \cosh(\alpha L) J_1(\alpha R) - \frac{1}{2} C_0 R^2 \alpha J_0(\alpha R)}{\frac{k_D}{k_T} \sinh(\alpha L) J_0(\alpha R) + \cosh(\alpha L) J_1(\alpha R)}, \end{aligned} \quad (2.19)$$

Here, $J_\nu(x)$ are Bessel functions of the first kind.

The nanowire growth rate induced by boron-migration can be defined as

$$\frac{\pi R^2}{\Omega} \left(\frac{dL}{dt} \right) = -\xi \int_0^R \left[k_T \left(\frac{\partial c_w}{\partial z} \right)_{z=L} \right] 2\pi r dr, \quad (2.20)$$

Here, the left-hand side gives the number of atoms per unit time nucleated on top of the nanowire, with Ω as the elementary volume (assuming boron and carbon have the same atomic volume). The right-hand side describes the average mass current (flow of atoms per unit time), with ξ as the modification factor (considering carbon atoms). Substituting the solution (2.17) into Eq. (2.20), the growth rate due to polytypic phase transformation can be expressed as:

$$\left(\frac{dL}{dt} \right)_T = \frac{-2\Omega \xi k_T}{R} J_1(\alpha R) [a_1 \cosh(\alpha L) + a_2 \sinh(\alpha L)], \quad (2.21)$$

Similarly, based on the surface diffusion model, the growth rate of the nanowire due to diffusion can be calculated as the solution (2.8), with coefficients (2.7). Here, $\lambda_s = \sqrt{k_D \tau}$ is the effective diffusion distance.

To verify the accuracy of the models, Eq. (2.21) and (2.8) were used to fit our experimental results, and the parameters were selected based on the experimental conditions. The atomic concentration of boron in the substrate was calculated according to the concentration of the initial Ni-B emulsion (2 g/ml) as $C_\infty = 2.23 \times 10^{28} / m^3$. The elementary volume was estimated to be $\Omega = 7.8 \times 10^{-30} m^3$, according to the bulk density of boron and carbon. In the process of nanowire growth, the migration flux should be always directed to the top because of the macroscopic gradient in chemical potential, which results in a corresponding macroscopic gradient in polytypes, with larger lattice distortions experienced at the bottom of the wire. The average boron concentration C_0 at the top of the nanowire should be in the range

of 0 to C_∞ , which can be expressed considering the continuity of chemical potential [10,43,44]. The fitting results for the nanowire growth are presented in Fig. 2.10 (b), showing that the growth rate gradually decreases with increasing nanowire diameters. The value of C_0 was adjusted to be $C_0 = 6 \times 10^{25} / m^3$ to represent the experimental data accurately. Clearly, the diffusion model in the T mode is in very close agreement with the experimentally observed growth rates of the nanowires, while the D mode model fails to explain the experimental data. Therefore, this volume-diffusion based kinetic model is more suitable for studying boron carbide nanowire growth.

2.5 Biomass-derived boron carbide nanowire growth

2.5.1 Experimental methods

Without further treatment, biomass materials, including cotton, flour, corn silk, paper towel, fallen leaf, were used to provide carbon source to synthesize boron carbide nanowires via VLS method (Fig. 2.11). A Ni-B emulsion was prepared by mixing 7 g of $Ni(NO_3)_2 \cdot 6H_2O$ (catalyst) and 4 g of amorphous boron powders (boron source) into 10ml of ethanol under ultrasonic vibration. Flour powder was mixed with the as-obtained emulsion to obtain the wheat dough. Other biomass materials were cut into small pieces, immersed in the Ni-B emulsion, and dried at 70 °C in a preheated oven for 3 h. The boron carbide nanowires were synthesized in a horizontal alumina tube furnace (diameter: 60 mm, length: 790 mm). The boron-loaded biomass materials were placed in the middle of the tube furnace and heated to 1160 °C for 2 h with 300 sccm (standard cubic centimeter) continuous flow of argon.

The morphology, structure, and composition of the as-synthesized samples were characterized by scanning electron microscopy (SEM, Quanta 650) and x-ray diffraction (XRD, PANalytical X'Pert Pro

Multi-Purpose Diffractometer (MPD) equipped with Cu K α radiation ($\lambda = 0.15406$ nm)).

2.5.2 Results and discussion

Numerous techniques have been used to synthesize B $_4$ C nanowires, such as carbothermal reduction (CTR), CNT template-mediated growth, plasma-enhanced CVD (PECVD), chemical vapor deposition (CVD), electrostatic spinning, porous alumina template-mediate technique, and annealing process, as shown in Table 1.1. However, these techniques often require complex instruments, high temperature, expensive raw materials, and difficult experimental conditions, which significantly increase the production cost, hindering the large-scale production. Based on the polytypic phase transformation enabled mass transport mechanism found in boron carbide nanowire growth, some low-cost raw materials were explored. Carbon is the most abundant element in woody biomass and it is considered to

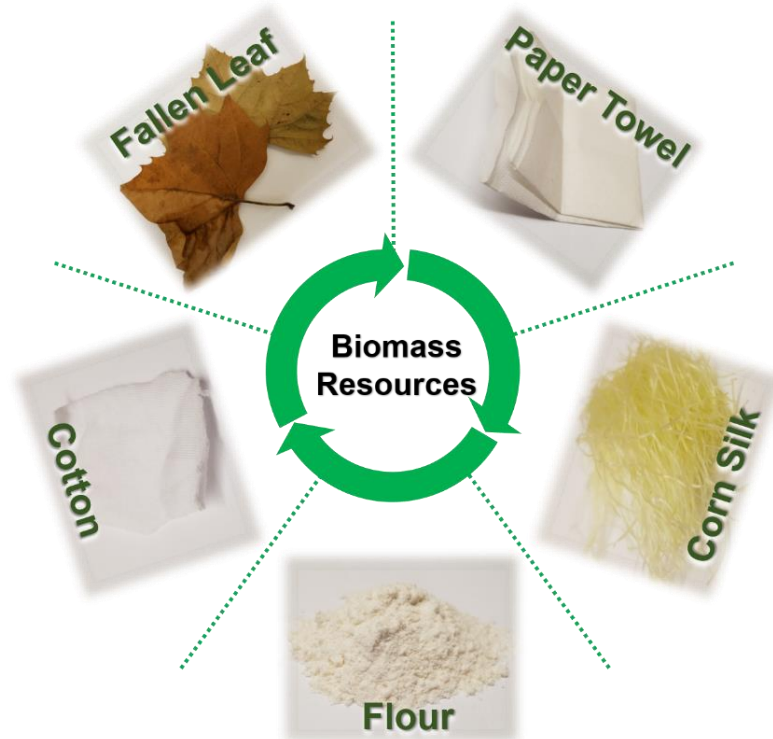


Fig. 2.11. Digital images of biomass resources, including cotton, flour, corn silk, paper towel, and fallen leaf.

be a promising low-cost carbon source for growing boron carbide nanowires.

Here, five biomasses were investigated, including cotton, flour, corn silk, paper towel, and fallen leaf (Fig. 2.11). High-density boron carbide nanowires were successfully synthesized via VLS method, using amorphous boron powder as the boron source, biomass as the carbon source and nickel (II) nitrate as the catalyst. As shown in Fig. 2.12 (a-e), boron carbide nanowires with catalytic particles on their tips were uniformly grown on various biomass, presenting the typical VLS synthesis features. All nanowires have similar dimensions with diameters in the range of 50-500 nm and the average length of 5 μm . XRD inspection (Fig. 2.12 (f)) verified that the nanowires have a highly crystalline structure of rhombohedral boron carbide (JCPDS No. 6-0555) with nickel boride in the catalyst. It has been demonstrated that the

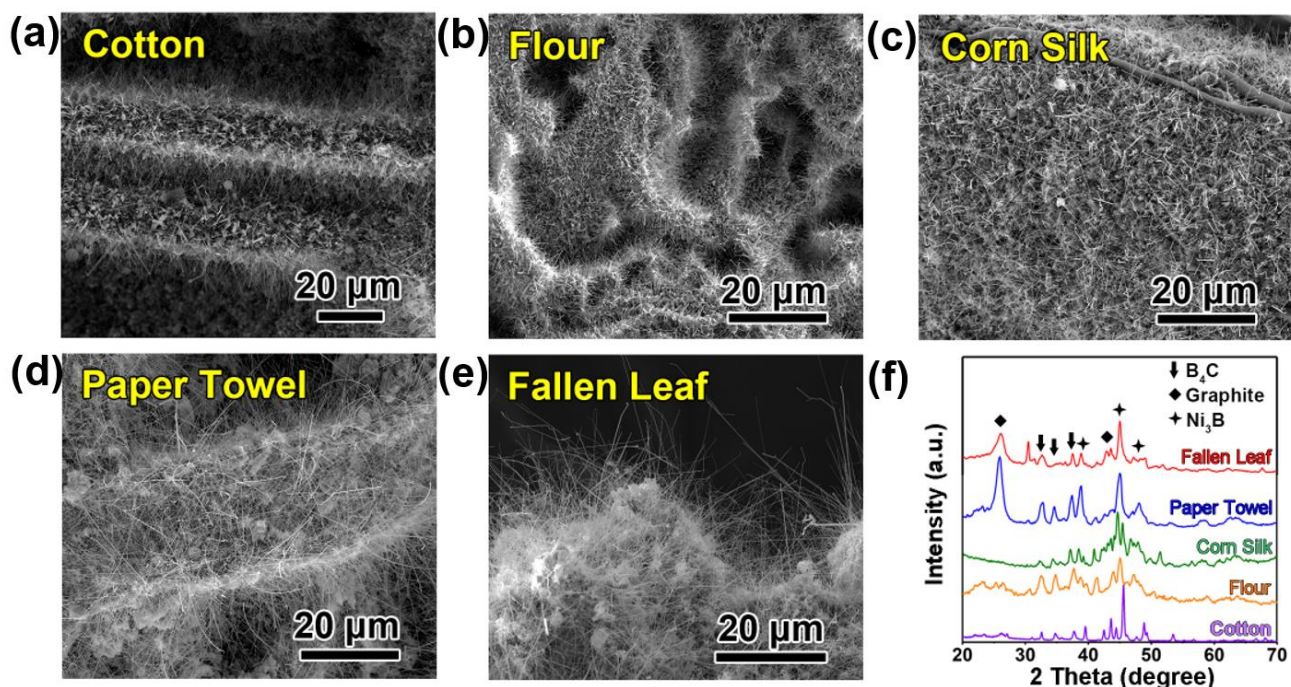
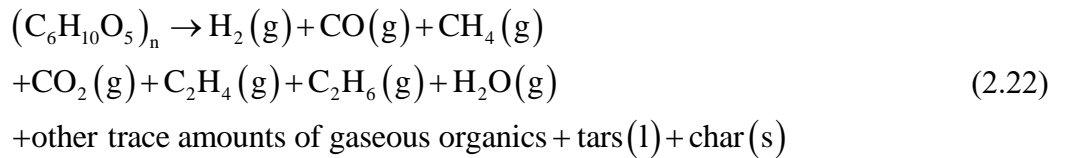


Fig. 2.12. SEM characterization showing the morphology of boron carbide nanowires synthesized from biomass resources: (a) cotton, (b) flour, (c) corn silk, (d) paper towel, and (e) fallen leaf. (f) XRD pattern of boron carbide nanowires, in good agreement with B_4C JCPDS No. 6-0555.

final morphology of boron carbide nanowires is rarely related to the carbon source employed.

Cellulose, the most plentiful organic compound, is the major component of all biomass and behaves the whole decomposition regulations of biomass in pyrolysis. During pyrolysis, the decomposition of cellulose gave rise to carbon-rich gas generation, which served as the carbon source. The gaseous products mainly contained H₂, CO, CO₂, CH₄, C₂H₄, and C₂H₆. Because of the thermal cracking of carbonyl and carboxyl, cellulose exhibits a relatively high CO yield [45], which is vital the in B₄C nanowire growth, as shown below:



Catalysts, promoting nanowire growth, are essential in the VLS growth of boron carbide nanowires. Nickel, serving as the catalyst, was obtained by thermal decomposition of Ni(NO₃)₂·6H₂O. After several degradation steps, nickel oxide (NiO) was generated [46] and then reduced to metallic nickel by hydrogen, carbon, and carbon monoxide (decomposition products of cotton) [47] at high temperature, revealing that biomass also played a key role in producing the catalysts. Fig. 2.13 shows that NiO, the thermal decomposition product of Ni(NO₃)₂·6H₂O, was reduced to nickel and then condensed into small droplets on the surface of the cotton microfibers. The XRD pattern of the prepared textile with nickel nanoparticles, as shown in Fig. 2.13(d), reveals three typical diffraction peaks, which can be indexed to the (111), (200) and (220) reflections of cubic nickel (Fm-3m). Due to the reducibility of biomass, nickel nitrate was used as a catalyst during VLS nanowire growth process, and the reaction temperature was decreased significantly.

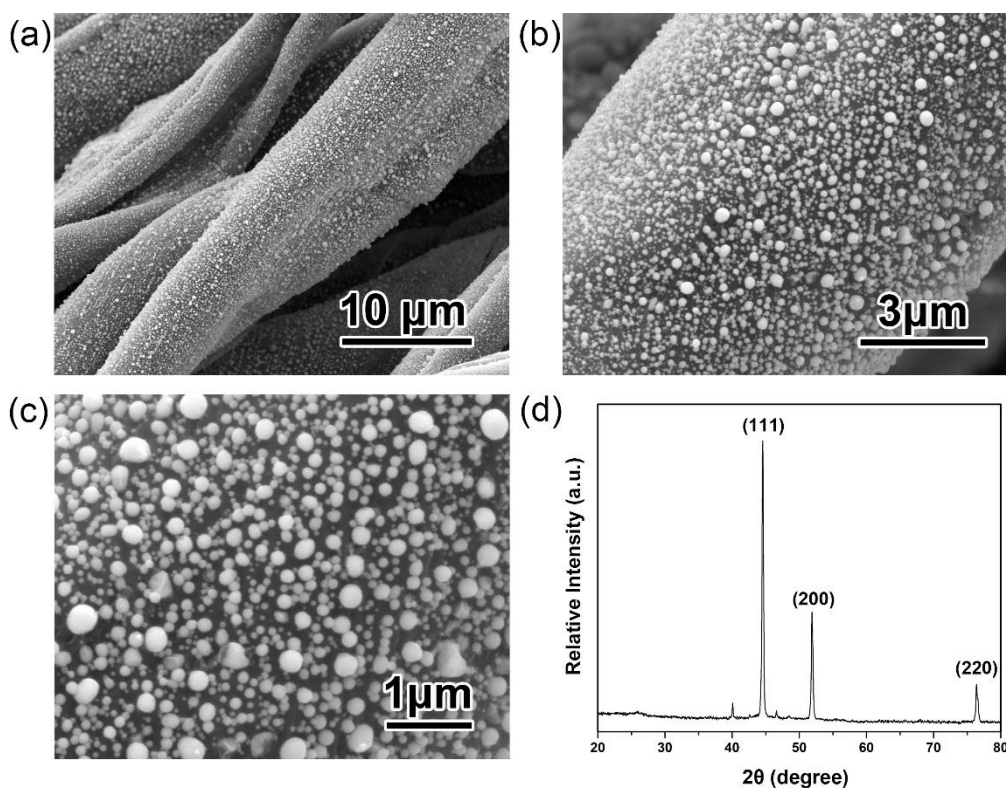
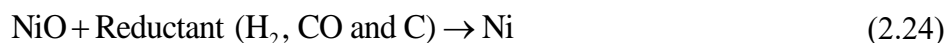


Fig. 2.13. (a-c) SEM images of nickel nanoparticles distributed uniformly on cotton textile. (d) XRD pattern of nickel nanoparticles.

Boron carbide nanowires have been successfully synthesized from Ni/B mixture loaded cotton textiles (B+Ni@cotton). Volume-diffusion induced mass transport model was built to describe how boron atoms migrate from substrate to the top of the nanowire. More experiments were performed to verify that boron atoms moved by diffusion in solid-phase along nanowires, not through gas flow in vapor-phase. B-loaded cotton textile (B@cotton) and Ni-loaded cotton textile (Ni@cotton) were both placed in the tube furnace separately and treated at 1160 °C for 4 h (Fig. 2.14). SEM inspection revealed some

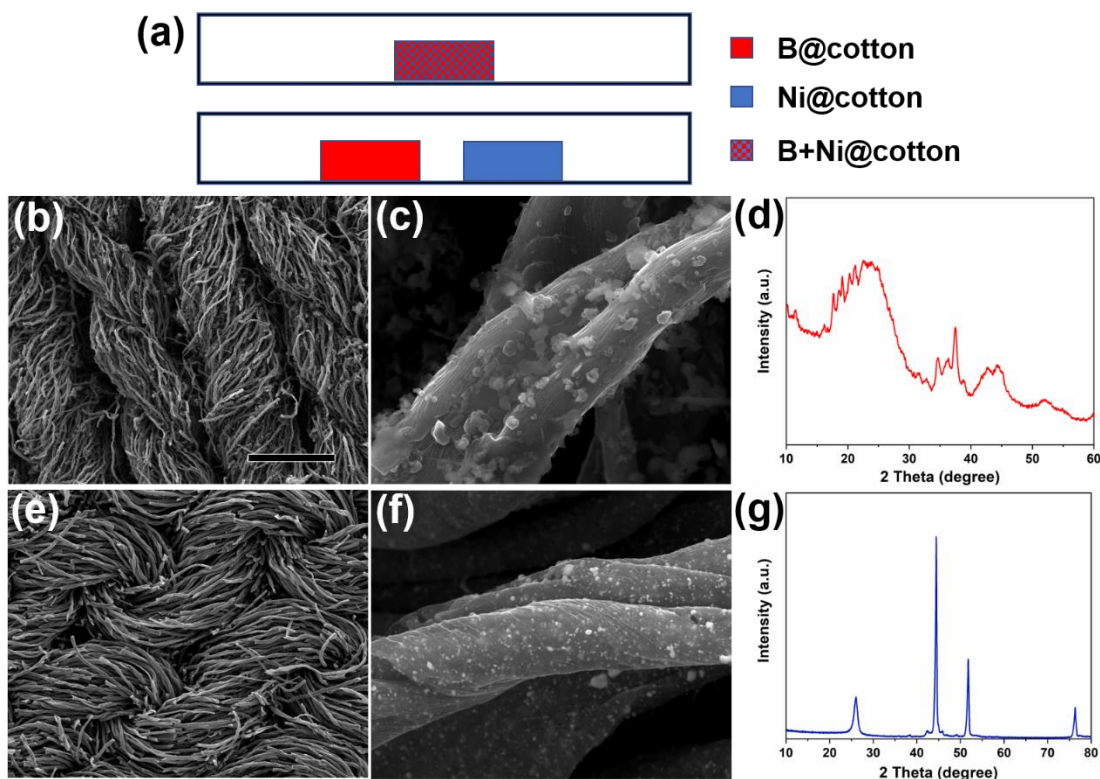


Fig. 2.14. (a) Schematic illustration showing sample arrangements in the tube furnace (red and blue colors represent boron and nickel, respectively). (b) and (c) SEM images of B@cotton. (d) XRD pattern of B@cotton. (e) and (f) SEM images of Ni@cotton. (g) XRD pattern of Ni@cotton.

nanoparticles on both B@cotton (Fig. 2.14 (b) and (c)), and Ni@cotton (Fig. 2.14 (e) and (f)), yet no nanowires were observed. XRD characterization (Fig. 2.14 (d)) showed peaks of amorphous boron (JCPDS No. 12-0377), boron carbide (JCPDS No. 6-0555), and activated carbon from B@cotton. XRD inspection (Fig. 2.14 (d)) revealed peaks of nickel (JCPDS No. 1-1260) and graphite (JCPDS No. 1-0640) from Ni@cotton. Therefore, boron atoms did not migrate from the B@cotton to Ni@cotton via vapor flow. The growth process of biomass-derived boron carbide nanowires is summarized in Fig. 2.15.

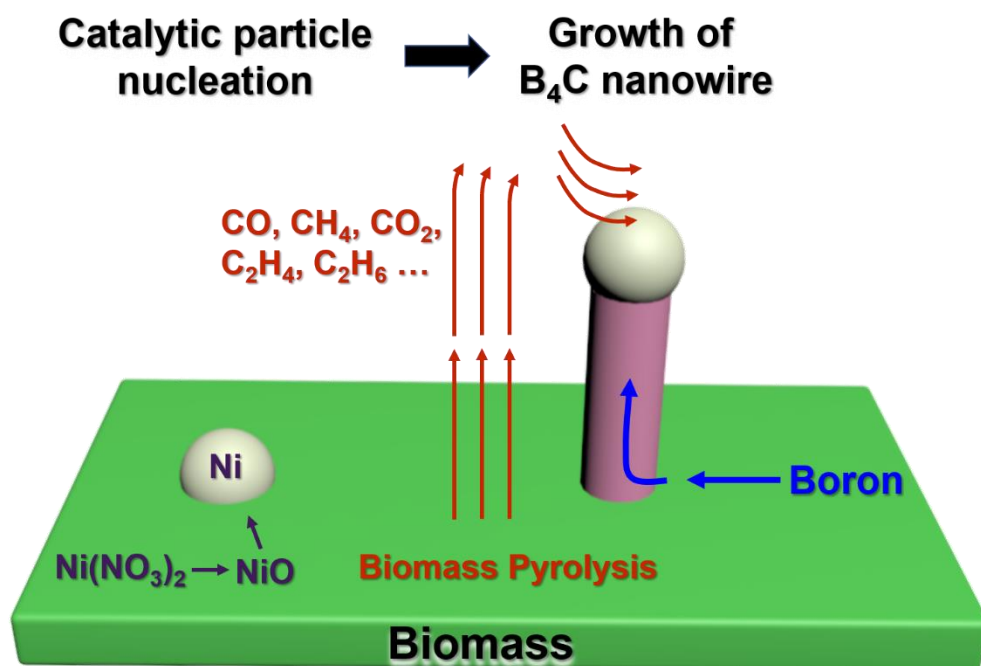


Fig. 2.15. Schematic illustrations of the process of biomass derived boron carbide nanowire growth.

2.6 Conclusion

In summary, the lattice strain fields in boron carbide nanowires were measured via a coupled HRTEM and DIC methodology. The formation enthalpies and lattice parameters of polytypic boron carbides were calculated by DFT, unveiling that the uniformly distributed distortion feature in the lattice strain fields resulted from the transformation between polytypic boron carbides. The energy barriers to boron migration along the nanowire were calculated to be 3.71eV for surface diffusion, and 1.35eV for phase-transformation-assisted mass transport, revealing that polytypic phase transformations play a crucial role in boron carbide nanowire growth. Based on the calculated energy barriers, a volumetric diffusion induced kinetic model was proposed and the corresponding growth rate was calculated. The theoretical results are in good agreement with the experimental data, indicating that the phase

transformation induced kinetic model accurately describes boron carbide nanowire growth. The coupled experimental and theoretical approaches unveil that polytypic phase transformation induced boron migration is the predominant mass transport mechanism in boron carbide nanowire growth. Various biomass materials, including cotton, flour, corn silk, paper towel, and fallen leaf were explored to synthesize boron carbide nanowires. A biomass-enabled boron carbide nanowire growth mechanism was derived from analytical models and experimental results.

Reference

- [1] Ma, R. & Bando, Y. Investigation on the growth of boron carbide nanowires. *Chem. Mater.* **14**, 4403–4407 (2002).
- [2] Madhav Reddy, K. *et al.* Enhanced mechanical properties of nanocrystalline boron carbide by nanoporosity and interface phases. *Nat. Commun.* **3**, 1052 (2012).
- [3] Reddy, K. M., Liu, P., Hirata, A., Fujita, T. & Chen, M. W. Atomic structure of amorphous shear bands in boron carbide. *Nat. Commun.* **4**, (2013).
- [4] Mauri, F., Vast, N. & Pickard, C. J. Atomic structure of icosahedral B₄C boron carbide from a first principles analysis of NMR spectra. *Phys. Rev. Lett.* **87**, 85506 (2001).
- [5] Huang, Y. *et al.* Fabrication of patterned boron carbide nanowires and their electrical, field emission, and flexibility properties. *Nano Res.* **5**, 896–902 (2012).
- [6] McIlroy, D. N. *et al.* Electronic and dynamic studies of boron carbide nanowires. *Phys. Rev. B* **60**, 4874–4879 (1999).
- [7] Zhang, H. Z. *et al.* Boron carbide nanowires with uniform CN_x coatings. *New J. Phys.* **9**, 13 (2007).
- [8] Ma, R. & Bando, Y. High purity single crystalline boron carbide nanowires. *Chem. Phys. Lett.* **364**, 314–317 (2002).
- [9] Pankoke, V., Sakong, S. & Kratzer, P. Role of sidewall diffusion in GaAs nanowire growth: A first-principles study. *Phys. Rev. B* **86**, 1–7 (2012).
- [10] Dubrovskii, V. G. & Hervieu, Y. Y. Diffusion-induced growth of nanowires: Generalized boundary conditions and self-consistent kinetic equation. *J. Cryst. Growth* **401**, 431–440 (2014).
- [11] Nagashima, K., Yanagida, T., Oka, K., Tanaka, H. & Kawai, T. Mechanism and control of sidewall growth and catalyst diffusion on oxide nanowire vapor-liquid-solid growth. *Appl. Phys. Lett.* **93**, 91–94 (2008).

- [12]Dubrovskii, V. G. Length distributions of nanowires: Effects of surface diffusion versus nucleation delay. *J. Cryst. Growth* **463**, 139–144 (2017).
- [13]Wagner, R. S. & Ellis, W. C. Vapor-liquid-solid mechanism of single crystal growth. *Appl. Phys. Lett.* **4**, 89–90 (1964).
- [14]Suarez-Martinez, I., El-Barbary, A. A., Savini, G. & Heggie, M. I. First-principles simulations of boron diffusion in graphite. *Phys. Rev. Lett.* **98**, 3–6 (2007).
- [15]Ittermann, B. *et al.* Diffusion of Boron in Copper by Direct-Exchange Mechanism. *Phys. Rev. Lett.* **77**, 4784–4787 (1996).
- [16]Domnich, V., Reynaud, S., Haber, R. A. & Chhowalla, M. Boron carbide: Structure, properties, and stability under stress. *J. Am. Ceram. Soc.* **94**, 3605–3628 (2011).
- [17]Duncan, T. M. The distribution of carbon in boron carbide: A ^{13}C nuclear magnetic resonance study. *J. Am. Chem. Soc.* **106**, 2270–2275 (1984).
- [18]Tallant, D. R., Aselage, T. L., Campbell, A. N. & Emin, D. Boron carbide structure by Raman spectroscopy. *Phys. Rev. B* **40**, 5649–5656 (1989).
- [19]Bouchacourt, M. & Thevenot, F. Analytical investigations in the B-C system. *J. Less Common Met.* **82**, 219–226 (1981).
- [20]Jiménez, I. *et al.* Photoemission and x-ray-absorption study of boron carbide and its surface thermal stability. *Phys. Rev. B* **57**, 13167–13174 (1998).
- [21]Sutton, M. A., Yan, J. H., Tiwari, V., Schreier, H. W. & Orteu, J. J. The effect of out-of-plane motion on 2D and 3D digital image correlation measurements. *Opt. Lasers Eng.* **46**, 746–757 (2008).
- [22]Sun, Y. *et al.* Atomic-scale imaging correlation on the deformation and sensing mechanisms of SnO_2 nanowires. *Appl. Phys. Lett.* **105**, 243105 (2014).
- [23]Kay, M. I., Young, R. A. & Posner, A. S. Crystal structure of hydroxyapatite. *Nature* **204**, 1050–1052 (1964).

- [24]Lazzari, R., Vast, N., Besson, J. M., Baroni, S. & Dal Corso, A. Atomic structure and vibrational properties of icosahedral B₄C boron carbide. *Phys. Rev. Lett.* **83**, 3230–3233 (1999).
- [25] Tao, X. *et al.* B₄C-nanowires/carbon-microfiber hybrid structures and composites from cotton T-shirts. *Adv. Mater.* **22**, 2055–2059 (2010).
- [26] Hong, N., Langell, M. A., Liu, J., Kizilkaya, O. & Adenwalla, S. Ni doping of semiconducting boron carbide. *J. Appl. Phys.* **107**, (2010).
- [27] Caretti, I., Gago, R., Albella, J. M. & Jiménez, I. Boron carbides formed by coevaporation of B and C atoms: Vapor reactivity, B_xC_{1-x} composition, and bonding structure. *Phys. Rev. B* **77**, 174109 (2008).
- [28]Fu, X., Jiang, J., Liu, C. & Yuan, J. Fivefold twinned boron carbide nanowires. *Nanotechnology* **20**, 365707 (2009).
- [29]Morosin, B., Kwei, G. H., Lawson, A. C., Aselage, T. L. & Emin, D. Neutron powder diffraction refinement of boron carbides nature of intericosahedral chains. *J. Alloys Compd.* **226**, 121–125 (1995).
- [30] Fanchini, G., McCauley, J. W. & Chhowalla, M. Behavior of disordered boron carbide under stress. *Phys. Rev. Lett.* **97**, 1–4 (2006).
- [31] Clark, S. J. *et al.* First principles methods using CASTEP. *Zeitschrift für Krist.* **220**, 567–570 (2005).
- [32]Wang, D. Y. *et al.* Predicted boron-carbide compounds: A first-principles study. *J. Chem. Phys.* **140**, 224704 (2014).
- [33]Bartl, A., Bohr, S., Haubner, R. & Lux, B. A comparison of low-pressure CVD synthesis of diamond and c-BN. *Int. J. Refract. Met. Hard Mater.* **14**, 145–157 (1996).
- [34]Van Santen, R. A. The Ostwald step rule. *J. Phys. Chem.* **88**, 5768–5769 (1984).
- [35]Ruth, V. & Hirth, J. P. Kinetics of diffusion-controlled whisker growth. *J. Chem. Phys.* **3139**, (2005).
- [36] Johansson, J., Svensson, C. P. T., Mårtensson, T., Samuelson, L. & Seifert, W. Mass transport model for semiconductor nanowire growth. *J. Phys. Chem. B* **109**, 13567–13571 (2005).

- [37] Wacaser, B. A. *et al.* Preferential interface nucleation: An expansion of the VLS growth mechanism for nanowires. *Adv. Mater.* **21**, 153–165 (2009).
- [38] Henkelman, G. & Jónsson, H. Improved tangent estimate in the nudged elastic band method for finding minimum energy paths and saddle points. *J. Chem. Phys.* **113**, 9978–9985 (2000).
- [39] Laidler, K. J. & King, C. M. The development of transition-state theory. *J. Phys. Chem.* **87**, 2657–2664 (1983).
- [40] Mantina, M. *et al.* First-principles calculation of self-diffusion coefficients. *Phys. Rev. Lett.* **100**, 1–4 (2008).
- [41] Schmidt, H., Borchardt, G., Kaitasov, O. & Lesage, B. Atomic diffusion of boron and other constituents in amorphous Si-B-C-N. *J. Non. Cryst. Solids* **353**, 4801–4805 (2007).
- [42] Balluffi, R. W., Allen, S. M. & Carter, W. C. *Kinetics of materials. Wiley-Interscience* (2005).
- [43] Dubrovskii, V. G. *et al.* Gibbs-Thomson and diffusion-induced contributions to the growth rate of Si, InP, and GaAs nanowires. *Phys. Rev. B* **79**, 205316 (2009).
- [44] Dubrovskii, V. G. *et al.* Role of nonlinear effects in nanowire growth and crystal phase. *Phys. Rev. B* **80**, 205305 (2009).

Chapter 3 Tailoring nanocomposite interfaces with graphene to achieve high strength and toughness

3.1 Introduction

Nano-fillers such as nanowires and nanoparticles, which have much larger specific surface areas than micro-fillers, are theoretically predicted to be ideal reinforcements to enable exceptional joint enhancements in strength and toughness. However, nanocomposites have not fulfilled such promise, largely because of the poor interfacial bonding between the fillers and matrix. As one of the third hardest materials known in nature, boron carbide (B_4C) is often prized for its eminent physical and mechanical properties, including low density (2.5 g/cm^3), extreme hardness ($27.4 - 37.7 \text{ GPa}$), and high elastic modulus (460 GPa) [1-4]. However, when used as nano-reinforcements in nanocomposites, B_4C nanowires did not show their entire reinforcing effect, due to the poor dispersion of B_4C nanowires in matrix and the weak interfacial bonding between B_4C nanowires and matrix [5]. Thus, engineering nanocomposite interfaces is key to realize the full potential of nano-fillers in their composites.

Many approaches have been explored to improve nano-filler dispersion and filler-matrix interfacial interaction. Interfacial engineering techniques include the attachment of small molecule surfactants, such as silane coupling agents [6,7], and grafted polymer chains, like polyacrylamide and polystyrene [8,9]. These surface treatments, to a certain extent, mitigated the interfacial problems, the trade-off was the reduction of the nano-filler intrinsic properties and extra treatment cost [10]. In this context, we have a pressing need for seeking a new kind of interface modifier that can simultaneously achieve the homogenous dispersion of nano-fillers and improve interfacial bonding in nanocomposites. Graphene,

on account of its exceptional high crystallinity and mechanical prowess [11-13], has stimulated widespread scientific interest. The recently developed mechanical shear mixing enables at scale production of graphene at low cost, promoting its practical applications, especially in polymer-based composites [14–18]. Graphene’s high specific area and surface dangling bonds make it an excellent interface agent to enhance the bonding between nano-fillers and polymer matrix. However, graphene interface engineering has not been explored.

Here, we report a graphene interface engineering technique which glued B₄C nanowires with epoxy, enabling exceptionally enhancements in both strength and toughness. In specific, high-density B₄C nanowires were obtained via a vapor-liquid-solid (VLS) process [19]. High-quality graphene sheets were converted directly from graphite and simultaneously wrapped onto the B₄C nanowires by shear-mixing. The as-obtained graphene wrapped B₄C-nanowires (graphene@B₄C-NWs) exhibited excellent dispersion in water and epoxy. The 0.2 vol% graphene@B₄C-NW reinforced epoxy composite exhibited joint enhancements in strength (144.2 MPa), elastic modulus (3.5 GPa), and fracture strain (15.0%).

3.2 Synthesis and characterizations of graphene@B₄C-NWs

3.2.1 Experimental methods

All chemicals were purchased from Sigma-Aldrich Company without further treatment. Cotton was used to provide a carbon source to synthesize B₄C NWs on the surface of carbon fibers via the VLS method. A Ni-B emulsion was prepared by mixing 7g of Ni(NO₃)₂·6H₂O (catalyst) and 4g of amorphous boron powders (boron source) into 10ml of ethanol under ultrasonic vibration. The carbon fiber cloths were cut into small pieces, immersed in the Ni-B emulsion, and dried at 70 °C in a preheated

oven for 3 h. The B₄C NWs were synthesized in a horizontal alumina tube furnace (diameter: 60 mm, length: 790 mm). The boron-loaded carbon fiber cloth, sandwiched by two pieces of cotton textile, was placed in the middle of the tube furnace and heated up to 1160 °C and held for 2 h with 300 sccm (standard cubic centimeter) continuous flow of argon. The as-synthesized samples were simply treated by ultrasonication, to peel off B₄C nanowires. Graphene@B₄C-NWs were simply synthesized by shear-mixing. 0.5 g of B₄C nanowire powders and 1.0 g of graphite powders (99.9% purity) were mixed into 200 ml of H₂O and shear-mixed at 3000 rpm at room temperature for 3 hours with a L5M-A shear mixer. The as-obtained suspension was further treated by freeze-drying for composite fabrications. For comparison, graphene alone was fabricated using the shear-mixing method following the same procedure. The graphene and B₄C nanowires were separately used for fabricating graphene epoxy composites and B₄C nanowire epoxy composites as control samples.

The morphology, structure, and composition of the as-synthesized samples were characterized by scanning electron microscopy (SEM, Quanta 650), high-resolution transmission electron microscopy (HRTEM, FEI Titan 80, equipped with electron energy-loss spectroscopy (EELS)), atomic force microscopy (AFM, Dimension Icon with ScanAsyst, Bruker), x-ray diffraction (XRD, PANalytical X'Pert Pro Multi-Purpose Diffractometer (MPD) equipped with Cu K_α radiation ($\lambda = 0.15406$ nm)), X-ray photoelectron spectroscopy (XPS, ULVAC-PHI, Inc.), and InVia Raman microscopy (Raman, Renishaw, at the wavelength of 514 nm).

3.2.2 Results and discussion

First, the B₄C nanowires were uniformly grown on the surface of carbon fiber cloth (Fig. 3.1 (a,b))

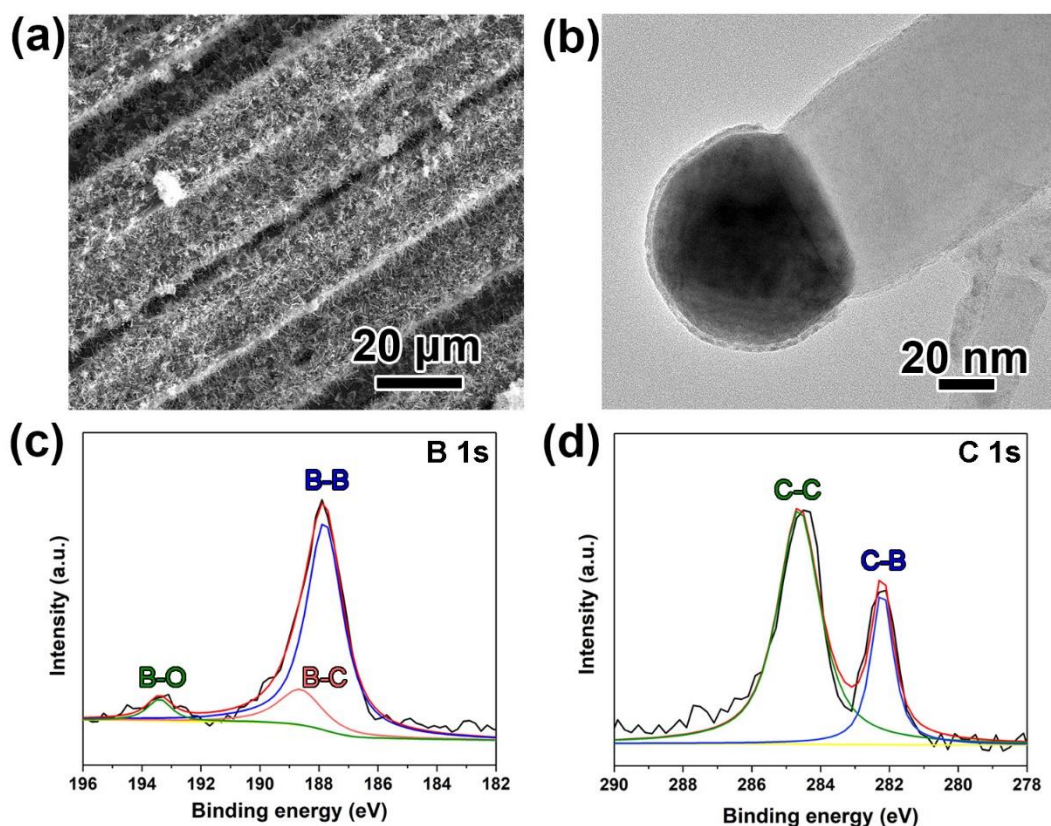


Fig. 3.1. Synthesis and characterization of B_4C nanowires. (a) SEM image of B_4C nanowires grown on the carbon fiber cloth. (b) TEM image of an individual B_4C nanowire. (c) B 1s and (d) C 1s XPS spectra of B_4C nanowires.

via a typical VLS method [19] where cotton served as carbon source, amorphous boron powders as boron source, and $Ni(NO_3)_2 \cdot 6H_2O$ as catalyst [1,20]. The B_4C nanowires of 20-300 nm in diameter and around 5 μm in length (Fig. 3.3 (a)) were then separated from the substrate by ultrasonic vibration. The chemical bonding states in the B_4C nanowires were studied by X-ray photoelectron spectroscopy (XPS). The B 1s peaks revealed the existence of B-B (187.9 eV), B-C (188.7 eV), and B-O (193.4 eV) bonds (Fig. 3.1 (c)). In the C 1s spectra, two peaks centered at 284.5 eV and 282.2 eV were observed, corresponding to C-C and C-B bonds, respectively (Fig. 3.1 (d)) [21]. The atomic ratio of B to C was

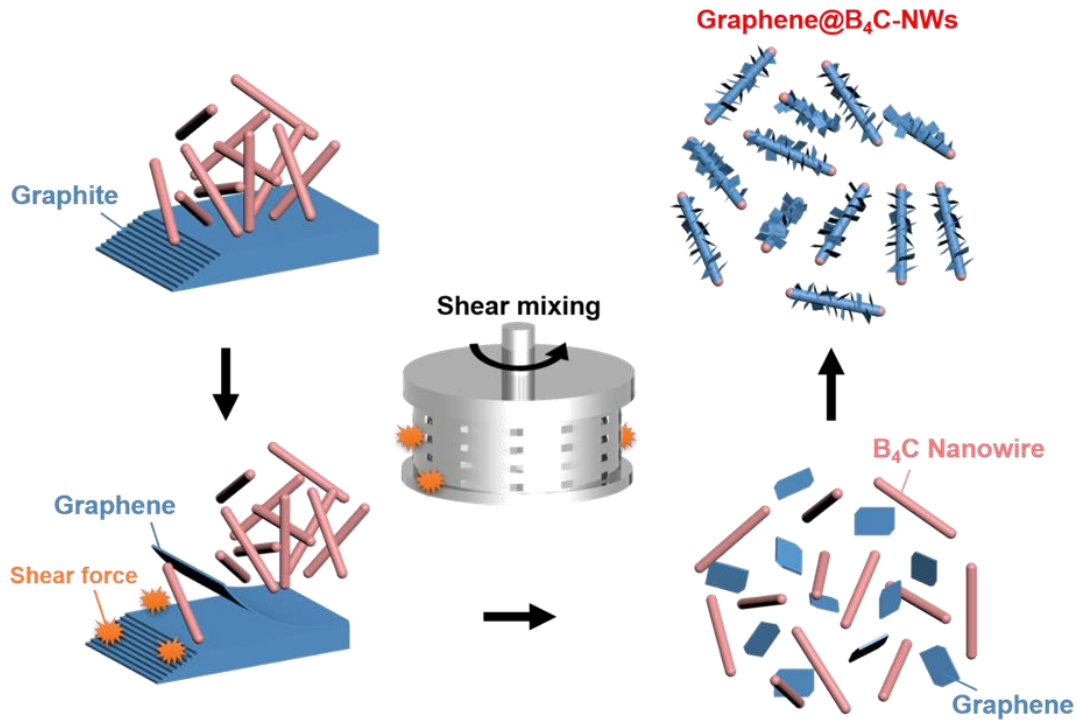


Fig. 3.2. Schematic illustration of the synthesis process steps of graphene@B₄C-NWs.

measured to be 3.56 ± 0.68 , which is in a reasonable range of B₄C stoichiometry, confirming the production of high-quality B₄C nanowires.

The self-assembled graphene wrapped B₄C nanowires (graphene@B₄C-NWs) were directly synthesized by shear mixing the mixture of graphite powders and B₄C nanowires (Fig. 3.2). Transmission electron microscopy (TEM) inspection (Fig. 3.3 (c)) showed that graphite was successfully exfoliated to graphene while B₄C nanowires remained intact in the shear-mixing. The diameter of graphene@B₄C-NWs was increased by 30%-200% compared with pristine B₄C nanowires. Following the same procedure, pristine graphene alone was fabricated using the shear-mixing method and served as the control sample (Fig. 3.3 (b)). To investigate the quality of graphene@B₄C-NWs, the suspension of graphene@B₄C-NWs in dilute water was monitored immediately after shear-mixing without any further treatments (Fig. 3.3

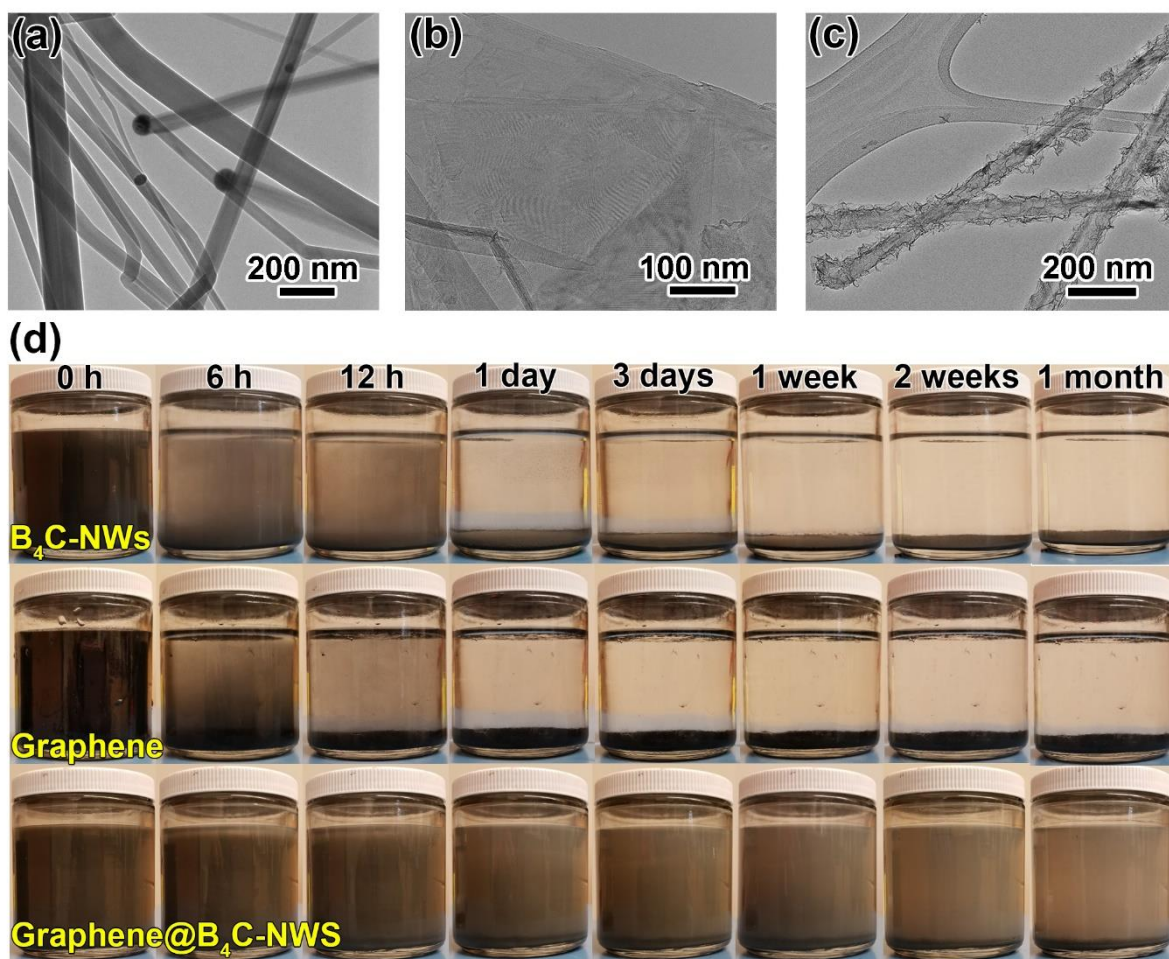


Fig. 3.3. Synthesis of nano-fillers in dilute water by shear mixing. TEM images of (a) B₄C nanowires, (b) multilayered graphene, and (c) graphene@B₄C-NWs. (d) Chronological digital photos of the suspensions of B₄C nanowires, graphene, and graphene@B₄C-NWs.

(d)). By using the same processing, the suspensions of B₄C nanowires and pristine graphene were also prepared for comparison. The above prepared graphene@B₄C-NWs, B₄C-NWs, and graphene were separately dispersed in water, and then the coarse powders which were not thoroughly shear mixed gradually precipitated down to the bottom. At the early stage, the settling rate of the sediments in both graphene and B₄C nanowire suspensions were much larger than the graphene@B₄C-NWs, indicating that

graphene and B₄C nanowires tended to agglomerate in their individual suspensions whereas the graphene@B₄C-NWs exhibited superlative dispersion. Adding B₄C nanowires in the suspension facilitated the exfoliation of graphite and the dispersion of as-synthesized graphene. After 6 h of sedimentation, both graphene and B₄C nanowire suspensions exhibited aggregation and deposition, and after 12 h, they were separated completely into the clean supernatants and the solid residues. In contrast, the graphene@B₄C-NWs remained well-dispersed with little precipitates. In conclusion, graphene sheets were fabricated from graphite together with B₄C nanowires by shear mixing in which graphene sheets were simultaneously self-assembled onto the B₄C nanowire surface.

High-resolution TEM (HRTEM) inspection revealed that graphene sheets were crumpled and self-assembled on the B₄C nanowires (Fig. 3.4 (a)). The graphene on B₄C nanowires showed highly complex wrinkled/crumpled texture. XRD inspection (Fig. 3.4 (b)) revealed three typical diffraction peaks of B₄C, which can be indexed to the (110), (114) and (021) diffractions of rhombohedral boron carbide (JCPDS No. 6-0555). The sharp XRD peak at 26.0° is ascribed to graphene, and other peaks resulted from nickel boride, the catalyst for B₄C nanowire growth. The electron energy loss spectroscopy (EELS) spectrum showed the B(1s) K-edge and the C(1s) K-edge. B₄C crystal lattice has a rhombohedral arrangement consisting of 12-atom icosahedra and 3-atom linear chains ($\bar{R}3m$ space group, $a = 5.16\text{\AA}$, and $\alpha = 65.7^\circ$) [1,22]. Close-up HRTEM observation (Fig. 3.4 (d)) and the Fast Fourier Transform (FFT) pattern with a zone axis $[01\bar{2}]$ (Fig. 3.4 (e)) jointly verified that the B₄C nanowires are of perfect rhombohedral crystalline structure. The measured interplanar spacing of 0.256 nm pointed toward the axial growth plane (121). Raman spectroscopy spectrum Fig. 3.4 (f) displayed peaks that can be ascribed to the

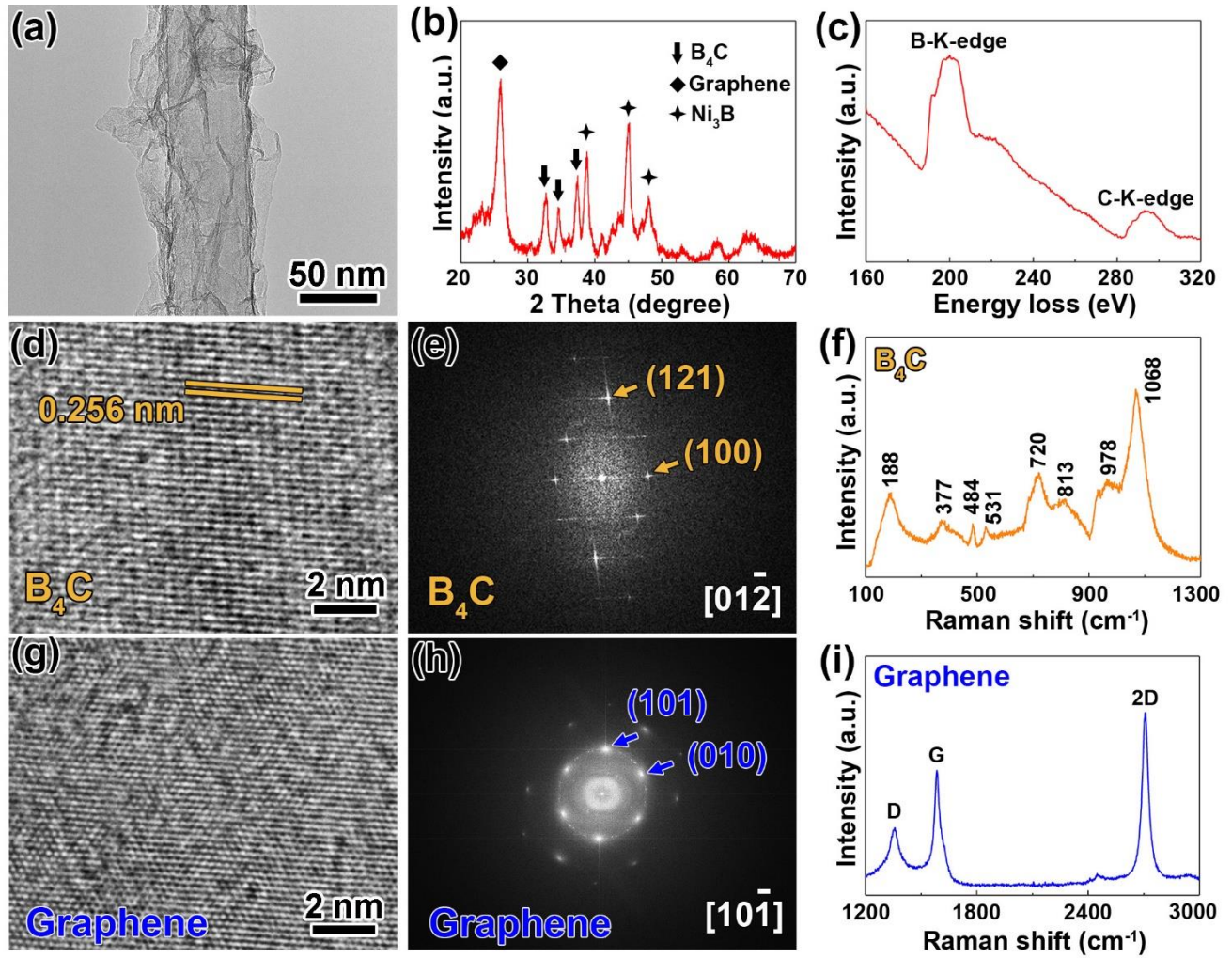


Fig. 3.4. Characterizations of graphene@B₄C-NWs. (a) TEM image, (b) XRD pattern, and (c) EELS of graphene@B₄C-NWs. (d) HRTEM image, (e) the corresponding FFT, and (f) background-corrected Raman spectrum of the B₄C nanowires in graphene@B₄C-NWs. (g) HRTEM image, (h) the corresponding FFT, and (i) background-corrected Raman spectrum of the monolayered graphene in graphene@B₄C-NWs.

intraicosahedral and intericosahedral modes (188, 720, 813, 978, and 1068 cm⁻¹), and the vibrations of chain structures linking icosahedra (377, 484, and 531 cm⁻¹) [23]. The HRTEM image and corresponding FFT pattern of graphene validated that the graphene sheets on B₄C nanowires are of high-quality with monolayered and multilayered features. The presence of monolayered graphene was confirmed by

Raman spectroscopy (Fig. 3.4 (i)), displaying a symmetrical 2D band with a full width at half maximum (FWHM) of 38.1 cm^{-1} and 2D/G intensity ratio of 1.65.

3.3 Mechanical characterizations of graphene@B₄C-NW composites

3.3.1 Experimental methods

The as-obtained fillers (graphene, B₄C nanowires, and graphene@B₄C-NWs) were dispersed into epoxy resin (EPO-TEK, 302-3M, Epoxy Technology Inc.) to fabricate their epoxy composites with the reinforcement content varying from 0.1 to 0.3 vol%. The blend was sonicated for 5 min to degas and then cured for 24 h at 60 °C. Pure epoxy resin, as a control sample, was prepared following the same procedure. The pure epoxy and composites were cut and polished into three-point bending specimens of $40 \times 7 \times 5$ mm (length \times width \times height). Three-point bending tests were carried out using an Admet eXpert 2600

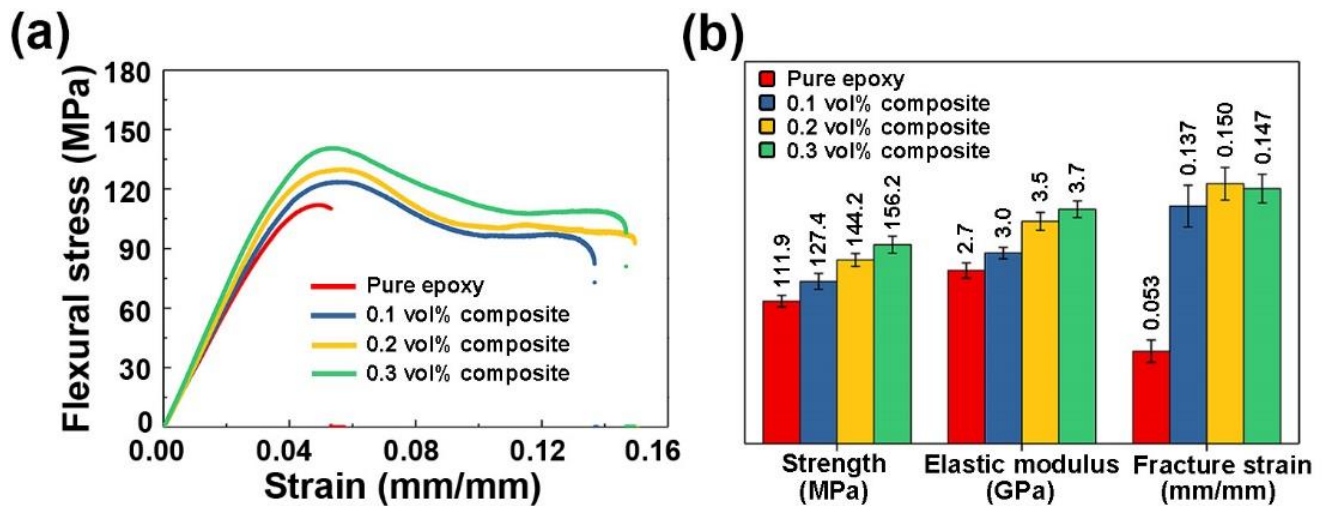


Fig. 3.5. (a) Flexural stress-strain curves of epoxy and graphene@B₄C-NW (0.1 vol%, 0.2 vol% and 0.3 vol%) reinforced composites. (b) Comparison of flexural strength, elastic modulus, and fracture strain for pure epoxy and graphene@B₄C-NW reinforced composites.

tensile universal testing machine with a deflection speed of 5 mm/min.

3.3.2 Results and discussion

The graphene@B₄C-NWs were dispersed into epoxy resin to fabricate epoxy nanocomposites. Three-point bending tests were carried out on the graphene@B₄C-NW composites and epoxy specimens (five beam specimens with the dimension of 40 × 7 × 5 mm (length × width × height) were tested for each material). The typical flexural stress-strain curves (Fig. 3.5 (a)) demonstrate a general trend that the flexural strength and elastic modulus increased with increasing nano-fillers. The pure epoxy sample exhibited a linear elastic stress-strain relationship without having plastic deformation, whereas the graphene@B₄C-NW nanocomposites underwent a large portion of plastic deformation before fracture. The 0.1 vol%, 0.2 vol% and 0.3 vol% graphene@B₄C-NW composites presented the flexural strengths

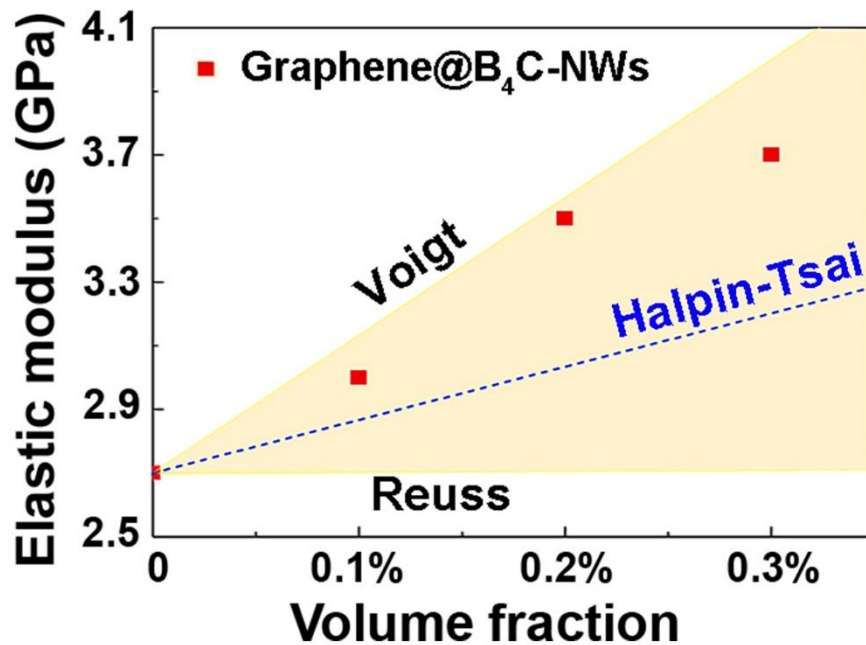


Fig. 3.6. Comparison of experimentally measured (scatter plot) and theoretically predicted elastic modulus values of graphene@B₄C-NW composites.

of 127.4, 144.2 and 156.2 MPa, representing respectively 13.9%, 28.9% and 39.6% amplification over the pure epoxy specimen (111.9 MPa), the elastic moduli of 3.0, 3.5 and 3.7 GPa, 11.1%, 29.6% and 37% enhancement compared with the epoxy control sample (2.7 GPa). The fracture strains of the nanocomposites are approximately increased by 173% (Fig. 3.5 (b)), indicating that the toughness of graphene@B₄C-NW composites is largely enhanced. To evaluate the dispersion quality of graphene@B₄C-NWs, theoretical elastic moduli of the composites were calculated using the Voigt Approximation (upper bound), the Reuss Approximation (lower bound), and the Halpin-Tsai model (empirical model) as following [24,25],

$$\text{Voigt Approximation: } E_c = \nu E_f + (1-\nu)E_m \quad (3.1)$$

$$\text{Reuss Approximation: } \frac{1}{E_c} = \frac{\nu}{E_f} + \frac{1-\nu}{E_m} \quad (3.2)$$

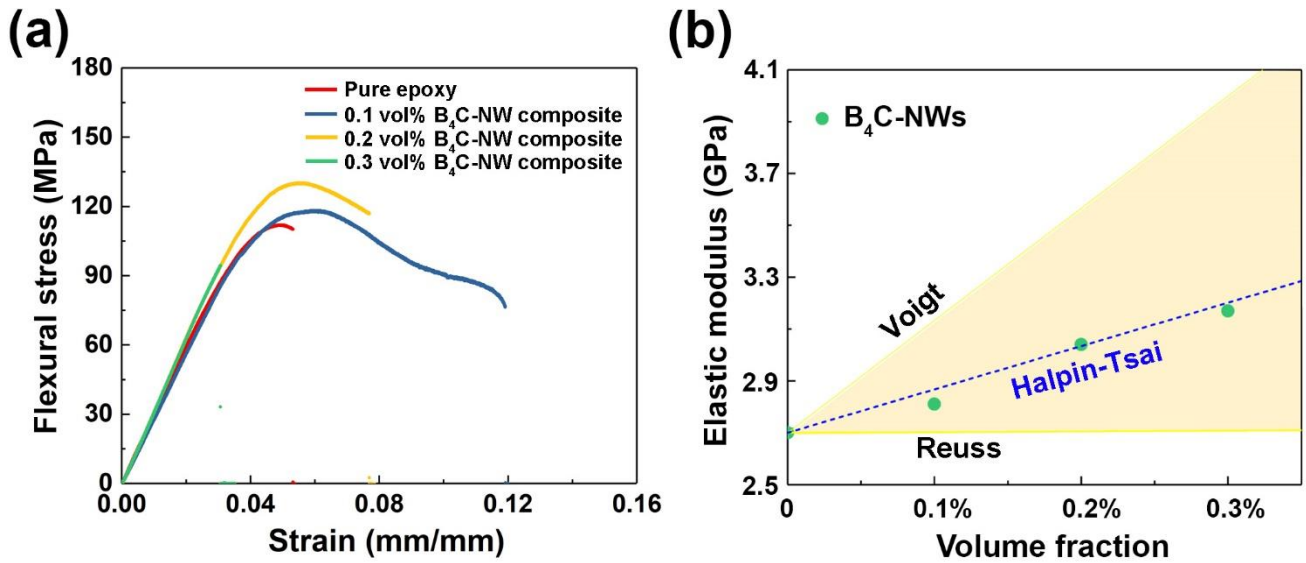


Fig. 3.7. (a) Flexural stress-strain curves of epoxy, B₄C nanowire (0.1 vol%, 0.2 vol% and 0.3 vol%) reinforced composites. (b) Comparison of experimentally measured (scatter plot) and theoretically predicted elastic modulus values.

$$\text{Halpin-Tsai model: } E_c = E_m \left[\frac{3}{8} \frac{1 + \eta_1 (2l_f/d_f) \nu}{1 - \eta_1 \nu} + \frac{5}{8} \frac{1 + 2\eta_2 \nu}{1 - \eta_2 \nu} \right]$$

$$\eta_1 = \frac{E_f/E_m - 1}{E_f/E_m + 2l_f/d_f}, \quad \eta_2 = \frac{E_f/E_m - 1}{E_f/E_m + 2} \quad (3.3)$$

where E_c , E_f , E_m are the elastic moduli of composite, fillers, and matrix, respectively. ν , l_f and d_f represent the volume fraction, length and diameter of the nano-fillers. The elastic moduli of B₄C nanowire [26], graphene [27], and epoxy were given by 435 GPa, 250 GPa and 2.7 GPa, respectively. The elastic modulus of graphene@B₄C-NW was considered to be approximately equal to that of B₄C nanowire. As shown in Fig. 3.6, the elastic moduli of graphene@B₄C-NW composites are much higher than the empirical values and very close to the upper limit. For comparison, graphene sheets and B₄C nanowires were separately dispersed into the epoxy resin and the graphene epoxy and B₄C nanowire epoxy

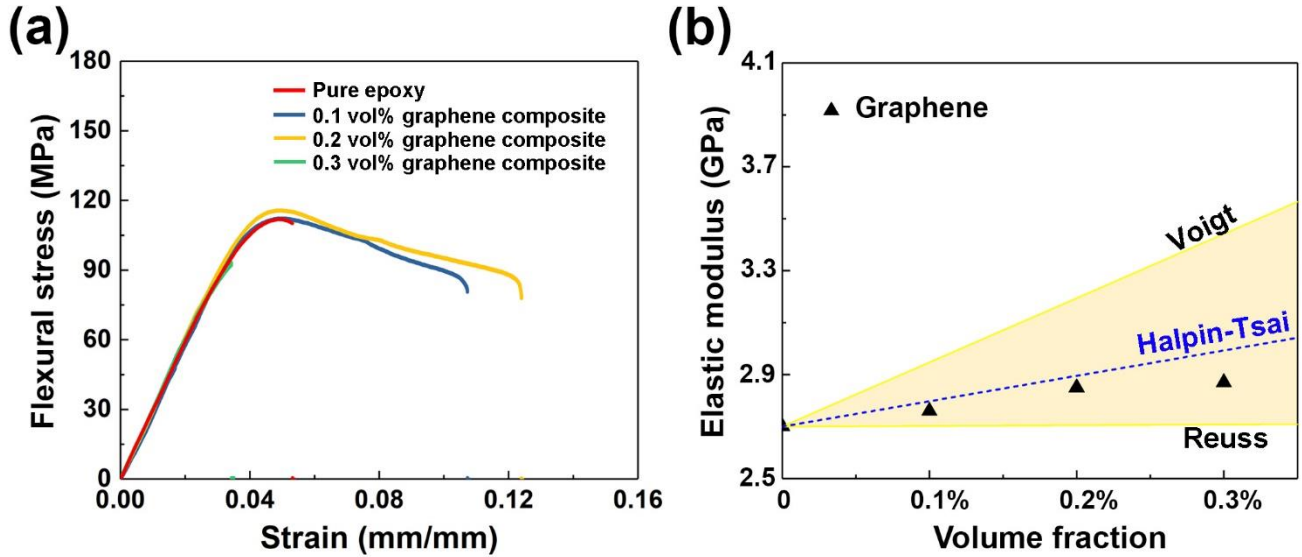


Fig. 3.8. (a) Flexural stress-strain curves of epoxy and graphene (0.1 vol%, 0.2 vol% and 0.3 vol%) reinforced composites. (b) Comparison of experimentally measured (scatter plot) and theoretically predicted elastic modulus values.

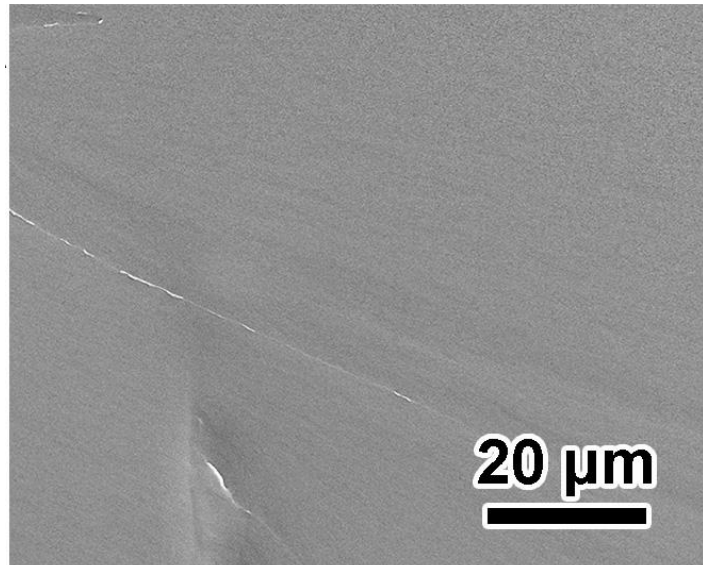


Fig. 3.9. SEM images of the fracture surface of pure epoxy

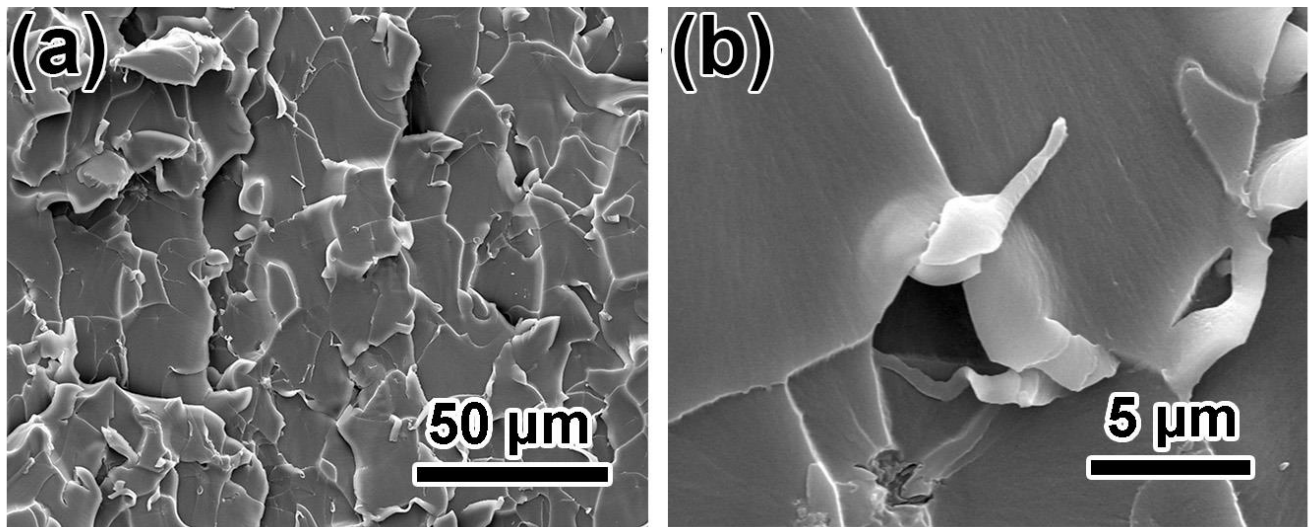


Fig. 3.10. (a) SEM images of the fracture surface of graphene@B₄C-NW reinforced composites. (b) An epoxy covered graphene@B₄C NW protruded out from the composite fracture surface.

composites were characterized by three-point bending (Fig. 3.7 and Fig. 3.8). With a low volume fraction of nano-fillers, both graphene and B₄C nanowire composites exhibited enhanced strength and toughness.

However, the resultant strength and elastic moduli of the B₄C nanowire composites were lower than the

graphene@B₄C-NW composites. All graphene@B₄C-NW (0.1 vol%, 0.2 vol% and 0.3 vol%) reinforced composites exhibited large plastic deformations before failures. However, the plastic deformation regions in the stress-strain diagrams of both graphene and B₄C nanowire composites gradually reduced with increasing nano-filler content and disappeared completely for 0.3 vol% composites, indicating that graphene and B₄C nanowires tended to agglomerate at high volume fractions of reinforcement. To evaluate load transfer efficiencies, the Cox–Krenchel model [28] was applied as following,

$$E_{composite} = \eta_{eff} \nu E_f + (1 - \nu) E_m \quad (3.4)$$

where $E_{composite}$ is the elastic modulus of composite measured by the three-point bending, and η_{eff} is the effective load transfer efficiency factor, involving the filler orientation factor. It turned out that 0.2 vol.% composites achieved their respective highest effective efficiencies, which were calculated to be 39.7%,

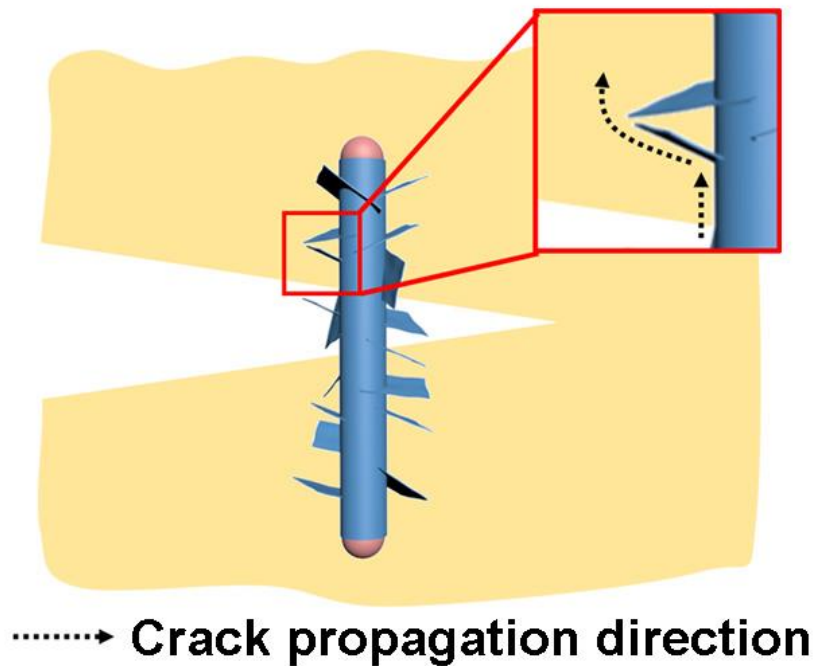


Fig. 3.11. Crack toughening mechanisms in graphene@B₄C-NW composites.

31.0%, and 92.5% for B₄C nanowire, graphene, and graphene@B₄C-NW composites. Impressively, tailoring the composite interfaces with graphene enabled effective utilization of the nano-fillers, resulting in 2 times increase in load transfer efficiency (from 39.7% to 92.5%).

The fractographic analysis was performed to investigate the dispersion quality of nano-fillers with the goal to understand graphene@B₄C-NW strengthening and toughening mechanisms. The pure epoxy control sample showed catastrophic failure with a rather smooth fracture surface (Fig. 3.9), whereas the graphene@B₄C-NW composite exhibited a much rougher fracture surface with “sea-island” like morphology (Fig. 3.10), indicating crack pinning and/or deflection when encountering with the graphene@B₄C-NWs. The frequently observed nanowire pull-out sites suggest that yielding of the matrix around the fillers was first generated, followed by plastic void formation and growth (Fig. 3.10 (b)), and the primary crack derivated when encountering with graphene/B₄C NWs (Fig. 3.11). The debonding of graphene@B₄C-NWs from epoxy consumed more energy. Therefore, crack pinning, deflection,

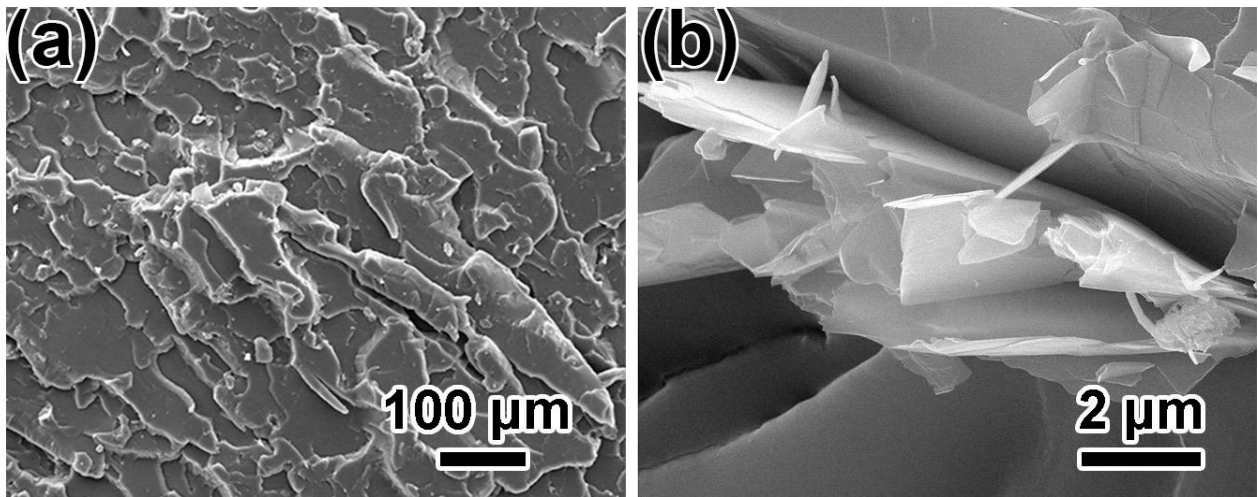


Fig. 3.12. (a) SEM images of the fracture surface of graphene reinforced composites. (b) Graphene agglomerations on the composite fracture surface.

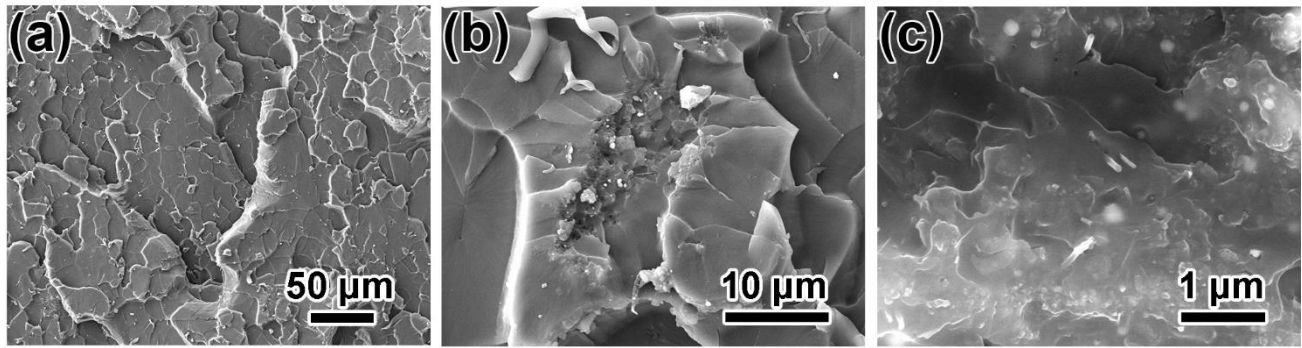


Fig. 3.13. (a) SEM images of the fracture surface of B₄C nanowire reinforced composites. (b) B₄C nanowire agglomerations on the composite fracture surface. (c) B₄C nanowires pulling out from the composite fracture surface.

debonding of graphene@B₄C-NWs from matrix, void formation around the nano-fillers, and nano-filler pull-out jointly contribute to the enhanced toughness of the graphene@B₄C-NW composites. The graphene composites and B₄C nanowire composites exhibited a plethora of large agglomerations on their fracture surfaces (Fig. 3.12 (b) and Fig. 3.13 (b)) which induced microcrack coalescence, promoting the primary crack propagation (Fig. 3.12 (a) and Fig. 3.13 (a)). The pulled-out B₄C nanowires in the B₄C nanowire composites showed smooth surface, suggesting the poor bonding between the B₄C nanowires and matrix (Fig. 3.13 (c)). In sum, graphene rendered nano-fillers better dispersion ability and improved load transfer, leading to joint amplifications in strength and toughness.

3.4 Role of graphene as the tailoring agent of nano-fillers

3.4.1 Methods

Molecular dynamics (MD) simulations were carried out using Large-scale Atomic/Molecular Massively Parallel Simulator (LAMMPS) [29]. B_4C has a rhombohedral unit cell ($R\bar{3}m$ space group, $a = 5.16\text{\AA}$, and $\alpha = 65.7^\circ$) consisting of 12-atom icosahedra and 3-atom linear chains [22,26]. The primary unit cell of graphene is extracted as the monolayer of graphite with hexagonal crystallography structure ($P6_3mc$ space group, $a = b = 2.47\text{\AA}$). The initial atomic configurations were replicated, truncated and combined to serve as the initial input structure (B_4C rod with a diameter of 10\AA and monolayered graphene sheet with the dimension of $50 \times 50\text{\AA}$) for MD simulations. The dangling bonds at the graphene edge were decorated with hydrogen atoms to avoid covalent bonding between two graphene sheets [30]. Periodic boundary conditions were applied in all directions. Boron carbide

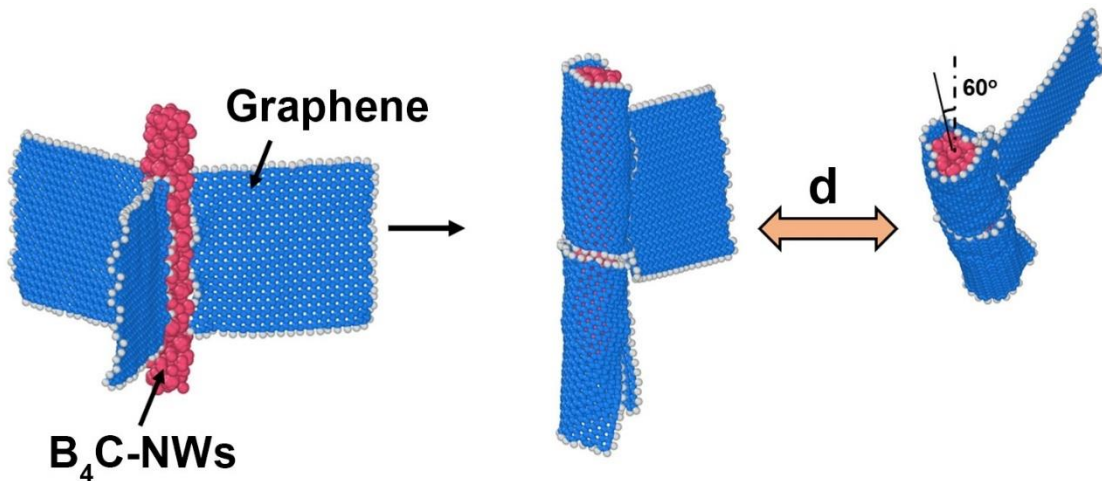


Fig. 3.14. MD snapshots of the atomic configurations representing the process of wrapping graphene around the B_4C nanowire, and the initial structure for calculation the interaction energy.

interactions were described by the reactive force field (ReaxFF) [31], and graphene was modeled by the adaptive intermolecular reactive empirical bond order (AIREBO) potential [32]. The non-bond interactions were described by the LJ potential, and LJ parameters were simply set to be $\epsilon = 2$ meV and $\sigma = 3$ Å, which are in the appropriate range for typical materials. The canonical ensemble (N, V, T) was applied to relax the structure with a time step of 0.25 fs, and the constant temperature was controlled by a Nose-Hoover thermostat method. Simulations temperature was set to be 10 K to ignore the thermal effect. After 500000 MD steps for reaching equilibrium, the as-obtained structures were replicated into

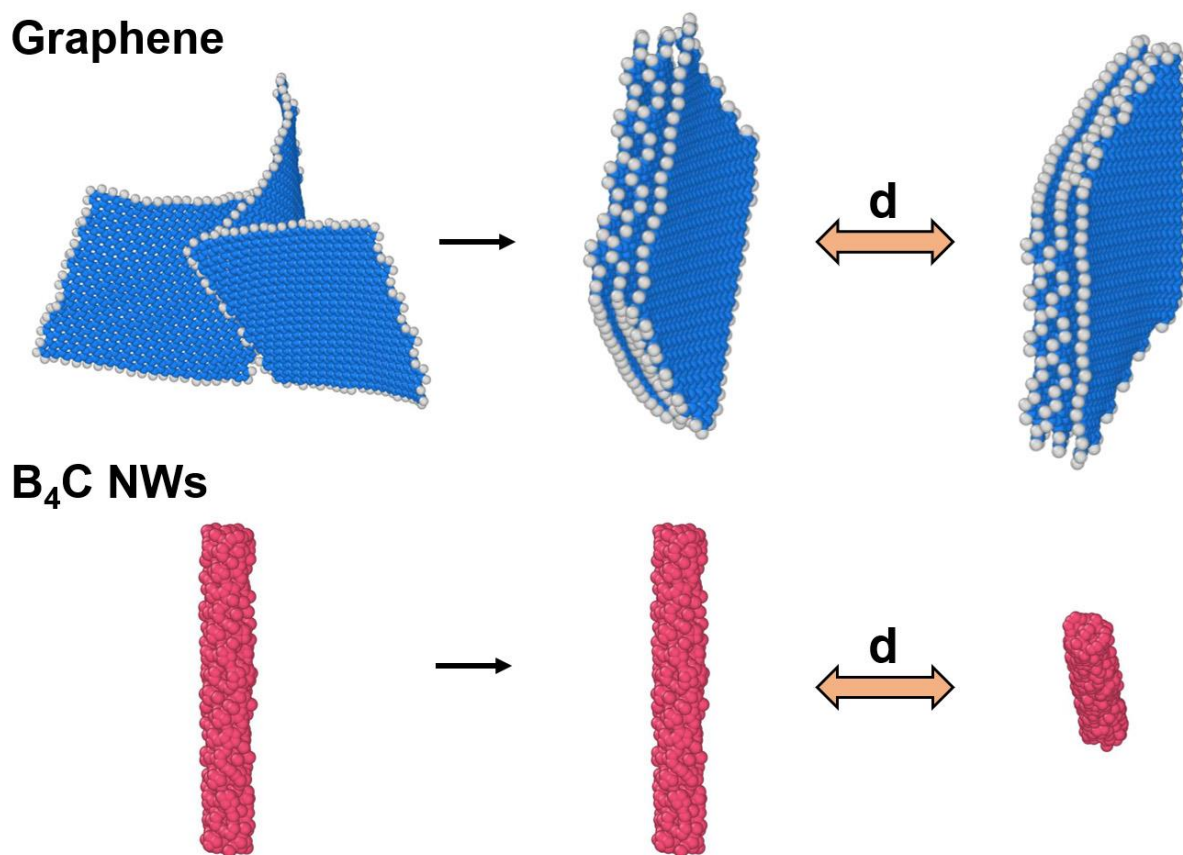


Fig. 3.15. MD snapshots of the atomic configurations representing the process of aggregation of graphene sheets, and the initial structure for calculation the interaction energy of multi-layer graphene and B₄C nanowires.

two structures (graphene/graphene, B₄C-NW/B₄C-NW, or graphene@B₄C-NW/ graphene@B₄C-NW).

The initial distance between the two structures was set to be 100 Å, and the angle to be 60°. By decreasing the distance, the interaction energy between two structures was calculated accordingly.

3.4.2 Results and discussion

Molecular dynamics (MD) simulations were carried out to unveil how graphene sheets edited the B₄C nanowire surface and how graphene facilitated the dispersion of B₄C nanowires. The initial atomic configuration consists of an individual B₄C nanowire and three graphene sheets (Fig. 3.14). The interaction between B₄C and graphene is only described by van der Waals forces (Lennard-Jones

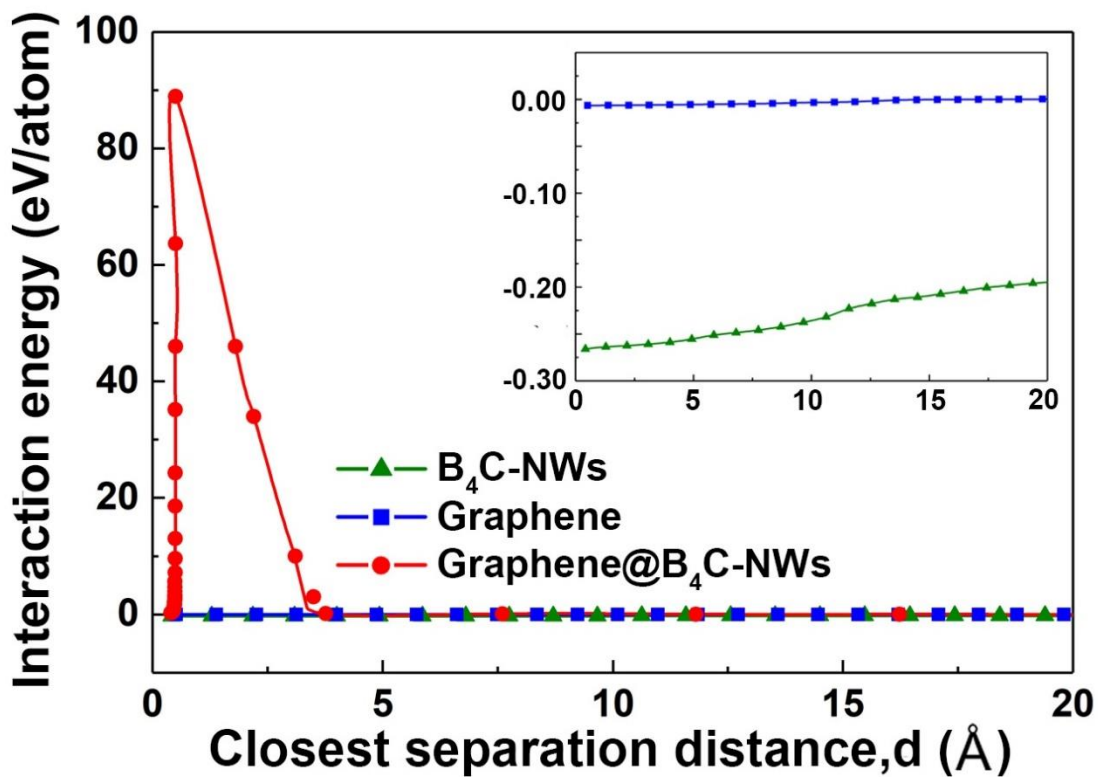


Fig. 3.16. Interaction energy profiles between two nano-fillers (graphene/graphene, B₄C-NW/B₄C-NW, and graphene@B₄C-NW/ graphene@B₄C-NW).

potential). The MD simulation results unveil that the B₄C nanowire remains stable while being blended and wrapped by graphene sheets. After the nanowire is fully wrapped up with graphene, the excess graphene sheet is absorbed in an edge to edge mode, generating a hybrid structure in equilibrium. Without B₄C nanowires, graphene sheets alone aggregate and form multilayered graphene, which is energetically favorable (Fig. 3.15). The interaction energy profiles between the nano-fillers (B₄C nanowires, multilayered graphene sheets, and graphene@B₄C-NWs) are calculated through

$$\phi_{\text{interaction}}(d) = [\phi_{xx}(d) - 2\phi_x]/n \quad (3.4)$$

where $\phi_{\text{interaction}}$ is the normalized interaction energy between two nano-fillers, ϕ_x is the total potential energy of an individual nano-filler (graphene, B₄C-NW, or graphene@B₄C-NW), ϕ_{xx} is the total potential energy of a system with two nano-fillers (graphene/graphene, B₄C-NW/B₄C-NW, or graphene@B₄C-NW/graphene@B₄C-NW), d is the closest separation distance between two nano-fillers, and n is the total atom number in the system. As shown in Fig. 3.16, with decreasing the distance between two nano-fillers, no obvious energy barriers are observed in both the interaction energy profiles of B₄C-NW and graphene, indicating that both graphene sheets and B₄C nanowires tend to agglomerate. In the system of graphene@B₄C-NWs, with decreasing the distance between two graphene@B₄C-NWs, the interaction energy suddenly increases at the position, $d = 3.76 \text{ \AA}$, and gradually reaches the maximum of 89.0 eV/atom. The high energy barrier is enabled by the hybrid structure with the coexistence of graphene sheets and B₄C nanowires. In the process of finding the equilibrium position, graphene sheets and B₄C nanowires move or deform as a unit, and simultaneously interlock each other. Armed with experimental observations, the MD simulations uncover that graphene tailored B₄C nanowires significantly enhance

the interaction energy barrier, making aggregation difficult, and thus largely improving the dispersion performance.

3.5 Conclusion

In summary, graphene sheets were utilized to tailor the interface between B₄C nanowire and epoxy. The graphene wrapped B₄C nanowires (graphene@B₄C-NWs) were directly synthesized by shear mixing the mixture of graphite powders and B₄C nanowires in dilute water. The as-obtained graphene@B₄C-NW suspension exhibited homogeneous dispersion in both water and epoxy, and enhanced load transfer efficiency from the matrix to reinforcements, leading to the overall improved mechanical performance of the composites. In addition, graphene@B₄C-NWs enabled hybrid toughening effects in the epoxy matrix via crack pinning and deflection, debonding of graphene@B₄C-NWs from matrix, void formation around the nano-fillers, and nano-filler pull-out. The 0.2 vol% graphene@B₄C-NW composite exhibited an exceptional combination of mechanical properties in terms of flexural strength (144.2 MPa), elastic modulus (3.5 GPa), and fracture strain (15.0%). This low-cost yet effective technique presents unprecedented opportunities for improving nanocomposite interfaces, enabling high load-transfer efficiency, and opens up a new path for developing strong and tough nanocomposites.

Reference

- [1] Song, N. N. & Li, X. D. Unveiling polytype transformation assisted growth mechanism in boron carbide nanowires. *J. Cryst. Growth* **481**, 11–17 (2018).
- [2] Ma, R. & Bando, Y. High purity single crystalline boron carbide nanowires. *Chem. Phys. Lett.* **364**, 314–317 (2002).
- [3] Song, N. N., Gao, Z., Zhang, Y. Y. & Li, X. D. B₄C nanoskeleton enabled, flexible lithium-sulfur batteries. *Nano Energy* **58**, 30–39 (2019).
- [4] Song, N. N., Zhang, Y. Y., Gao, Z. & Li, X. D. Bioinspired, multiscale reinforced composites with exceptionally high strength and toughness. *Nano Lett.* **18**, 5812–5820 (2018).
- [5] Kuchibhatla, S. V. N. T., Karakoti, A. S., Bera, D. & Seal, S. One dimensional nanostructured materials. *Prog. Mater. Sci.* **52**, 699–913 (2007).
- [6] Zhao, J., Milanova, M., Warmoeskerken, M. M. C. G. & Dutschk, V. Surface modification of TiO₂ nanoparticles with silane coupling agents. *Colloids Surfaces A Physicochem. Eng. Asp.* **413**, 273–279 (2012).
- [7] Rong, M. Z., Zhang, M. Q. & Ruan, W. H. Surface modification of nanoscale fillers for improving properties of polymer nanocomposites: a review. *Mater. Sci. Technol.* **22**, 787–796 (2006).
- [8] Kango, S. *et al.* Surface modification of inorganic nanoparticles for development of organic-inorganic nanocomposites - A review. *Prog. Polym. Sci.* **38**, 1232–1261 (2013).
- [9] Rong, M. Z., Ji, Q. L., Zhang, M. Q. & Friedrich, K. Graft polymerization of vinyl monomers onto nanosized alumina particles. *Eur. Polym. J.* **38**, 1573–1582 (2002).
- [10] Kinloch, I. A., Suhr, J., Lou, J., Young, R. J. & Ajayan, P. M. Composites with carbon nanotubes and graphene: An outlook. *Science* **362**, 547–553 (2018).
- [11] Geim, A. K. & Novoselov, K. S. The rise of graphene. *Nat. Mater.* **6**, 183–91 (2007).

- [12] Lee, C., Wei, X., Kysar, J. W. & Hone, J. Measurement of the elastic properties and intrinsic strength of monolayer graphene. *Science* **321**, 385–388 (2008).
- [13] Zhang, Y. Y., Gao, Z., Song, N. N., He, J. J. & Li, X. D. Graphene and its derivatives in lithium–sulfur batteries. *Mater. Today Energy* **9**, 319–335 (2018).
- [14] Paton, K. R. *et al.* Scalable production of large quantities of defect-free few-layer graphene by shear exfoliation in liquids. *Nat. Mater.* **13**, 624–630 (2014).
- [15] Li, Y. Q., Yu, T., Yang, T. Y., Zheng, L. X. & Liao, K. Bio-inspired nacre-like composite films based on graphene with superior mechanical, electrical, and biocompatible properties. *Adv. Mater.* **24**, 3426–3431 (2012).
- [16] Fang, M., Wang, K., Lu, H., Yang, Y. & Nutt, S. Covalent polymer functionalization of graphene nanosheets and mechanical properties of composites. *J. Mater. Chem.* **19**, 7098–7105 (2009).
- [17] Zhao, X., Zhang, Q., Chen, D. & Lu, P. Enhanced mechanical properties of graphene-based polyvinyl alcohol composites. *Macromolecules* **43**, 2357–2363 (2010).
- [18] Zhang, Y. Y., Song, N. N., He, J., Chen, R. X. & Li, X. D. Lithiation-aided conversion of end-of-life lithium-ion battery anodes to high-quality graphene and graphene oxide. *Nano Lett.* **19**, 512–519 (2019).
- [19] Wagner, R. S. & Ellis, W. C. Vapor-liquid-solid mechanism of single crystal growth. *Appl. Phys. Lett.* **4**, 89–90 (1964).
- [20] Tao, X. *et al.* B₄C-nanowires/carbon-microfiber hybrid structures and composites from cotton t-shirts. *Adv. Mater.* **22**, 2055–2059 (2010).
- [21] Kolel-Veetil, M. K. *et al.* Substitution of silicon within the rhombohedral boron carbide (B₄C) crystal lattice through high-energy ball-milling. *J. Mater. Chem. C* **3**, 11705–11716 (2015).
- [22] Lazzari, R., Vast, N., Besson, J. M., Baroni, S. & Corso, a D. Atomic structure and vibrational properties of icosahedral B₄C boron carbide. *Phys. Rev. Lett.* **83**, 3230–3233 (1999).

- [23] Tallant, D. R., Aselage, T. L., Campbell, A. N. & Emin, D. Boron carbide structure by Raman spectroscopy. *Phys. Rev. B* **40**, 5649–5656 (1989).
- [24] Halpin, J. C. & Kardos, J. L. The Halpin-Tsai equations: A review. *Polym. Eng. Sci.* **16**, 344–352 (1976).
- [25] Aboudi, J., Arnold, S. M. & Bednarczyk, B. A. *Micromechanics of Composite Materials*. Elsevier Inc. (2013).
- [26] Domnich, V., Reynaud, S., Haber, R. A. & Chhowalla, M. Boron carbide: structure, properties, and stability under stress. *J. Am. Ceram. Soc.* **94**, 3605–3628 (2011).
- [27] Papageorgiou, D. G., Kinloch, I. A. & Young, R. J. Mechanical properties of graphene and graphene-based nanocomposites. *Prog. Mater. Sci.* **90**, 75–127 (2017).
- [28] Lee, K. Y. & Bismarck, A. Bacterial nanocellulose as reinforcement for polymer matrices. in *Bacterial Nanocellulose: From Biotechnology to Bio-Economy*. (Elsevier, 2016).
- [29] Plimpton, S. Fast Parallel Algorithms for short-range molecular dynamics. *J. Comput. Phys.* **117**, 1–19 (1995).
- [30] Zhang, Y., Liu, Q. & Xu, B. Self-folding mechanics of surface wettability patterned graphene nanoribbons by liquid evaporation. *J. Appl. Mech.* **85**, 021006 (2017).
- [31] An, Q. & Goddard, W. A. Atomistic origin of brittle failure of boron carbide from large-scale reactive dynamics simulations: suggestions toward improved ductility. *Phys. Rev. Lett.* **115**, 105501 (2015).
- [32] Stuart, S. J., Tutein, A. B. & Harrison, J. A. A reactive potential for hydrocarbons with intermolecular interactions. *J. Chem. Phys.* **112**, 6472–6486 (2000).

Chapter 4 Bioinspired, multiscale boron carbide filler reinforced composites

4.1 Introduction

Biological materials often possess superlative properties [1,2] which are still beyond the reach of man-made materials. One of the best examples is nacre (mother-of-pearl), commonly referred to as nature's armor. Nacre is renowned for its unusual combination of strength and toughness. With only two constituent materials – aragonite and biopolymer cemented in a brick-mortar architecture, nacre exhibits several times enhancement in strength and thousand times amplification in toughness [2-5]. However, it has been proven that simply cloning the brick-mortar architecture in engineering materials cannot reproduce nacre's accomplishments, because nature employs multiple multiscale reinforcing principles in nacre to achieve such exceptional mechanical prowess. The micro reinforcements (the aragonite bricks) act as in-plane load carriers while the nano-reinforcements (the nanoasperities/nanobridges on nacre's brick surfaces) lift the out-of-plane performance. Such hierarchical architecture facilitates the filler/matrix interfacial load transfer. Due to the large span of length scales and the overall complexity of nacre, the development of engineering biomimetic composites has been largely hampered by the lack of micro/nano hybrid reinforcements [2]. Engineering composites often rely on employing reinforcements such as micro- or nano-fillers in a relatively soft matrix. However, simultaneously adding both micro- and nano-reinforcements in a matrix material remains challenging since nano-fillers tend to loosely adhere (agglomerate) onto micro-fillers, decreasing their reinforcing effects. An immediate question is raised: how to achieve multiscale (both micro- and nano-scales) reinforcing effects simultaneously in the matrix material? Can we achieve multiple reinforcing mechanisms using only one type of reinforcements?

In this context, we have a pressing need for seeking new kinds of fillers with both micro- and nano-characteristics (for instance, nanowires decorated microplatelets), with the goal of replicating nature's multiscale reinforcing mechanisms in engineering composites.

Boron carbide (B_4C), one of the third hardest materials known to man, is a promising reinforcement for composites. B_4C possesses appealing physical and mechanical properties such as a low density (2.5 g/cm^3), high melting point (exceeding $2400 \text{ }^\circ\text{C}$), extreme hardness ($27.4 - 37.7 \text{ GPa}$), high elastic modulus (460 GPa), chemical inertness, high thermal stability, and a high capture section for neutrons [6-8]. These properties make B_4C a promising material for numerous applications such as lightweight armor sustaining extreme conditions, abrasives, electronics, and neutron absorbers in nuclear reactors [7,9]. Furthermore, armed with a unique rhombohedral crystal structure, B_4C at reduced dimensions, especially 1-dimensional, often exhibits novel properties [9] such as large specific surface area and high mechanical strength close to its theoretical value [10]. However, the outstanding properties make the multiscale structural design and hierarchical morphology control of B_4C difficult. Although chemical vapor deposition (CVD) [11], plasma-enhanced chemical vapor deposition (PECVD) [12] and carbothermal reduction (CTR) [13] have been used to grow B_4C nanomaterials, synthesizing a B_4C filler with both micro- and nano-characteristics remains a challenge.

In this chapter, multiscale B_4C fillers were designed and synthesized under the guidance of the B_4C growth mechanisms. Epoxy composites reinforced by B_4C fillers were fabricated and characterized by the tensile tester, scanning electron microscopy (SEM) and DIC. Furthermore, an analytical model was built to describe the multiscale reinforced performance of B_4C . In sum, the ultimate goal is to design and

produce lightweight yet strong and tough B₄C reinforced composites.

4.2 Multiscale boron carbide nano-filler fabrication and surface functionalization

4.2.1 Experimental methods

B₄C micro/nano hybrid fillers were synthesized directly on the surface of carbon fibers by loading boron source and catalyst to carbon fiber cloths via dipping and drying processes. Amorphous boron powder and cotton were used as boron and carbon sources, respectively. First, a Ni-B emulsion was produced by dissolving 7 g of Ni(NO₃)₂ · 6H₂O and 4 g of amorphous boron powder into 10 ml of ethanol through ultrasonic vibration. Pieces of carbon fiber cloths were cut into a size of 1 cm × 2 cm and immersed into the Ni-B emulsion. The as-dipped pieces were dried at 70 °C in a preheated oven for 3 h and then transferred to a horizontal alumina tube furnace (diameter: 60 mm, length: 790 mm) to grow B₄C micro/nano hybrid fillers. The nickel- and boron-loaded carbon fibers, clamped by two pieces of

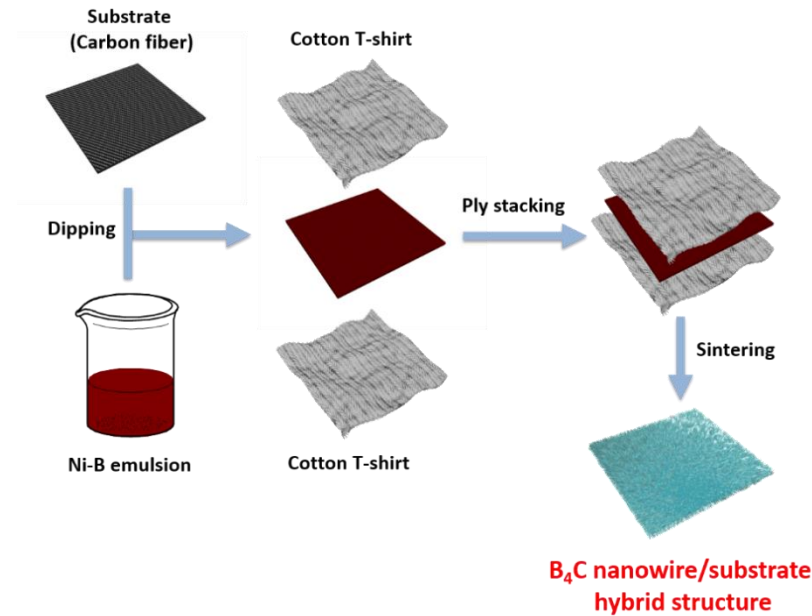


Fig. 4.1. Schematic illustration of the synthesis details of B₄C nanowire/carbon fiber hybrid structure.

cotton textile, as shown in Fig. 4.1, were placed in the middle of the tube furnace and heated to 1160 °C for 4 h with 300 standard cubic centimeters (scm) of a continuous flow of argon at atmospheric pressure. The as-synthesized and annealed samples were characterized by scanning electron microscopy (SEM, Quanta 650), transmission electron microscopy (TEM, 2000FX), x-ray diffraction (XRD, PANalytical X'Pert Pro MPD) and InVia Raman microscopy (Raman, Renishaw). The composition of B₄C nanowires was analyzed by electron energy-loss spectroscopy (EELS).

The as-synthesized samples were simply treated through ultrasonication, in order to peel off the B₄C micro/nano hybrid fillers, which were then characterized by transmission electron microscopy (TEM, 2000FX) and high-resolution transmission electron microscopy (HRTEM, FEI Titan 80). The B₄C micro/nano hybrid fillers were functionalized with PANI by the surface-initiated-polymerization (SIP) method [14,15]. The B₄C micro/nano hybrid fillers (1.78 g), ammonium persulfate (APS, 0.85 g), and cetrimonium bromide (CTAB, 1.51 g) were mixed into 50 mL deionized water and mechanically stirred in an ice-water bath for 1 h. An aniline acid solution (0.465 g aniline in 12.5 mL, 1 mol/L HCl) was added to the above suspension while being stirred for 1 h. The final product was vacuum filtered, washed with deionized water, and dried at 60 °C overnight.

To describe the aniline polymerization process, the atomic configuration was optimized using MD simulations, and the Universal force field (UFF) [16] was implemented to describe the interatomic interactions.

4.2.2 Results and discussion

As shown in Fig. 4.2 (a) and (b), B₄C nanowires were uniformly grown on the carbon fiber cloth by

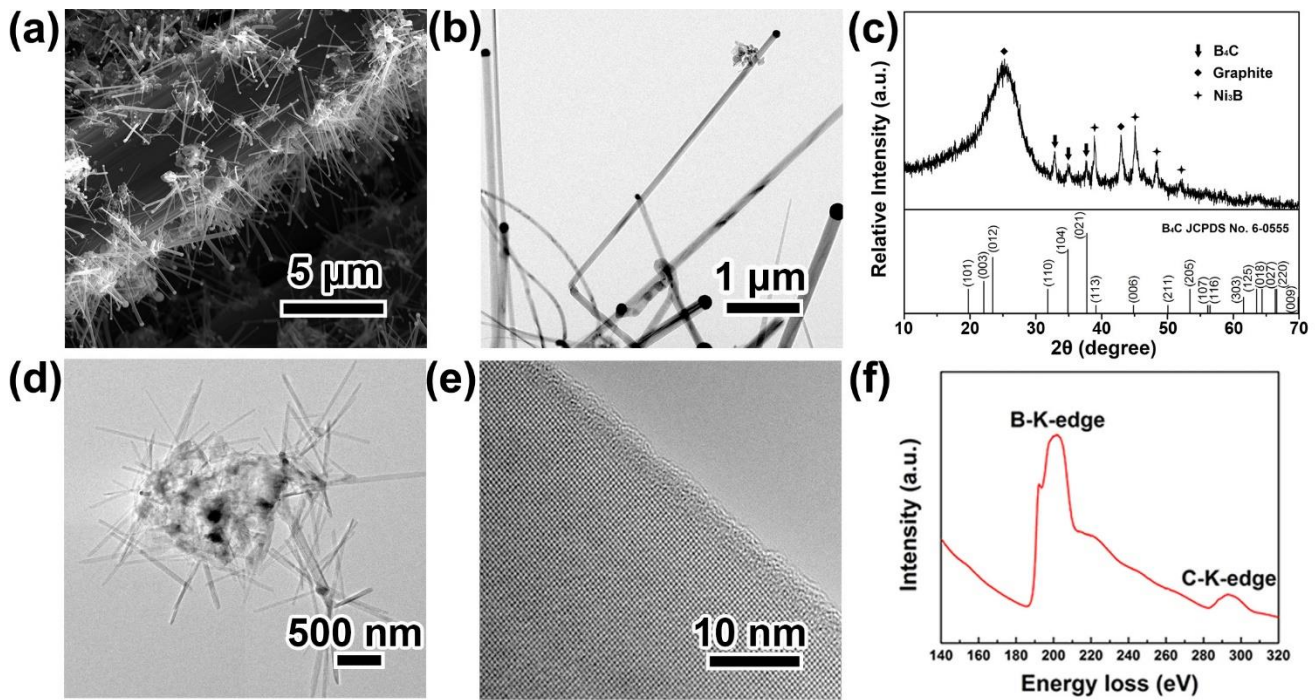


Fig. 4.2. (a) SEM image of the morphology of B₄C micro-/nano-fillers synthesized on carbon fibers. (b) TEM image of B₄C nanowires. (c) XRD pattern of the as-synthesized B₄C micro-/nano-fillers on carbon fibers. (d) TEM image of B₄C micro-/nano-fillers. (e) HRTEM of B₄C micro-/nano-fillers. (f) EELS of B₄C micro-/nano-fillers.

a top-growth mechanism through a typical vapor-liquid-solid (VLS) process [17], where amorphous boron served as source of boron, carbon-rich gases generated from pyrolysis of cotton served as carbon source, and nickel served as a catalyst. During the VLS growth process, catalyst-mediated precipitation led to the axial elongation of nanowires while microplatelets were deposited around the nanowires on the carbon fiber substrate (Fig. 4.3). Each microplatelet with a size of 1 μm×1 μm contains around 20 nanowires which are 50-500 nm in diameter and around 5 μm in length. The typical x-ray diffraction pattern of the unaltered micro/nano hybrid fillers is presented in Fig. 4.2 (c). The peaks at 32.9°, 34.8° and 37.6° can be respectively indexed to (110), (104) and (021) planes of rhombohedral B₄C (JCPDS No. 6-

0555), indicating that the microplatelets and nanowires are of the same material - B₄C. The general peak broadening and shifting were observed because of the existence of nickel [18]. The other peaks resulted from the catalyst and substrate. The EELS spectrum (Fig. 4.2 (f)) revealed two ionization edges corresponding to the characteristic K-edges of boron and carbon, respectively.

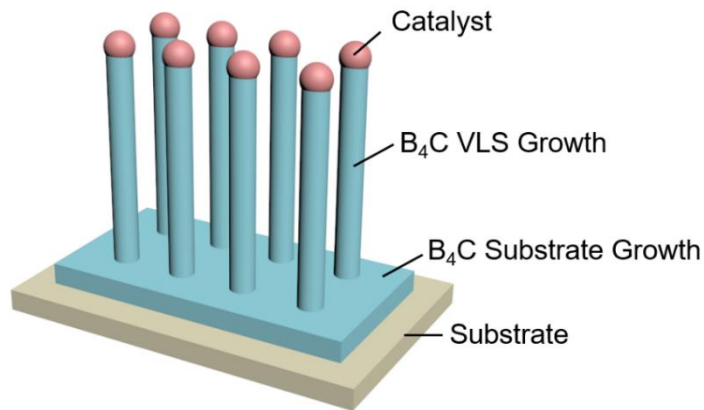


Fig. 4.3. Schematic illustrating the typical B₄C microplatelet/nanowire hybrid fillers grown on the carbon fiber substrate.

The B₄C micro/nano hybrid fillers were released and dispersed by simply processing the unaltered samples using ultrasonication, and characterized by TEM, as shown in Fig. 4.2 (d). The B₄C nanowires, with “smooth surface”, are radially distributed on the B₄C microplatelet. The primary structural unit cell of B₄C has a rhombohedral arrangement ($R\bar{3}m$ space group, $a = 5.16\text{\AA}$ and $\alpha = 65.7^\circ$ [19]), consisting of 12-atom icosahedra and 3-atom linear chains [20,21]. HRTEM inspection (Fig. 4.2 (e)) revealed that B₄C nanowires grew with a perfect crystal lattice that had the axial growth plane ($\bar{2}01$), covered with a layer of amorphous carbon.

After being coated with PANI, B₄C micro-/nano-fillers became rougher (Fig. 4.4(a) and (b)). Raman spectroscopy (Fig. 4.4 (c)) uncovered that the untreated B₄C micro-/nano-fillers (without PANI coating) displayed peaks at 189, 376, 486, 529, 723, 812, 980 and 1067 cm⁻¹, which all correspond to crystalline B₄C [22]. The spectrum below 200 cm⁻¹ and above 600 cm⁻¹ resulted from the intricosahedral and intericosahedral modes. The bands at 376, 486 and 529 cm⁻¹ are ascribed to the vibrations of chain structures linking icosahedra. PANI functionalized B₄C micro-/nano-fillers (Fig. 4.4 (c)) displayed similar Raman peaks with slight offsets, which could be caused by the introduction of PANI. In addition to these peaks from B₄C, typical bands of PANI were also observed, including C-N⁺ stretching vibration

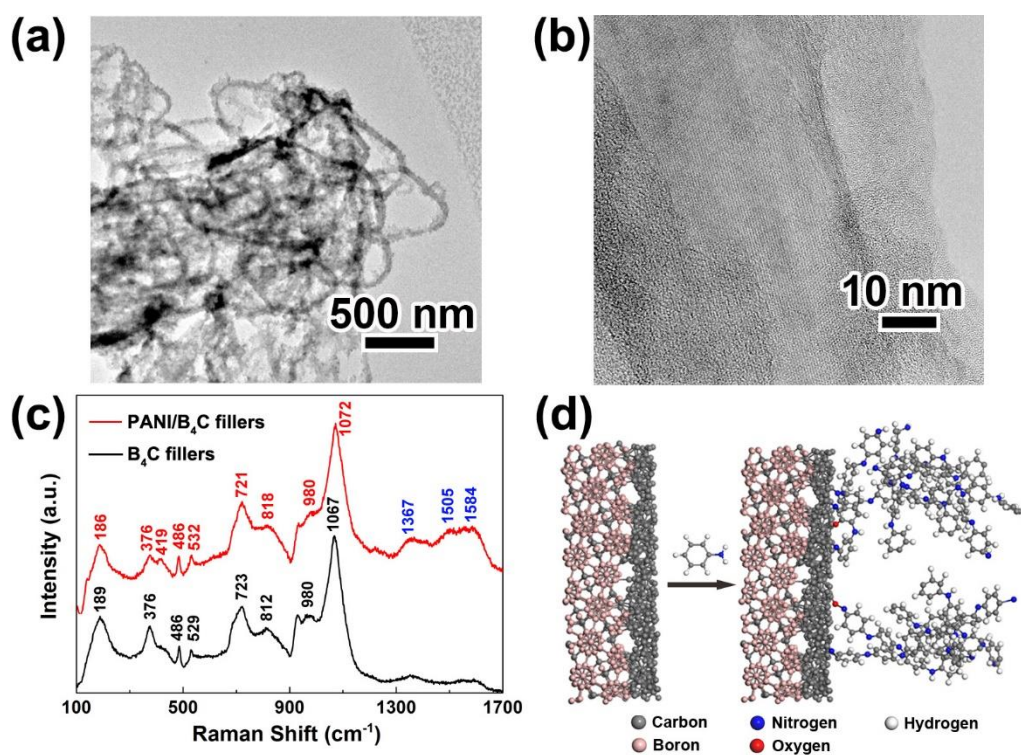


Fig. 4.4. (a) TEM image of PANI functionalized B₄C micro-/nano-fillers. (b) HRTEM image of PANI functionalized B₄C micro-/nano-fillers. (c) Background-corrected Raman spectra of B₄C micro-/nano-fillers excited with a 514-nm wavelength laser line. (d) Polymerization process of PANI and

at 1367 cm^{-1} , C=N stretching at 1505 cm^{-1} and C-C stretching in the benzene ring at 1584 cm^{-1} [23,24]. Clearly, the B₄C micro-/nano-fillers were well functionalized by coating PANI. The general atomic configuration of aniline polymerization was revealed by molecular dynamics (MD) simulations and schematically described in Fig. 4.4(d), showing the adsorption of aniline cation radicals on the B₄C and corresponding polymerization.

4.3 Mechanical characterizations of boron carbide nano-filler reinforced composites

4.3.1 Experimental methods

Both unfunctionalized and functionalized B₄C micro/nano hybrid fillers were dispersed into epoxy resin to fabricate epoxy composites. The reinforcement content was varied from 0.2 to 1 wt.%. The blend was sonicated for 5 min, in order to degas and then cured for 24 h at 60 °C. Following the same procedure described above, pure epoxy resin as a control sample was also prepared and tested for comparison. The

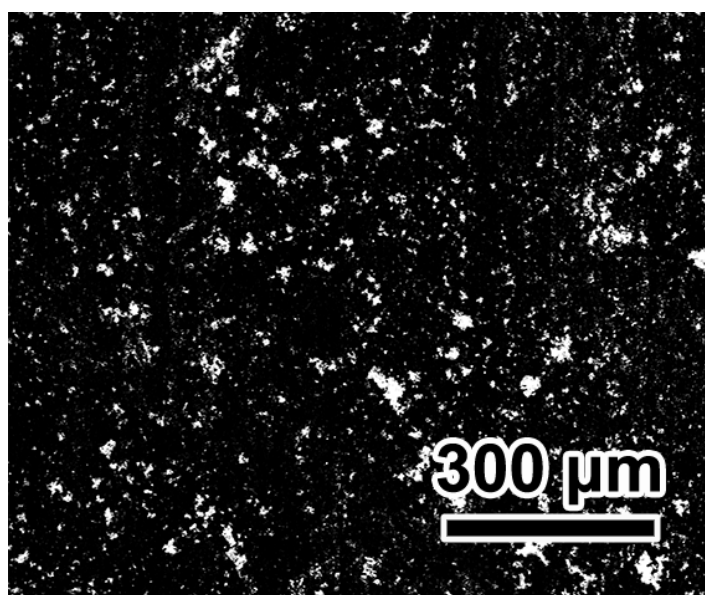


Fig. 4.5. A representative high-contrast CBS SEM image taken during *in situ* tensile test.

composites were stretched with a mechanical tester (MTII SEM tester 1000) *in situ* inside the scanning electron microscope (SEM, Quanta 650) to observe the strain field and the load transfer between the reinforcements and epoxy matrix. The tensile specimens were painted with nickel particles to increase the SEM imaging contrast. The displacements of individual speckles were traced with the SEM circular backscatter detector (CBS) during the *in-situ* SEM tensile testing, and then processed with digital image correlation (DIC) software (Fig. 4.5). In addition to the *in-situ* SEM testing, the composites were mechanically tested on an Instron MicroTester 5848 at a strain rate of 1 mm/min. The fracture surface was examined by SEM. The morphology and area of newly created fracture surface during the tensile test were measured by atomic force microscopy (AFM, Dimension Icon with ScanAsyst, Bruker).

4.3.2 Results and discussion

The unfunctionalized and PANI functionalized B₄C micro-/nano-fillers were separately dispersed into epoxy resin to fabricate B₄C/epoxy composites (Fig. 4.6(a)). The DIC deformation fields along the tensile direction obtained from the *in-situ* SEM tensile testing on pure epoxy, unfunctionalized B₄C micro-/nano-filler reinforced composite, and PANI functionalized B₄C micro-/nano-filler reinforced composite are respectively presented in Fig. 4.6 (b-d). The strain line profiles along the tensile direction are illustrated in Fig. 4.6(e). The pure epoxy sample exhibited relatively uniform deformation (Fig. 4.6 (b)). For unfunctionalized B₄C micro-/nano-filler reinforced composite (Fig. 4.6 (c)), the strain distribution was close to that of the pure epoxy sample (Fig. 4.6 (b)), except that the local region exhibited a slight strain reduction, due to the high stiffness of the reinforcements. The PANI functionalized B₄C micro-/nano-filler reinforced composite (Fig. 4.6 (d)) displayed similar, but even more pronounced

micro-sized strain islands. Generally, due to the high surface-to-volume ratio and van der Waals forces caused by π electrons on the amorphous carbon coating of the B₄C [25,26], the B₄C micro-/nano-fillers tend to agglomerate (specimen ii in Fig. 4.7 (a)) to form bundles/blocks susceptible to the formation of voids and cracks. Therefore, the reinforcing potential of unfunctionalized B₄C micro-/nano-fillers cannot be fully achieved. The dangling carbon bonds on the B₄C amorphous carbon layer are quite reactive and can be stabilized by terminating the dangling bonds with hydrogen, hydroxy or other functional groups [27], enabling PANI to be well polymerized and strongly bonded with the B₄C fillers. Meanwhile, the introduced PANI layer formed covalent bonding with the epoxy matrix, remarkably enhancing the load carrying capacity of the B₄C micro-/nano-fillers. According to the shear-lag theory [28-30], for a discontinuous sheet reinforced composite with perfect bonding interface, strain builds up to a plateau value in the middle of the sheet and then dips down slightly at the edges. Thus, the PANI functionalized B₄C micro-/nano-filler reinforced composite exhibited localized oscillatory strains (Fig. 4.6 (d) and (e)), illustrating that the introduction of PANI coating strengthened the interfacial bonding and accordingly enhanced the load transfer efficiency of the fillers, and furthermore, unveiling that the PANI functionalized B₄C micro-/nano-fillers were dispersed uniformly in the epoxy matrix.

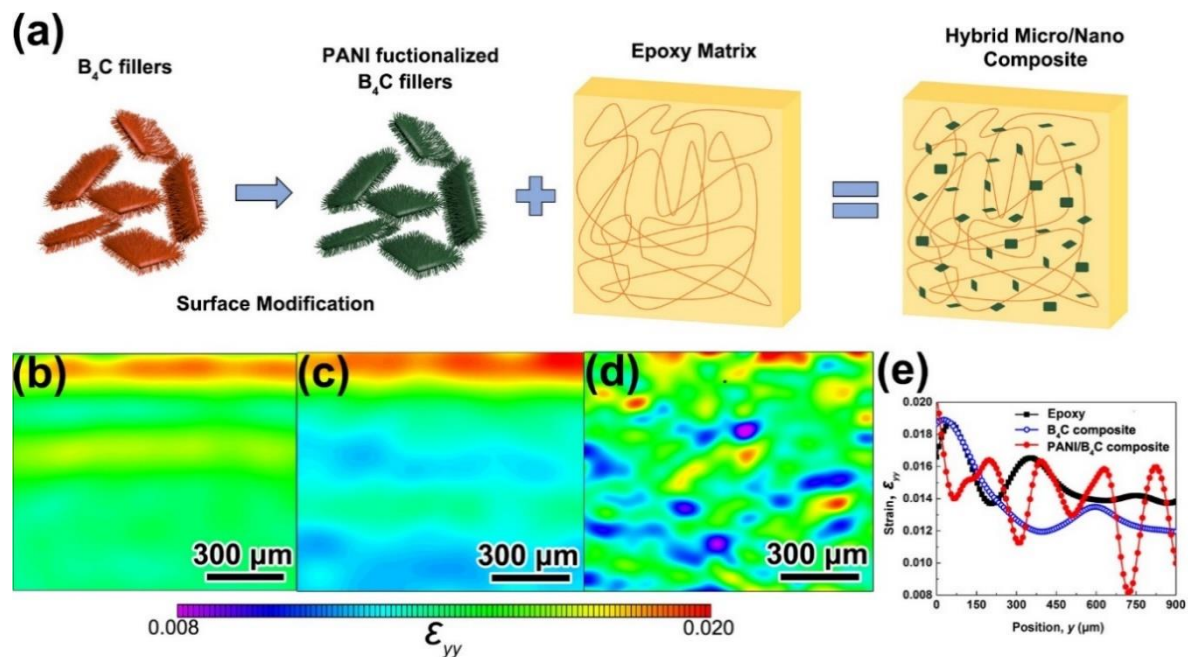


Fig. 4.6. (a) Schematic showing the detailed processes for fabricating PANI functionalized B_4C micro-/nano-filler reinforced epoxy composites. (b-d) DIC strain maps of (b) pure epoxy, (c) unfunctionalized B_4C micro-/nano-filler reinforced composite, and (d) PANI functionalized B_4C micro-/nano-filler reinforced composite. (e) Line profiles of the strains extracted from (b-d) along the tensile direction.

The pure epoxy exhibited a rather smooth fracture surface (Fig. 4.7(b)), a typical feature of the rapid crack propagation of a brittle thermoset polymer [31]. The fracture surface of the B_4C composites, no matter if the reinforcements were treated with PANI or not, were much rougher with sea-wave like patterns (Fig. 4.7 (c) and (d)). The energy consumption during the fracture of the specimens can be evaluated according to the cross-sectional surface area of newly created fractures [32], which were measured by AFM (Fig. 4.8 (a) and (b)). With the same projected area ($10 \mu m \times 10 \mu m$), the fracture surface area of the B_4C composites ($122.6 \mu m^2$) was much larger than that of the pure epoxy ($100.1 \mu m^2$),

indicating more energy consumption before failure. Fiber bridging and pulling-out were observed in the composites (Fig. 4.8 (c) and (d), Fig. 4.9 (e)), suggesting that the B₄C hybrid fillers indeed played the role in reinforcing the matrix [33]. The strength and toughness enhancements of the composites could be attributed to the outstanding strength of B₄C and B₄C/epoxy bonding. Note that the PANI functionalized

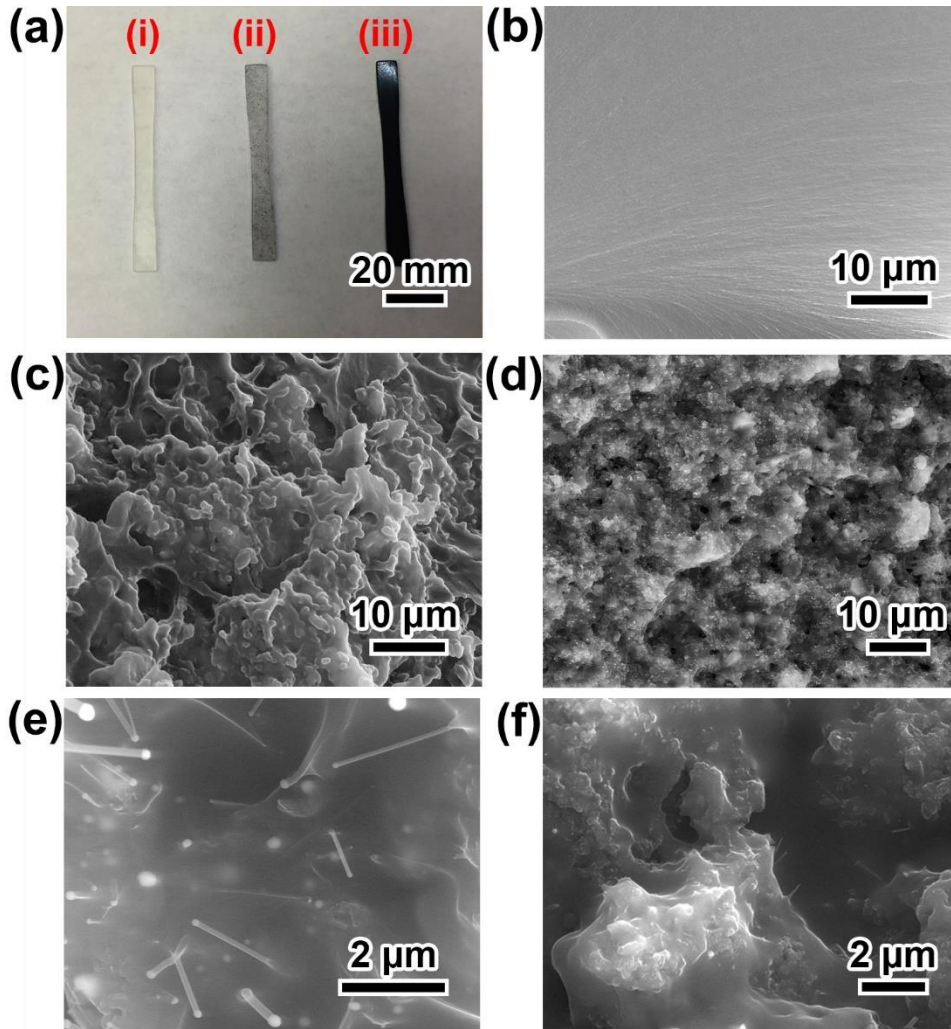


Fig. 4.7. (a) Samples for mechanical testing ((i) epoxy control sample, (ii) unfunctionalized B₄C micro-/nano-filler reinforced composite, (iii) PANI functionalized B₄C micro-/nano-filler reinforced composite). (b) SEM image of the fracture surface of pure epoxy resin. (c) and (e) SEM images of the fracture surface of unfunctionalized B₄C micro-/nano-filler reinforced composite. (d) and (f) SEM images of the fracture surface of PANI functionalized B₄C micro-/nano-filler reinforced composite.

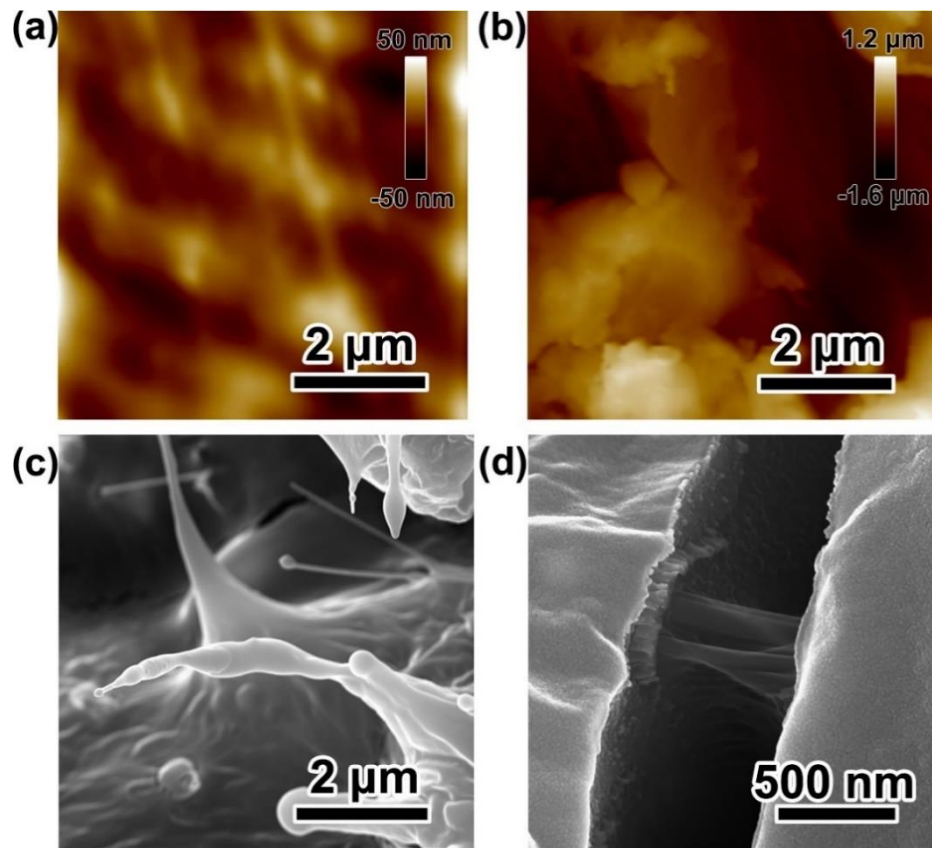


Fig. 4.8. (a) AFM height image of the fracture surface of pure epoxy resin. (b) AFM height image of the fracture surface of unfunctionalized B₄C micro-/nano-filler reinforced composite. (c) SEM image showing pulling-out of B₄C micro-/nano-fillers in the PANI functionalized B₄C composite. (d) SEM image showing B₄C micro-/nano-filler bridging a crack in the PANI functionalized B₄C composite.

B₄C composite showed even rougher fracture surface (Fig. 4.7 (d)). Close-up inspection (Fig. 4.7 (f)) revealed that the PANI functionalized B₄C micro-/nano-fillers were well dispersed in the epoxy matrix, and some broken fillers were visible on the fracture surface where the surrounding epoxy was pulled up, suggesting stronger bonding between the functionalized B₄C and epoxy.

Fig. 4.9 (a) and (b) show the stress-strain curves of B₄C composites and epoxy. The strain was measured and calibrated by DIC [34]. The general trend demonstrated that the tensile strength increased

with increasing B₄C fillers. The 0.2 wt.%, 0.5 wt.% and 1.0 wt.% B₄C composites (without PANI functionalization) exhibited respectively the tensile strengths of 56.0, 67.5 and 77.0 MPa, representing 14.5%, 38.0% and 57.5% enhancement compared to the pure epoxy sample (48.9 MPa), and elastic moduli of 2290.6, 2779.8 and 3329.9 MPa, 17.9%, 43.1%, and 71.5% amplification over the epoxy control sample (1942.1 MPa). The strength and elastic modulus enhancements of untreated B₄C reinforced composites are mainly ascribed to the excellent mechanical properties of B₄C. The toughness

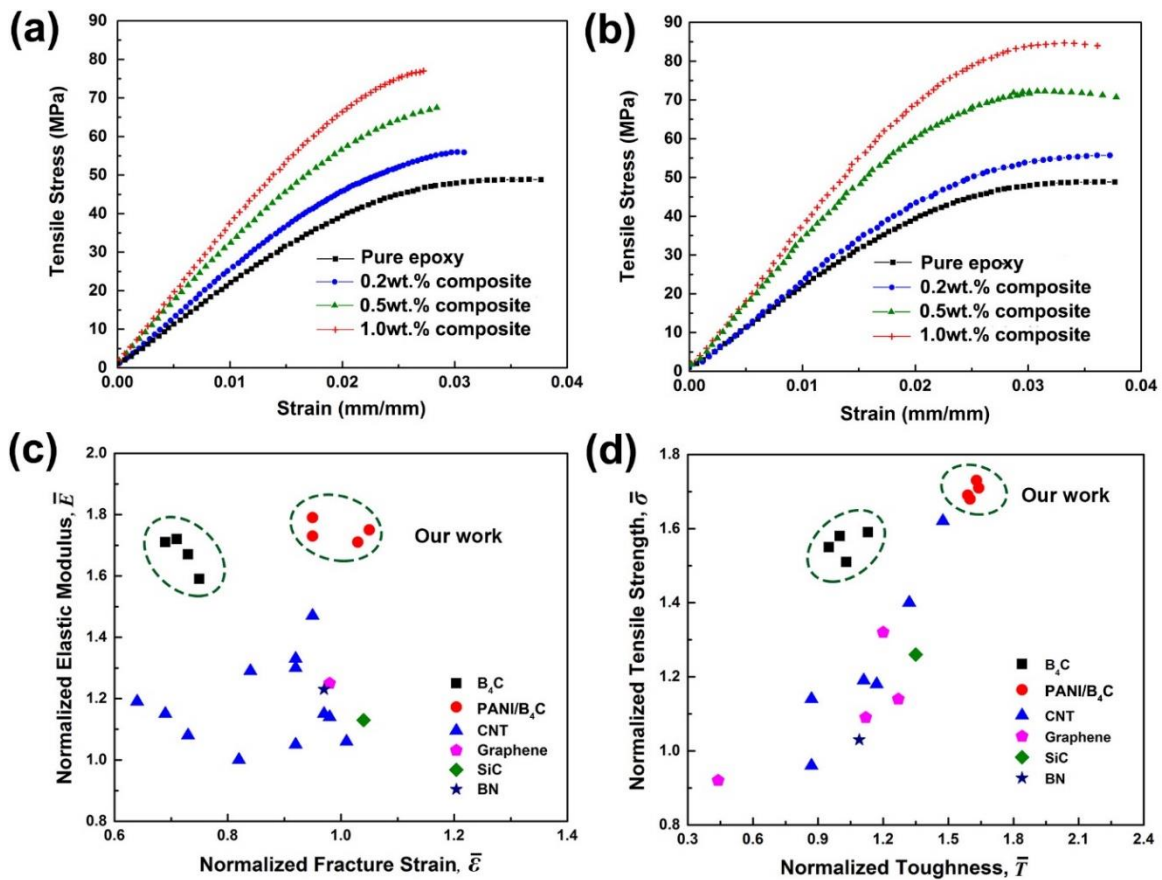


Fig. 4.9. Reinforcing effects of unfunctionalized and functionalized B₄C micro-/nano-fillers (a) Stress-strain curves of untreated B₄C micro-/nano-filler reinforced composites. (b) Stress-strain curves of PANI functionalized B₄C micro-/nano-filler reinforced composites. (c) and (d) Comparison of the mechanical properties of 1 wt.% B₄C composites with other typical polymer composites containing different reinforcements.

(here referred to the area under stress-strain curve), however, appeared to decrease, because of the decreased fracture strain. Whereas, the PANI-functionalized B₄C composites exhibited an exceptional increase in toughness, 8.5%, 51.5%, and 63.1% amplification, respectively, for 0.2 wt.%, 0.5 wt.% and 1.0 wt.% PANI-functionalized B₄C composites over the pure epoxy. Clearly, the PANI coating indeed enhanced the bonding between the B₄C fillers and matrix. Here, PANI acted like the protein in biomaterials, which increases toughness by redistributing stress via the protein networks to avoid crack initiation and propagation at the interface [35]. The enhancements in elastic modulus and strength became pronounced by adding more (over 0.2 wt.%) PANI-functionalized B₄C fillers (Tables 4.1 and 4.2). For comparison, Fig. 4.9 (c) and (d) summarize the elastic modulus, fracture strain, tensile strength, and toughness values of 1 wt.% B₄C/epoxy composites, respectively, which are normalized by dividing the composites' properties by the corresponding properties of pure epoxy. The 1 wt.% B₄C micro-/nano-filler (with/without PANI functionalization) reinforced composites exhibited 70% enhancement in elastic modulus compared with other composites reported in the literature. Importantly, the PANI functionalized B₄C composites demonstrated an exceptional performance of high elastic modulus of 3474 MPa and large fracture strain of 3.5% (Fig. 4.9 (c)), thereby possessing a high strength-toughness combination (Fig. 4.9 (d)).

Table 4.1. Mechanical properties of unfunctionalized B₄C micro/nano-filler reinforced epoxy composites

| Samples | Elastic modulus (MPa) | Strength (MPa) | Toughness(kJ/m ³) | Fracture strain (mm/mm) |
|------------|-----------------------|----------------|-------------------------------|-------------------------|
| Pure epoxy | 1942.1 | 48.9 | 1242.1 | 3.8% |
| 0.2 wt.% | 2290.6 | 56.0 | 1057.9 | 3.1% |
| 0.5 wt.% | 2779.8 | 67.5 | 1154.2 | 2.8% |
| 1.0 wt.% | 3329.9 | 77.0 | 1248.1 | 2.7% |

Table 4.2. Mechanical properties of PANI functionalized B₄C micro/nano-filler reinforced epoxy composites

| Samples | Elastic modulus (MPa) | Strength (MPa) | Toughness(kJ/m ³) | Fracture strain (mm/mm) |
|------------|-----------------------|----------------|-------------------------------|-------------------------|
| Pure epoxy | 1942.1 | 48.9 | 1242.1 | 3.8% |
| 0.2 wt.% | 2182.7 | 55.7 | 1348.2 | 3.7% |
| 0.5 wt.% | 3004.1 | 72.2 | 1882.4 | 3.8% |
| 1.0 wt.% | 3474.4 | 84.7 | 2026.3 | 3.6% |

4.4 Continuum mechanics study of multiscale reinforcements

To elucidate the reinforcing mechanisms of PANI functionalized B₄C reinforced composites, a continuum micromechanics analysis was performed on a representative volume element (RVE). According to our electron microscopy inspection (Fig. 4.2), the B₄C filler consists of a B₄C microplatelet with irregular shape and B₄C nanowires growing in various directions. In order to better describe the B₄C fillers and simplify the modeling process, the multiscale RVE is assumed to be an individual B₄C cylinder

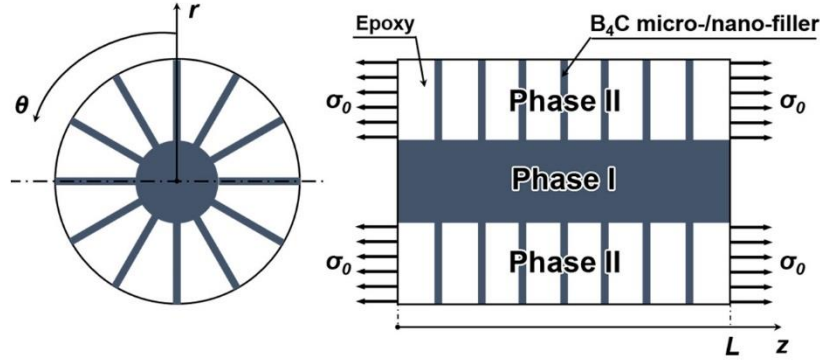


Fig. 4.10. Schematic diagram showing the cross section of the three-phase representative volume element (RVE) for the composites.

(Phase I) surrounded by a sheath of B₄C nanowire/epoxy nanocomposite (Phase II). It is assumed that the Phase II material is reinforced by radially aligned B₄C nanowires, thereby exhibiting orthotropic properties. To investigate the interfacial load transfer, a tensile stress σ_0 was applied to Phase II of the RVE along with z-direction (Fig. 4.10). [36] The axisymmetric governing equations [37], in terms of the polar coordinates (r, θ, z) , include the equilibrium equation in direction z ,

$$\frac{\partial \sigma_{zz}^i}{\partial z} + \frac{1}{r} \frac{\partial (r \sigma_{rz}^i)}{\partial r} = 0 ; i = \text{I and II} \quad (4.1)$$

the geometrical equations,

$$\varepsilon_{zz}^i = \frac{\partial u_z^i}{\partial z}, \quad \varepsilon_{\theta\theta}^i = \frac{u_r^i}{r}, \quad \varepsilon_{rr}^i = \frac{\partial u_r^i}{\partial r}, \quad 2\varepsilon_{rz}^i = \frac{\partial u_z^i}{\partial r} + \frac{\partial u_r^i}{\partial z} ; i = \text{I and II} \quad (4.2 \text{ a-d})$$

and the constitutive equations,

$$\begin{bmatrix} \sigma_{zz}^i \\ \sigma_{\theta\theta}^i \\ \sigma_{rr}^i \\ \sigma_{z\theta}^i \\ \sigma_{rz}^i \\ \sigma_{r\theta}^i \end{bmatrix} = \begin{bmatrix} C_{11}^i & C_{12}^i & C_{13}^i & 0 & 0 & 0 \\ C_{12}^i & C_{22}^i & C_{23}^i & 0 & 0 & 0 \\ C_{13}^i & C_{23}^i & C_{33}^i & 0 & 0 & 0 \\ 0 & 0 & 0 & C_{44}^i & 0 & 0 \\ 0 & 0 & 0 & 0 & C_{55}^i & 0 \\ 0 & 0 & 0 & 0 & 0 & C_{66}^i \end{bmatrix} \begin{bmatrix} \varepsilon_{zz}^i \\ \varepsilon_{\theta\theta}^i \\ \varepsilon_{rr}^i \\ 2\varepsilon_{z\theta}^i \\ 2\varepsilon_{rz}^i \\ 2\varepsilon_{r\theta}^i \end{bmatrix}; \quad i = \text{I and II} \quad (4.3)$$

In Eqs. (4.1-4.3), σ_{mn} and ε_{mn} are stress and strain components, u_r and u_z are, respectively, the radial and axial displacement components, and $[C]$ is the stiffness tensor with the indices 1, 2, 3 denoting the axes z , θ , and r , respectively. i is the material layer ($i = \text{I and II}$). The average axial normal stresses over the cross-section are defined as

$$\langle \sigma_{zz}^I \rangle = \frac{1}{\pi a^2} \int_0^a \sigma_{zz}^I(r, z) (2\pi r) dr, \quad \langle \sigma_{zz}^{II} \rangle = \frac{1}{\pi(R^2 - a^2)} \int_a^R \sigma_{zz}^{II}(r, z) (2\pi r) dr \quad (4.4 \text{ a,b})$$

The boundary conditions for this problem are given by

$$\langle \sigma_{zz}^I \rangle \Big|_{z=0} = \langle \sigma_{zz}^I \rangle \Big|_{z=L} = 0, \quad \sigma_{rr}^{II} \Big|_{r=R} = \sigma_{rz}^{II} \Big|_{r=R} = 0 \quad (4.5 \text{ a,b})$$

Phase I and II are assumed to be perfectly bonded, due to the one-step growth of the B₄C micro-/nano-fillers, and the interfacial continuity conditions are

$$\sigma_{rr}^I \Big|_{r=a} = \sigma_{rr}^{II} \Big|_{r=a}, \quad \sigma_{rz}^I \Big|_{r=a} = \sigma_{rz}^{II} \Big|_{r=a} = \tau_{\text{int}}(z), \quad u_r^I \Big|_{r=a} = u_r^{II} \Big|_{r=a} \quad (4.6 \text{ a-c})$$

where $\tau_{\text{int}}(z)$ is the transverse shear stress at the interface between Phase I and Phase II, a and R are the inner and outer radii of Phase II, respectively, and L is the length of the cylindrical RVE. Also, the force balance of the RVE cylinder along the z -direction is considered,

$$\int_0^a \sigma_{zz}^I 2\pi r dr + \int_a^R \sigma_{zz}^{II} 2\pi r dr = \pi(R^2 - a^2) \sigma \quad (4.7)$$

Making use of Eq. (4.1), (4.4) and (4.6(b)), it can be derived that

$$\frac{d\langle\sigma_{zz}^I\rangle}{dz} = -\frac{2}{a}\tau_{\text{int}}(z), \quad \frac{d\langle\sigma_{zz}^{II}\rangle}{dz} = \frac{2a}{R^2 - a^2}\tau_{\text{int}}(z) \quad (4.8 \text{ a,b})$$

It is assumed that the gradient of σ_{zz} with respect to the axial coordinate (z) is independent of the radial coordinate (r), thus we have

$$\frac{\partial\sigma_{zz}^I}{\partial z} = f(z), \quad \frac{\partial\sigma_{zz}^{II}}{\partial z} = g(z) \quad (4.9 \text{ a,b})$$

where $f(z)$ and $g(z)$ are unknown functions yet to be derived. Substituting (4.9) into (4.1), we have

$$\sigma_{rz}^I = \frac{r}{a}\tau_{\text{int}}(z), \quad \sigma_{rz}^{II} = \frac{a}{a^2 - R^2}\left(r - \frac{R^2}{r}\right)\tau_{\text{int}}(z) \quad (4.10 \text{ a,b})$$

The gradient of radial displacements with respect to z -direction is assumed to be negligible [38],

$$\left|\frac{\partial u_r}{\partial z}\right| \ll \left|\frac{\partial u_z}{\partial r}\right| \quad (4.11)$$

Combining this with Eq. (4.2d), (4.3) and (4.10b) will result in

$$\sigma_{rz}^{II} = \frac{a}{a^2 - R^2}\left(r - \frac{R^2}{r}\right)\tau_{\text{int}}(z) = C_{55}^{II}\frac{\partial u_z^{II}}{r} \quad (4.12)$$

and integrating with respect to r from a to R , we can obtain that

$$\tau_{\text{int}}(z) = C_{55}^{II}\frac{a^2 - R^2}{a}\frac{1}{\frac{1}{2}(R^2 - a^2) - R^2 \ln \frac{R}{a}}\left[u_z^{II}\Big|_{r=R} - u_z^{II}\Big|_{r=a}\right] \quad (4.13)$$

Substituting Eq. (4.13) into Eq. (4.10b) and (4.12) then gives

$$\sigma_{rz}^{II} = C_{55}^{II}\frac{\left[u_z^{II}\Big|_{r=R} - u_z^{II}\Big|_{r=a}\right]}{\frac{1}{2}(R^2 - a^2) - R^2 \ln \frac{R}{a}}\left(r - \frac{R^2}{r}\right) \quad (4.14)$$

$$u_z^{II} = u_z^{II}\Big|_{r=a} + \frac{\frac{1}{2}(r^2 - a^2) - R^2 \ln \frac{r}{a}}{\frac{1}{2}(R^2 - a^2) - R^2 \ln \frac{R}{a}}\left[u_z^{II}\Big|_{r=R} - u_z^{II}\Big|_{r=a}\right] \quad (4.15)$$

Similarly, it can be derived that

$$\sigma_{rz}^I = C_{55}^I \frac{a^2 - R^2}{a^2} \frac{r}{\frac{1}{2}(R^2 - a^2) - R^2 \ln \frac{R}{a}} \left[u_z^I \Big|_{r=R} - u_z^I \Big|_{r=a} \right] \quad (4.16)$$

$$u_z^I = \frac{C_{55}^I}{C_{55}^I} \frac{a^2 - R^2}{a^2} \frac{\frac{1}{2} r^2}{\frac{1}{2}(R^2 - a^2) - R^2 \ln \frac{R}{a}} \left[u_z^I \Big|_{r=R} - u_z^I \Big|_{r=a} \right] \quad (4.17)$$

The radial displacements in the two phases can be assumed as [39]

$$u_r^I = b_1(z)r, \quad u_r^II = b_2(z)r + b_3(z)/r \quad (4.18)$$

According to Eq. (4.6c), we have

$$b_3 = (b_1 - b_2)a^2 \quad (4.19)$$

Perfect bonding assumption implies that $\varepsilon_{zz}^I \Big|_{r=a} = \varepsilon_{zz}^II \Big|_{r=a} = \varepsilon_{\text{int}}$, also note that $\varepsilon_{zz}^II \Big|_{r=R} = \varepsilon_0$. Substituting Eq.

(4.15), (4.17-4.19) into (4.2), we have

$$\begin{aligned} \varepsilon_{zz}^I &= \frac{C_{55}^II}{C_{55}^I} \frac{a^2 - R^2}{a^2} \frac{\frac{1}{2} r^2}{\frac{1}{2}(R^2 - a^2) - R^2 \ln \frac{R}{a}} [\varepsilon_0 - \varepsilon_{\text{int}}] \\ \varepsilon_{zz}^II &= \varepsilon_{\text{int}} + \frac{\frac{1}{2}(r^2 - a^2) - R^2 \ln \frac{r}{a}}{\frac{1}{2}(R^2 - a^2) - R^2 \ln \frac{R}{a}} [\varepsilon_0 - \varepsilon_{\text{int}}] \\ \varepsilon_{\theta\theta}^I &= \frac{u_r^I}{r} = b_1, \quad \varepsilon_{rr}^I = \frac{\partial u_r^I}{\partial r} = b_1 \\ \varepsilon_{\theta\theta}^II &= \frac{u_r^II}{r} = b_2 + \frac{(b_1 - b_2)a^2}{r^2}, \quad \varepsilon_{rr}^II = \frac{\partial u_r^II}{\partial r} = b_2 - \frac{(b_1 - b_2)a^2}{r^2} \end{aligned} \quad (4.20 \text{ a-d})$$

Using Eq. (4.20) in Eq. (4.3) then gives

$$\begin{aligned} \sigma_{zz}^II &= C_{11}^II \varepsilon_{zz}^II + C_{12}^II \varepsilon_{\theta\theta}^II + C_{13}^II \varepsilon_{rr}^II \\ &= C_{11}^II \left\{ \varepsilon_{\text{int}} + \frac{\frac{1}{2}(r^2 - a^2) - R^2 \ln \frac{r}{a}}{\frac{1}{2}(R^2 - a^2) - R^2 \ln \frac{R}{a}} [\varepsilon_0 - \varepsilon_{\text{int}}] \right\} + C_{12}^II \left\{ b_2 + \frac{(b_1 - b_2)a^2}{r^2} \right\} + C_{13}^II \left\{ b_2 - \frac{(b_1 - b_2)a^2}{r^2} \right\} \end{aligned}$$

$$\begin{aligned}
\sigma_{rr}'' &= C_{13}'' \varepsilon_{zz}'' + C_{23}'' \varepsilon_{\theta\theta}'' + C_{33}'' \varepsilon_{rr}'' \\
&= C_{13}'' \left\{ \varepsilon_{\text{int}} + \frac{\frac{1}{2}(r^2 - a^2) - R^2 \ln \frac{r}{a}}{\frac{1}{2}(R^2 - a^2) - R^2 \ln \frac{R}{a}} [\varepsilon_0 - \varepsilon_{\text{int}}] \right\} + C_{23}'' \left\{ b_2 + \frac{(b_1 - b_2)a^2}{r^2} \right\} + C_{33}'' \left\{ b_2 - \frac{(b_1 - b_2)a^2}{r^2} \right\} \\
\sigma_{rr}' &= C_{13}' \varepsilon_{zz}' + C_{23}' \varepsilon_{\theta\theta}' + C_{33}' \varepsilon_{rr}' = C_{13}' \varepsilon_{zz}' + C_{23}' b_1 + C_{33}' b_1
\end{aligned} \tag{4.21 a-c}$$

Considering the boundary conditions (Eq. (4.5)) and the continuity conditions (Eq. (4.6)), it can be obtained that

$$\sigma_{rr}'' \Big|_{r=R} = C_{13}'' \varepsilon_0 + C_{23}'' \left\{ b_2 + \frac{(b_1 - b_2)a^2}{R^2} \right\} + C_{33}'' \left\{ b_2 - \frac{(b_1 - b_2)a^2}{R^2} \right\} = 0 \tag{4.22}$$

$$C_{13}' \varepsilon_{\text{int}} + C_{23}' b_1 + C_{33}' b_1 = C_{13}'' \varepsilon_{\text{int}} + C_{23}'' b_1 + C_{33}'' (2b_2 - b_1) \tag{4.23}$$

From Eq. (4.20a), we have

$$\frac{C_{55}''}{C_{55}'} \frac{a^2 - R^2}{(R^2 - a^2) - 2R^2 \ln \frac{R}{a}} [\varepsilon_0 - \varepsilon_{\text{int}}] = \varepsilon_{\text{int}} \tag{4.24}$$

Substituting Eq. (4.21a) and (4.4a) into Eq. (4.7) leads to

$$\begin{aligned}
&\left(\frac{C_{11}'' \left(-\frac{1}{2}R^4 + \frac{1}{2}a^4 + 2a^2 R^2 \ln \frac{R}{a} \right)}{R^2 - a^2 - 2R^2 \ln \frac{R}{a}} \right) \varepsilon_{\text{int}} + \left(\frac{C_{11}'' \left(\frac{3}{2}R^4 + \frac{1}{2}a^4 - 2a^2 R^2 - 2R^4 \ln \frac{R}{a} \right)}{R^2 - a^2 - 2R^2 \ln \frac{R}{a}} \right) \varepsilon_0 \\
&+ \left[2a^2 (C_{12}'' - C_{13}'') \ln \frac{R}{a} \right] b_1 + \left[C_{12}'' \left(R^2 - a^2 - 2a^2 \ln \frac{R}{a} \right) + C_{13}'' \left(R^2 - a^2 + 2a^2 \ln \frac{R}{a} \right) \right] b_2 = (R^2 - a^2) \sigma - a^2 \langle \sigma_{zz}' \rangle
\end{aligned} \tag{4.25}$$

Combining Eq. (4.22-4.25), the following equations for solving ε_0 , ε_{int} , b_1 and b_2 are obtained,

$$\begin{bmatrix} M_{11} & M_{12} & M_{13} & M_{14} \\ M_{21} & M_{22} & M_{23} & M_{24} \\ M_{31} & M_{32} & M_{33} & M_{34} \\ M_{41} & M_{42} & M_{43} & M_{44} \end{bmatrix} \begin{bmatrix} \varepsilon_0 \\ \varepsilon_{\text{int}} \\ b_1 \\ b_2 \end{bmatrix} = \begin{bmatrix} 0 \\ 0 \\ 0 \\ (R^2 - a^2) \sigma - a^2 \langle \sigma_{zz}' \rangle \end{bmatrix} \tag{4.26}$$

where,

$$\begin{aligned}
M_{11} &= C_{13}'' , M_{12} = 0 , M_{13} = (C_{23}'' - C_{33}'') \frac{a^2}{R^2} , M_{14} = \left[C_{23}'' \left(1 - \frac{a^2}{R^2} \right) + C_{33}'' \left(1 + \frac{a^2}{R^2} \right) \right] , \\
M_{21} &= 0 , M_{22} = C_{13}' - C_{13}'' , M_{23} = C_{23}' + C_{33}' - C_{23}'' + C_{33}'' , M_{24} = -2C_{33}'' , \\
M_{31} &= 1 , M_{32} = \frac{(C_{55}' - C_{55}'')(R^2 - a^2) - 2C_{55}'R^2 \ln \frac{R}{a}}{C_{55}''(R^2 - a^2)} , M_{33} = 0 , M_{34} = 0 , \\
M_{41} &= C_{11}'' \frac{\frac{3}{2}R^4 + \frac{1}{2}a^4 - 2a^2R^2 - 2R^4 \ln \frac{R}{a}}{R^2 - a^2 - 2R^2 \ln \frac{R}{a}} , M_{42} = C_{11}'' \frac{-\frac{1}{2}R^4 + \frac{1}{2}a^4 + 2a^2R^2 \ln \frac{R}{a}}{R^2 - a^2 - 2R^2 \ln \frac{R}{a}} , \\
M_{43} &= 2a^2 (C_{12}'' - C_{13}'') \ln \frac{R}{a} , M_{44} = C_{12}'' \left(R^2 - a^2 - 2a^2 \ln \frac{R}{a} \right) + C_{13}'' \left(R^2 - a^2 + 2a^2 \ln \frac{R}{a} \right) \quad (4.27)
\end{aligned}$$

Then the solutions of Eq. (4.26) can be expressed as

$$\begin{aligned}
\varepsilon_{\text{int}} &= M_0 \left[(R^2 - a^2) \sigma - a^2 \langle \sigma_{zz}' \rangle \right] , \quad \varepsilon_0 = -M_{32} M_0 \left[(R^2 - a^2) \sigma - a^2 \langle \sigma_{zz}' \rangle \right] \\
b_1 &= \frac{M_{11} M_{24} M_{32} + M_{14} M_{22}}{M_{13} M_{24} - M_{14} M_{23}} M_0 \left[(R^2 - a^2) \sigma - a^2 \langle \sigma_{zz}' \rangle \right] \\
b_2 &= \frac{M_{11} M_{23} M_{32} + M_{13} M_{22}}{M_{14} M_{23} - M_{13} M_{24}} M_0 \left[(R^2 - a^2) \sigma - a^2 \langle \sigma_{zz}' \rangle \right] \quad (4.28a-d)
\end{aligned}$$

where

$$M_0 = \frac{M_{13} M_{24} - M_{14} M_{23}}{(M_{13} M_{24} - M_{14} M_{23})(-M_{32} M_{41} + M_{42}) + M_{43} (M_{11} M_{24} M_{32} + M_{14} M_{22}) - M_{44} (M_{11} M_{23} M_{32} + M_{13} M_{22})}$$

From Eq. (4.8a), (4.13) and (4.28), it leads to

$$\frac{d^2 \langle \sigma_{zz}' \rangle}{dz^2} - \alpha^2 \langle \sigma_{zz}' \rangle = -\frac{R^2 - a^2}{a^2} \alpha^2 \sigma \quad (4.29)$$

$$\text{where } \alpha^2 = C_{55}'' \frac{2(R^2 - a^2)(M_{32} + 1)M_0}{\frac{1}{2}(R^2 - a^2) - R^2 \ln \frac{R}{a}}$$

The general solution of Eq. (4.29) is given by

$$\langle \sigma_{zz}^I \rangle = c_1 e^{\alpha z} + c_2 e^{-\alpha z} + \frac{R^2 - a^2}{a^2} \sigma$$

in which c_1 and c_2 are constants. According to the boundary condition Eq. (4.5a), it yields the average axial normal stress in Phase I ($\langle \sigma_{zz}^I \rangle$) as

$$\langle \sigma_{zz}^I \rangle = \frac{(R^2 - a^2) \sigma}{a^2} \left(\frac{e^{-\alpha L} - 1}{e^{\alpha L} - e^{-\alpha L}} e^{\alpha z} - \frac{e^{\alpha L} - 1}{e^{\alpha L} - e^{-\alpha L}} e^{-\alpha z} + 1 \right) \quad (4.30)$$

Finally, the use of Eq. (4.30) in Eq. (4.8a), (4.20a,b) and (4.28a-d) derives the tensile strain along z-direction (ε_{zz}^I), interfacial shear stress (τ_{int}) as

$$\varepsilon_{zz}^I = \frac{C_{55}^{\text{II}}}{C_{55}^{\text{I}}} \frac{(R^2 - a^2)^2}{a^2} (M_{32} + 1) M_0 \sigma_0 \frac{\frac{1}{2} r^2}{\frac{1}{2} (R^2 - a^2) - R^2 \ln \frac{R}{a}} \left[\frac{e^{\alpha L} - 1}{e^{\alpha L} - e^{-\alpha L}} e^{-\alpha z} - \frac{e^{-\alpha L} - 1}{e^{\alpha L} - e^{-\alpha L}} e^{\alpha z} \right] \quad (4.31)$$

$$\varepsilon_{zz}^{\text{II}} = M_0 (R^2 - a^2) \sigma_0 \left[1 - \frac{\frac{1}{2} (r^2 - a^2) - R^2 \ln \frac{r}{a}}{\frac{1}{2} (R^2 - a^2) - R^2 \ln \frac{R}{a}} (M_{32} + 1) \right] \left[\frac{e^{\alpha L} - 1}{e^{\alpha L} - e^{-\alpha L}} e^{-\alpha z} - \frac{e^{-\alpha L} - 1}{e^{\alpha L} - e^{-\alpha L}} e^{\alpha z} \right] \quad (4.32)$$

$$\tau_{\text{int}}(z) = \frac{(a^2 - R^2) \alpha \sigma_0}{2a} \left(\frac{e^{-\alpha L} - 1}{e^{\alpha L} - e^{-\alpha L}} e^{\alpha z} + \frac{e^{\alpha L} - 1}{e^{\alpha L} - e^{-\alpha L}} e^{-\alpha z} \right) \quad (4.33)$$

The Mori-Tanaka (MT) model [40] was used to estimate the effective elastic properties of the B₄C nanowire reinforced composite in Phase II. Unless otherwise mentioned, the overall stiffness values of the composite in Phase I and II are given by

$$\begin{aligned} \mathbf{C}^{\text{I}} &= \mathbf{C}^{\text{BC}} \\ \mathbf{C}^{\text{II}} &= \mathbf{C}^{\text{m}} + \nu_{\text{BC}} (\mathbf{C}^{\text{BC}} - \mathbf{C}^{\text{m}}) \mathbf{T} (\nu_{\text{m}} \mathbf{I} + \nu_{\text{BC}} \mathbf{T})^{-1} \end{aligned} \quad (4.34 \text{ a,b})$$

in which

$$\mathbf{T} = \left[\mathbf{I} + \mathbf{S} (\mathbf{C}^{\text{m}})^{-1} (\mathbf{C}^{\text{BC}} - \mathbf{C}^{\text{m}}) \right]^{-1}$$

In Eq. (4.34), \mathbf{C}^{m} and \mathbf{C}^{BC} are the stiffness tensor of the epoxy matrix and B₄C nanowires, respectively;

\mathbf{I} is an identity matrix; v_m and v_{BC} represent the volume fractions of the epoxy matrix and B₄C nanowires in Phase II, respectively; \mathbf{S} is the Eshelby tensor, and the elements were obtained from ref. [41]. According to the experimental results, the isotropic elastic coefficients of the epoxy matrix, C_{ij}^m , are given by $C_{11}^m = 2.96$ GPa and $C_{12}^m = 1.46$ GPa. The elastic coefficients of boron carbide, C_{ij}^{BC} , were obtained from ref. [17] and [37] as follows, $C_{11}^{BC} = C_{22}^{BC} = 542.8$ GPa, $C_{12}^{BC} = 130.6$ GPa, $C_{13}^{BC} = C_{23}^{BC} = 63.5$ GPa, $C_{33}^{BC} = 534.5$ GPa, $C_{44}^{BC} = C_{55}^{BC} = 164.8$ GPa, $C_{66}^{BC} = (C_{11}^{BC} - C_{12}^{BC})/2$. Based on the experimental characterization, the following parameters were adopted to inform the analytical models: $a = 3$ μm , $R = 8$ μm , $L = 6$ μm , and $\sigma_o = 90$ MPa.

To better understand the reinforcing mechanisms of B₄C micro-/nano-fillers, the strain distributions of the RVE along the tensile direction (ε_{zz}) were calculated for three cases: (1) Phase I and Phase II are both pure epoxy (Fig. 4.11(a)); (2) Phase I is boron carbide and Phase II is pure epoxy (Fig. 4.11(b)); (3) Phase I is boron carbide and Phase II is B₄C nanowire reinforced epoxy composite ($v_{BC} = 50\%$, Fig. 4.11(c)). Consistent with the DIC deformation fields obtained from the *in-situ* SEM tensile testing, the RVE of the pure epoxy exhibits relatively uniform strain distribution, whereas the RVEs of the case (3) presents localized strain islands. As revealed by Fig. 4.11(b), the significant differences in stiffness between matrix and fillers lead to a sudden drop in the strain at the interface susceptible to the formation of voids and cracks. One effective approach to mitigating this problem is to design the micro/nano hybrid fillers. It is observed in case (3) that Phase II, reinforced by B₄C nanowires, serves as an intermediate layer, enabling strain gradually decreasing from the matrix to the filler (Fig. 4.11(c)).

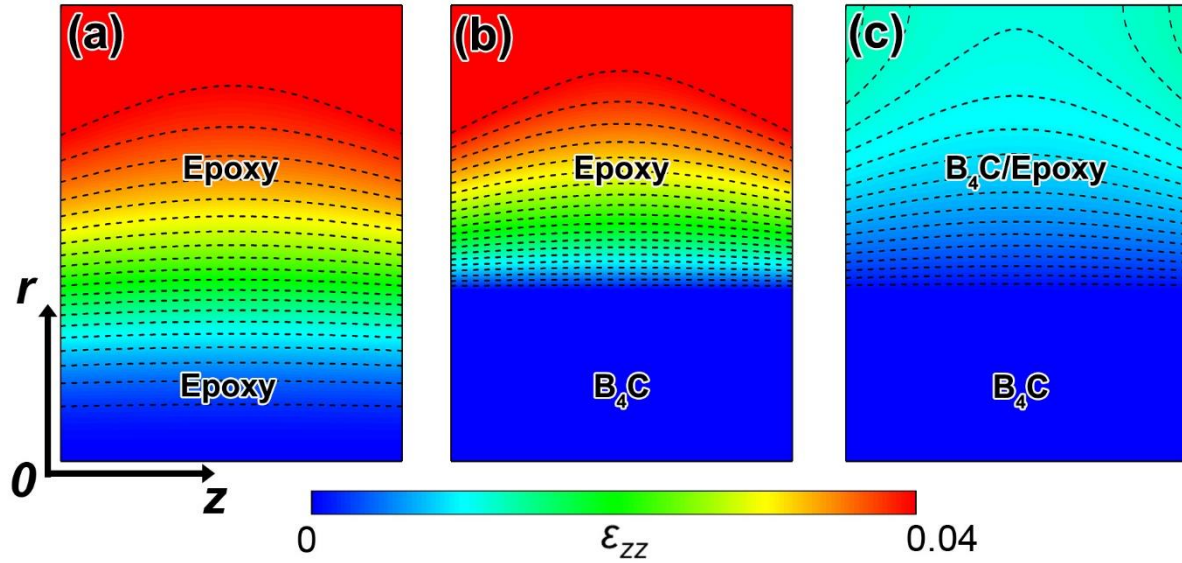


Fig. 4.11. Theoretically calculated normal strain distributions of the RVE for three cases: (a) pure epoxy, (b) Phase I is B_4C and Phase II is pure epoxy, and (c) Phase I is B_4C and Phase II is B_4C nanowire reinforced epoxy composite. Half of the strain distributions of the RVE is displayed, due to the symmetry.

Furthermore, the interfacial shear stress (τ_{int}) and average axial normal stress ($\langle \sigma_{zz}^I \rangle$) were calculated and normalized (Fig. 4.12) to investigate load transfer efficiency in the B_4C micro-/nano-filler reinforced composites. Due to symmetry, the middle of the RVE is shear stress-free, and the maximum stress transfer occurs near both ends (Fig. 4.12(a)). Dedicated by the global equilibrium requirement, the maximum axial stress is achieved in the middle of the RVE, whereas the minimum axial stress occurs at the ends (Fig. 4.12(b)). The magnitudes of both interfacial shear stress and average axial normal stress increase as the volume fraction of B_4C nanowires in Phase II (v_{BC}) increases initially and decrease afterward. Therefore, adding B_4C nanowires to Phase II, that is the design of B_4C micro-/nano-fillers, facilitates the load applied on the matrix being efficiently transferred into the fillers and then carried by the fillers.

As an index for evaluating the effectiveness of the reinforcing fillers embedded in the matrix, the

effective length of the B₄C fillers is introduced as [43]

$$L_{eff} = \frac{\int_0^L \langle \sigma_{zz}^I \rangle dz}{\langle \sigma_{zz}^I \rangle_{max}} \quad (4.35)$$

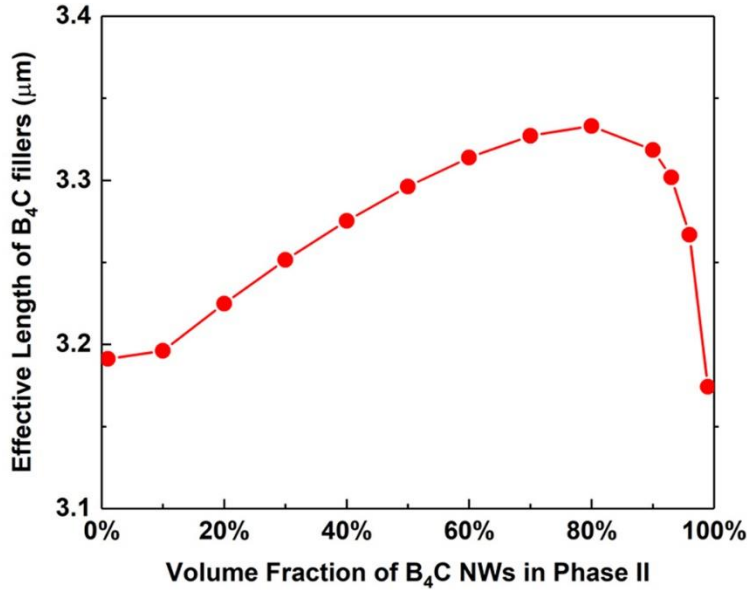


Fig. 4.13. The effective length of B₄C fillers associated with different volume fractions of B₄C nanowires in Phase II.

where $\langle \sigma_{zz}^I \rangle_{max}$ is the maximum value of the average axial normal stress along the length direction of the RVE. The results of the effective length associated with various volume fractions of the B₄C nanowires in Phase II are presented in Fig. 4.13. It is obvious that the multiscale design of B₄C fillers makes the effective length larger, which indicates higher load carrying efficiency of the reinforcements, and, accordingly, better overall mechanical performance of the composites [43]. Furthermore, the effective length can reach its peak by adjusting the volume fractions of the B₄C nanowires.

4.5 Conclusion

Assisted with cotton, we synthesized a new type of micro-/nano-filler which has B₄C microplatelet

as the core and radially aligned B₄C nanowires as the shell. Such B₄C micro-/nano-fillers enabled multiple multiscale reinforcing effects in the epoxy matrix, and largely enhanced the load carrying efficiency of the reinforcements, leading to the overall improved mechanical performance of the composites. In addition, the radially aligned B₄C nanowires on the B₄C microplatelets acted as interlocks between the wires and matrix, further pushing up the strength and toughness of the composites. To enhance the bonding between the B₄C fillers and epoxy, the B₄C micro-/nano-fillers were coated with a layer of PANI. With a low concentration of the PANI functionalized B₄C micro-/nano-fillers (1 wt.%), this B₄C/epoxy composite exhibited an exceptional combination of mechanical properties in terms of elastic modulus (~ 3.47 GPa), toughness (2026.3 kJ/m³), and fracture strain ($>3.6\%$). Importantly, we provide a new technique to design lightweight yet strong and tough materials that have enormous potentials in a multitude of fields including biomaterials, infrastructure and armors.

Reference

- [1] Munch, E. *et al.* Tough, Bio-inspired hybrid materials. *Science* **322**, 1516–1520 (2008).
- [2] Wegst, U. G. K., Bai, H., Saiz, E., Tomsia, A. P. & Ritchie, R. O. Bioinspired structural materials. *Nat. Mater.* **14**, 23–36 (2015).
- [3] Launey, M. E. & Ritchie, R. O. On the fracture toughness of advanced materials. *Adv. Mater.* **21**, 2103–2110 (2009).
- [4] Espinosa, H. D. *et al.* Tablet-level origin of toughening in abalone shells and translation to synthetic composite materials. *Nat. Commun.* **2**, 173–179 (2011).
- [5] Naleway, S. E., Porter, M. M., McKittrick, J. & Meyers, M. A. Structural design elements in biological materials: Application to bioinspiration. *Adv. Mater.* **27**, 5455–5476 (2015).
- [6] Lazzari, R., Vast, N., Besson, J. M., Baroni, S. & Dal Corso, A. Atomic structure and vibrational properties of icosahedral B₄C boron carbide. *Phys. Rev. Lett.* **83**, 3230–3233 (1999).
- [7] Zhou, M. J., Wong, S. F., Ong, C. W. & Li, Q. Microstructure and mechanical properties of B₄C films deposited by ion beam sputtering. *Thin Solid Films* **516**, 336–339 (2007).
- [8] Gu, Y., Chen, L., Qian, Y., Zhang, W. & Ma, J. Synthesis of nanocrystalline boron carbide via a solvothermal reduction of CCl₄ in the presence of amorphous boron powder. *J. Am. Ceram. Soc.* **88**, 225–227 (2005).
- [9] Ma, R. & Bando, Y. High purity single crystalline boron carbide nanowires. *Chem. Phys. Lett.* **364**, 314–317 (2002).
- [10] Tao, X. *et al.* B₄C-nanowires/carbon-microfiber hybrid structures and composites from cotton T-shirts. *Adv. Mater.* **22**, 2055–2059 (2010).
- [11] Xu, F. F. & Bando, Y. Formation of two-dimensional nanomaterials of boron carbides. *J. Phys. Chem. B* **108**, 7651–7655 (2004).

- [12] Zhang, D., McIlroy, D. N., Geng, Y. & Norton, M. G. Growth and characterization of boron carbide nanowires. *J. Mater. Sci. Lett.* **18**, 349–351 (1999).
- [13] Johnsson, M. Synthesis of boride, carbide, and carbonitride whiskers. *Solid State Ionics* **172**, 365–368 (2004).
- [14] Gu, H. *et al.* Polyaniline stabilized magnetite nanoparticle reinforced epoxy nanocomposites. *ACS Appl. Mater. Interfaces* **4**, 5613–5624 (2012).
- [15] Gu, H. *et al.* Magnetoresistive polyaniline-magnetite nanocomposites with negative dielectrical properties. *Polymer* **53**, 801–809 (2012).
- [16] Rappé, A. K., Casewit, C. J., Colwell, K. S., Goddard, W. A. & Skiff, W. M. UFF, a Full Periodic Table Force Field for Molecular Mechanics and Molecular Dynamics Simulations. *J. Am. Chem. Soc.* **114**, 10024–10035 (1992).
- [17] Wagner, R. S. & Ellis, W. C. Vapor-liquid-solid mechanism of single crystal growth. *Appl. Phys. Lett.* **4**, 89–90 (1964).
- [18] Hong, N., Langell, M. A., Liu, J., Kizilkaya, O. & Adenwalla, S. Ni doping of semiconducting boron carbide. *J. Appl. Phys.* **107**, (2010).
- [19] Thévenot, F. Boron carbide—A comprehensive review. *J. Eur. Ceram. Soc.* **6**, 205–225 (1990).
- [20] Domnich, V., Reynaud, S., Haber, R. A. & Chhowalla, M. Boron carbide: structure, properties, and stability under stress. *J. Am. Ceram. Soc.* **94**, 3605–3628 (2011).
- [21] Duncan, T. M. The Distribution of Carbon in Boron Carbide: A ^{13}C nuclear magnetic resonance study. *J. Am. Chem. Soc.* **106**, 2270–2275 (1984).
- [22] Tallant, D. R., Aselage, T. L., Campbell, A. N. & Emin, D. Boron carbide structure by Raman spectroscopy. *Phys. Rev. B* **40**, 5649–5656 (1989).

- [23] Yao, P., Xu, J., Wang, Y. & Zhu, C. Preparation and characterization of soluble and DBSA doped polyaniline grafted multi-walled carbon nanotubes nano-composite. *J. Mater. Sci. Mater. Electron.* **20**, 891–898 (2009).
- [24] Yang, W. *et al.* Synthesis of hollow polyaniline nano-capsules and their supercapacitor application. *J. Power Sources* **272**, 915–921 (2014).
- [25] Wang, Y., Wu, J. & Wei, F. A treatment method to give separated multi-walled carbon nanotubes with high purity, high crystallization and a large aspect ratio. *Carbon* **41**, 2939–2948 (2003).
- [26] Gu, H. *et al.* Epoxy resin nanosuspensions and reinforced nanocomposites from polyaniline stabilized multi-walled carbon nanotubes. *J. Mater. Chem. C* **1**, 729–743 (2013).
- [27] Mathur, R. B., Singh, B. P. & Pande, S. *Carbon nanomaterials: synthesis, structure, properties and applications*. CRC Press (2016).
- [28] Cox, H. L. The elasticity and strength of paper and other fibrous materials. *Br. J. Appl. Phys.* **3**, 72 (1952).
- [29] Nairn, J. A. A variational mechanics analysis of the stresses around breaks in embedded fibers. *Mech. Mater.* **13**, 131–154 (1992).
- [30] Gong, L. *et al.* Interfacial stress transfer in a graphene monolayer nanocomposite. *Adv. Mater.* **22**, 2694–2697 (2010).
- [31] Hsieh, T. H. *et al.* The toughness of epoxy polymers and fibre composites modified with rubber microparticles and silica nanoparticles. *J. Mater. Sci.* **45**, 1193–1210 (2010).
- [32] Marston, T. U., Atkins, A. G. & Felbeck, D. K. Interfacial fracture energy and the toughness of composites. *J. Mater. Sci.* **9**, 447–455 (1974).
- [33] Dassios, K. G. A review of the pull-out mechanism in the fracture of brittle-matrix fibre-reinforced composites. *Adv. Compos. Lett.* **16**, 17–24 (2007).

- [34] Sutton, M. A., Yan, J. H., Tiwari, V., Schreier, H. W. & Orteu, J. J. The effect of out-of-plane motion on 2D and 3D digital image correlation measurements. *Opt. Lasers Eng.* **46**, 746–757 (2008).
- [35] Gao, H., Ji, B., Jager, I. L., Arzt, E. & Fratzl, P. Materials become insensitive to flaws at nanoscale: lessons from nature. *Proc. Natl. Acad. Sci. U. S. A.* **100**, 5597–5600 (2003).
- [36] Wei, X., Naraghi, M. & Espinosa, H. D. Optimal length scales emerging from shear load transfer in natural materials: Application to carbon-based nanocomposite design. *ACS Nano* **6**, 2333–2344 (2012).
- [37] Timoshenko, S.; Goodier, J. N. *Theory of Elasticity; McGraw-Hill* (2001).
- [38] Nairn, J. A. On the use of shear-lag methods for analysis of stress transfer in unidirectional composites. *Mech. Mater.* **26**, 63–80 (1997).
- [39] Seidel, G. D. & Lagoudas, D. C. Micromechanical analysis of the effective elastic properties of carbon nanotube reinforced composites. *Mech. Mater.* **38**, 884–907 (2006).
- [40] Benveniste, Y. A new approach to the application of Mori-Tanaka's theory in composite materials. *Mech. Mater.* **6**, 147–157 (1987).
- [41] Qiu, Y. P. & Weng, G. J. On the application of Mori-Tanaka's theory involving transversely isotropic spheroidal inclusions. *Int. J. Eng. Sci.* **28**, 1121–1137 (1990).
- [42] McClellan, K. J., Chu, F., Roper, J. M. & Shindo, I. Room temperature single crystal elastic constants of boron carbide. *J. Mater. Sci.* **36**, 3403–3407 (2001).
- [43] Tsai, J. L. & Lu, T. C. Investigating the load transfer efficiency in carbon nanotubes reinforced nanocomposites. *Compos. Struct.* **90**, 172–179 (2009).

Chapter 5 Boron carbide nanoskeleton enabled, flexible lithium-sulfur batteries

5.1 Introduction

Developing advanced energy-storage systems becomes paramount due to the continuously increasing demand of energy consumptions and rising concerns about environmental issues.[1-4] Owing to the stern reality that conventional lithium-ion batteries (LIBs) are approaching their theoretical limit,[5-9] lithium-sulfur (Li-S) battery is considered as one of the most promising energy storage devices for electric vehicles, portable electronics, and even grid-scale storage devices.[10] Li-S chemistry offers superior theoretical specific capacity (1673 mAh/g) while natural abundance sulfur endows low cost and environmental compatibility.[11] Coupling with lithium metal, the assembled Li-S battery has a specific energy of 2600 W h/kg, which is more than five times higher than that of state-of-the-art lithium-ion batteries.[12] Despite the obvious advantages of Li-S batteries, many challenges need to be addressed before practical implementation, by and large, due to severe capacity decay, poor cycle life, low utilization of sulfur, and bad coulombic efficiency.[13] This dilemma can be primarily ascribed to the low electrical conductivities of sulfur, dissolution of intermediate polysulfides (Li_xS_n , $3 \leq n \leq 8$), and structural collapse induced by large volume variation (~80%) during solid-solid conversion between sulfur and Li_2S . [14,15]

Aforementioned issues have sparked considerable interests in the configuration and rational design of Li-S battery cathodes to increase the sulfur utilization, immobilize polysulfides, and enhance battery's structural stability. Advanced carbon materials, such as porous carbon, carbon nanotube and graphene, [16,17] have been extensively studied and widely utilized in various devices, such as supercapacitors,

[18] solar cells, [19, 20] piezoresistive sensors, [21] and strain sensors. [22] To date, the most common cathode design is to impregnate sulfur into various carbon matrices, such as amorphous carbon,[23] carbon nanotube,[24] and graphene.[25-27] Although substantial progress has been made, carbon-based materials alone are insufficient for high-performance Li-S batteries, especially the ones assembled in the flexible/wearable electronic devices, because it is still very challengeable to simultaneously increase the sulfur content, inhibit the “shuttle effect”, and ensure mechanical stability of the electrode.[28-30]

To address these issues, many efforts and improvements have been made to encapsulate sulfur with novel materials to mitigate capacity decay and enhance cycling performance, especially by employing carbides due to their chemical and mechanical stabilities.[31,32] Boron carbide (B_4C), one of the third hardest materials known in nature,[33] is distinguished from other materials by its eminent physical and mechanical properties such as low density (2.5 g/cm^3), high melting point (exceeding $2400 \text{ }^\circ\text{C}$), extreme hardness ($27.4 - 37.7 \text{ GPa}$), high elastic modulus (460 GPa), outstanding corrosion resistance, and high thermal stability.[34] In addition, at the nanometer scale, B_4C nanowires are ductile, without cracking when being bent to an included angle of 70° .[35] Such exceptional properties make B_4C a promising electrode material for batteries and fuel cells.[36-41] However, to the best of our knowledge, the investigation on B_4C as the electrode material for Li-S batteries is rare, let alone its further design and production.

Here, we report a rational design and implementation of a flexible, free-standing cathode for Li-S batteries with B_4C nanowires (BC-NWs) as the skeleton. In specific, porous activated cotton textile (ACT) was applied as the framework, and BC-NWs@ACT composite was obtained by *in-situ* synthesizing the

self-assembled high-density BC-NWs on the ACT via a conventional vapor-liquid-solid (VLS) [42] process. Then the preparation of a binder-free cathode for Li-S batteries was realized by impregnating elemental melted sulfur into the as-synthesized BC-NWs@ACT composite to form BC-NWs@ACT/S, and in further wrapping the BC-NWs@ACT/S with reduced graphene oxide (rGO) sheets that serve as the self-adaptive protective shell. This novel hierarchically configured cathode (BC-NWs@ACT/S/rGO) successfully confined sulfur in the three-dimensional interconnected framework while being flexible and mechanically robust. Ultimately, the Li-S cell with BC-NWs@ACT/S/rGO as the cathode exhibited excellent cycling stability (over 1000 cycles), an ultralow capacity decay rate (0.056% per cycle) and high capacities at a range of discharging rate from 0.1 to 1.5 mA/cm². The flexible free-standing BC-NWs@ACT/S/rGO cathode was also assembled into a lightweight and foldable Li-S battery, which retained a high specific capacity and excellent mechanical stability, confirming its practical usage as a flexible power source.

5.2 Synthesis and characterization of the electrode nanocomposite

5.2.1 Experimental methods

The BC-NWs@ACT hybrid structure was directly synthesized according to our previously established method.[43,44] A Ni-B emulsion was mixed by dissolving 7 g of Ni(NO₃)₂·6H₂O and 4 g of amorphous boron powders into 10 ml of ethanol under ultrasonic vibration. A piece of cotton textile was immersed in the Ni-B emulsion and dried at 70 °C in a preheated oven for 3 h. The BC-NWs@ACT hybrid structure was synthesized in a horizontal alumina tube furnace (diameter: 60 mm, length: 790 mm). The nickel- and boron-loaded cotton textile was placed in the middle of the tube furnace and heated

to 1160 °C for 2 h with 300 sccm (standard cubic centimeter) continuous flow of argon at atmospheric pressure. BC- NWs@ACT/S nanocomposite was prepared via a melt-diffusion method. Sulfur powders were loaded onto the as-synthesized BC-NWs@ACT plate and heated to 156 °C for 10 h in a sealed autoclave.

In a typical procedure, graphene oxide (GO) solution with a concentration of ~4 mg/ml was produced using a modified hummers method [45] from pure graphite powders. A piece of BC-NWs@ACT/S nanocomposite was dipped in the GO solution and dried for 6 h at 70 °C. The obtained hybrid structure was further thermally treated at 200 °C for 2 h in a sealed autoclave to vaporize any superfluous sulfur and partially reduce the GO to conductive rGO. BC-NWs@ACT/rGO hybrid structure with the same size was produced following the above-mentioned process as a reference to calculate the loading of sulfur. The sulfur loading of the BC-NWs@ACT/S/rGO hybrid cathode was measured to be ~3.0 mg/cm². As shown in Fig. 5.1, the mass ratio of active S was calculated to be 77.6 wt % using thermogravimetric analysis (TGA; Q50, TA Instruments). A piece of ACT was synthesized by directly

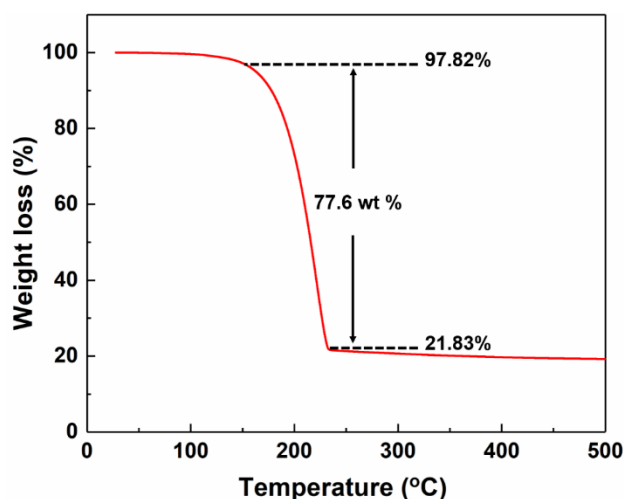


Fig. 5.1. Thermogravimetric analysis (TGA) spectrum of the BC-NWs@ACT/S/rGO composite.

heating the blank cotton textile to 1160 °C with 300 sccm continuous flow of argon in the tube furnace. Sulfur powders were respectively loaded onto the ACT and the BC-NWs@ACT plates without rGO coating, and heated to 156 °C for 10 h and 200 °C for 2 h. The as-synthesized ACT/S and BC-NWs@ACT/S hybrid cathodes served as control samples and the mass of loading sulfur was controlled to be $\sim 3.0 \text{ mg/cm}^2$.

The morphology and compositions of the as-synthesized samples were characterized and analyzed by scanning electron microscopy (SEM, Quanta 650), high-resolution transmission electron microscopy (HRTEM, FEI Titan 80), energy dispersive x-ray spectroscopy (EDX on the SEM and HRTEM), x-ray diffraction (XRD, PANalytical X'Pert Pro MPD), X-ray photoelectron spectroscopy (XPS, ULVAC-PHI, Inc.), and Raman spectroscopy (Raman, Renishaw InVia Raman microscope at 514 nm). The specific surface area of the composite was measured using a Quantachrom Autosorb iQ nitrogen adsorption-

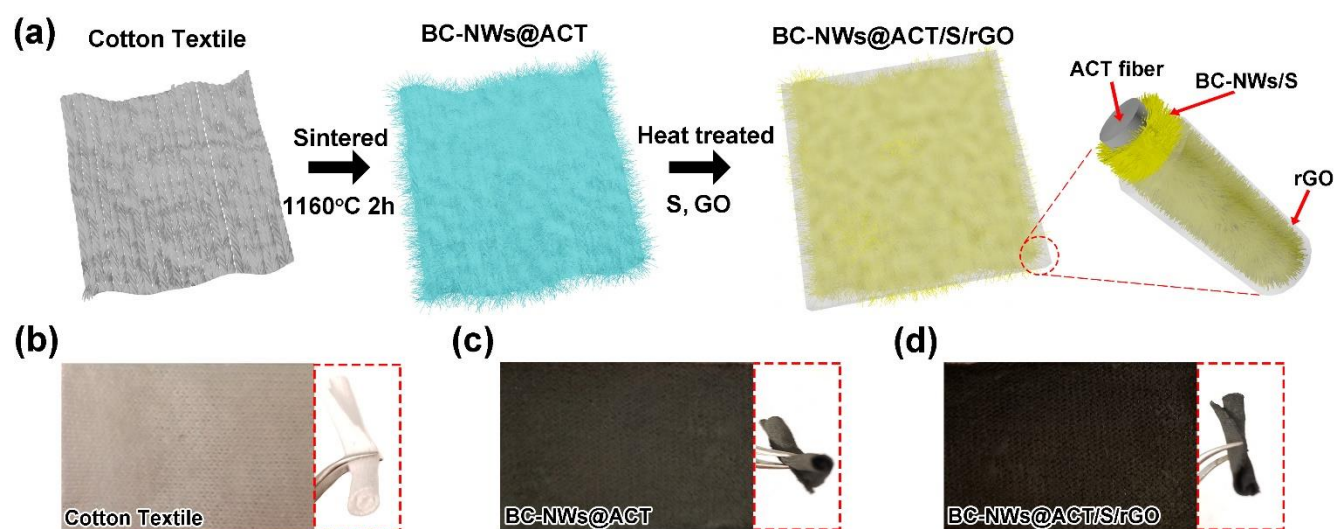


Fig. 5.2. (a) Schematic illustration of the design principle and synthesis process of BC-NWs@ACT/S/rGO hybrid structure. (b,c,d) Digital images of cotton textile, BC-NWs@ACT and BC-NWs@ACT/S/rGO samples. The corresponding samples under folded state are also imaged, as shown in the inset.

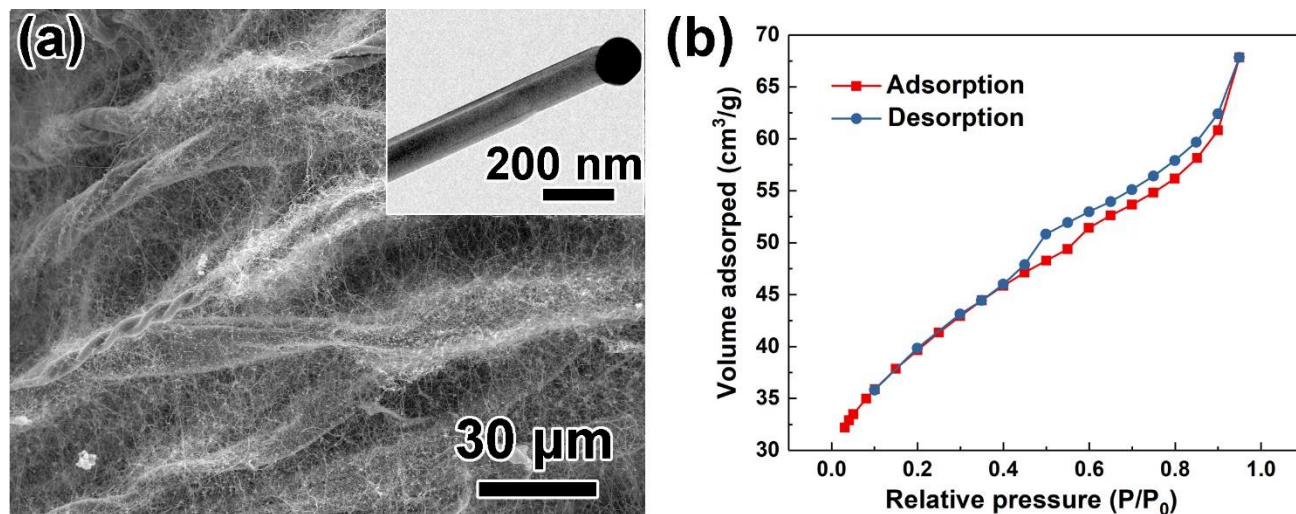


Fig. 5.3. Synthesis and characterization of BC-NWs@ACT composite. (a) Low-magnification SEM image of BC-NWs@ACT and TEM image inset of a B₄C nanowire. (b) Nitrogen adsorption/desorption isothermal curves of the BC-NWs@ACT composite.

desorption analyzer and measured with the Brunauer–Emmet–Teller (BET) theory.

5.2.2 Results and discussion

A one-step synthesis (Fig. 5.2) was used to obtain BC-NWs@ACT hybrid structure via VLS method by utilizing amorphous boron powder as boron source, carbonaceous gases generated from pyrolysis of cotton as carbon source and nickel as the catalyst. Scanning electron microscopy (SEM) and transmission electron microscopy (TEM) images (Fig. 5.3 (a)) demonstrate that high-density boron carbide nanowires with catalytic particles on their tips are uniformly aligned on ACT microfibers. Each 1 μm×1 μm region contains around 20 nanowires, which have dimensions with diameters in the range of 50-500 nm and the average length of 5 μm. X-ray diffraction (XRD) analysis verifies that the nanowires are rhombohedral boron carbide (JCPDS No. 6-0555) with nickel boride in the catalyst particles (Fig. 5.5 (a)). Typical peak broadening and shifting are due to the existence of nickel and small particle

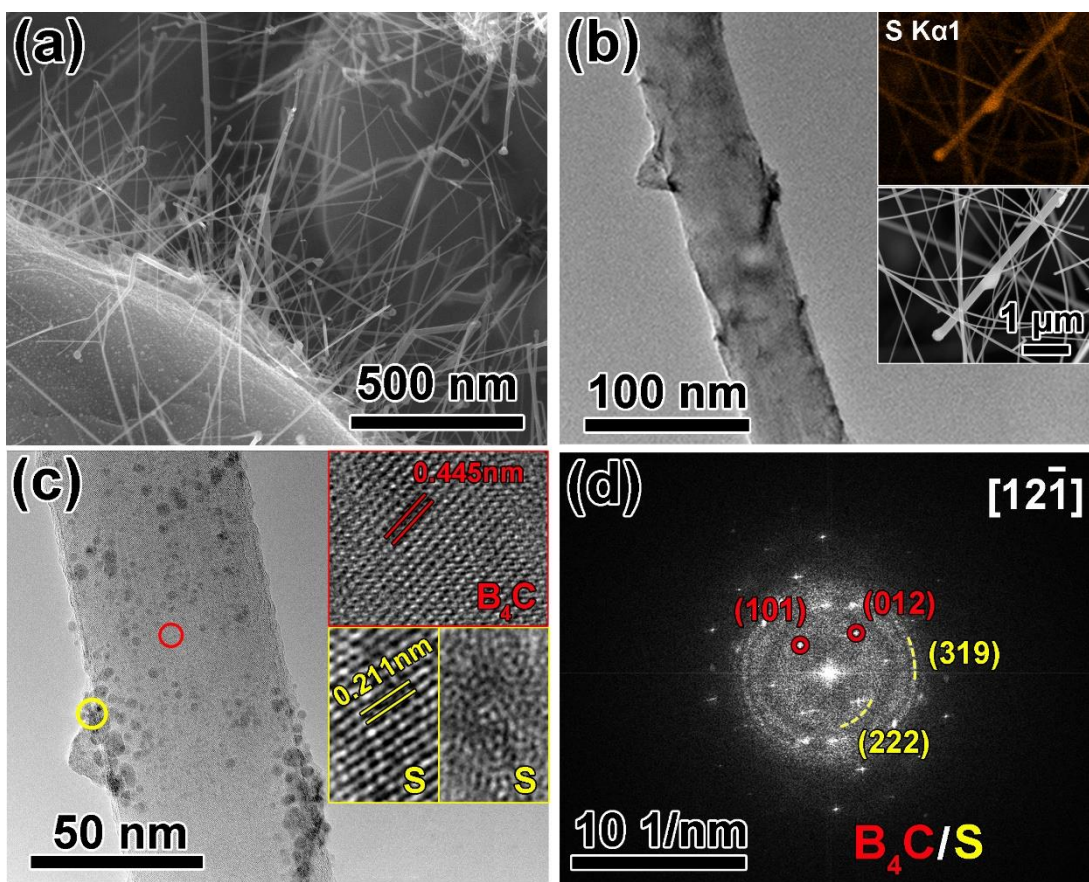


Fig. 5.4. Synthesis and characterization of BC-NWs@ACT/S composite. (a) Low-magnification SEM image of BC-NWs@ACT/S. (b) TEM image of BC-NW/S (EDS sulfur map and corresponding SEM image of BC-NWs/S in the inset). (c) HRTEM image and close-up observations of B₄C and sulfur, and (d) the corresponding FFT of BC-NW/S.

sizes.[46] The nitrogen adsorption/desorption test showed that such BC-NWs@ACT composite had a BET surface area of ~142.6 m²/g (Fig. 5.3 (b)).

Afterward, sulfur was deposited via a simple melt-diffusion method at 156 °C to construct the BC-NWs@ACT/S nanocomposite. Fig. 5.4 (a) and (b) show the SEM image of BC-NWs@ACT/S and the TEM image of an individual B₄C nanowire coated with sulfur. No obvious morphology changes are observed after heating but the surface of the nanowire becomes “rougher” due to the uniform deposition

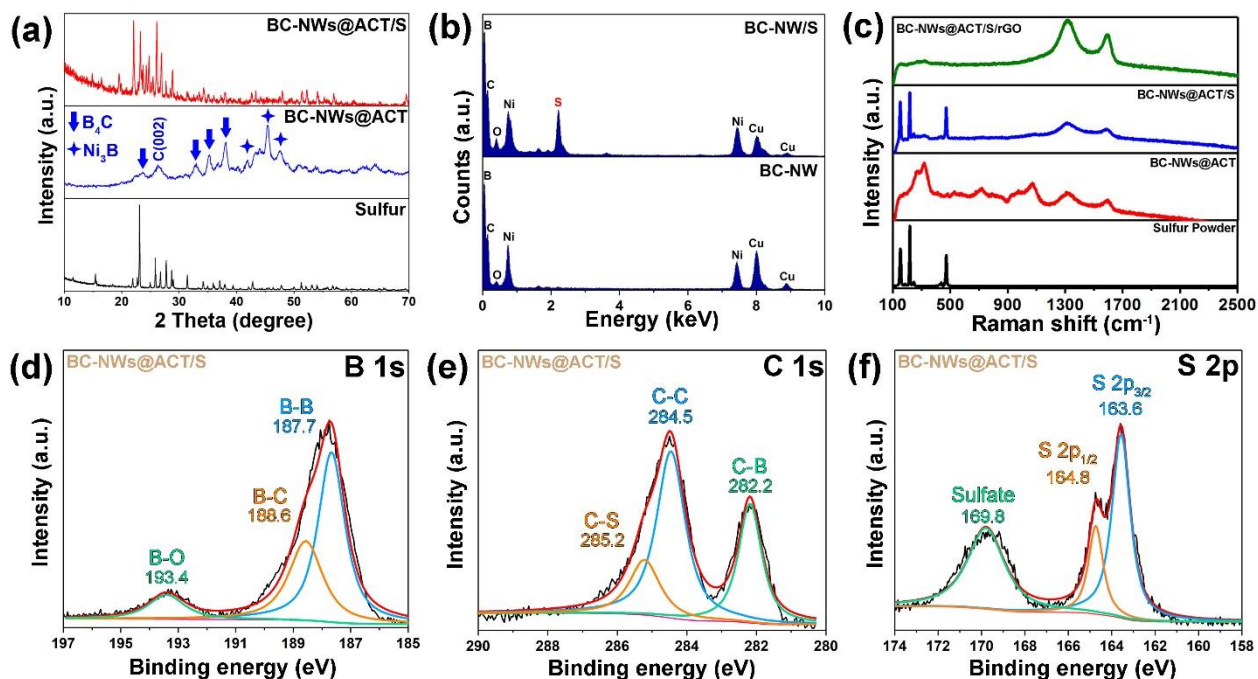


Fig. 5.5. Characterization of BC-NWs@ACT/S composite. (a) XRD patterns of sulfur powders, BC-NWs@ACT and BC-NWs@ACT/S. (b) EDX characterization of BC-NW and BC-NW/S. (c) Raman spectra of pure S powder, BC-NWs@ACT, BC-NWs@ACT/S, and BC-NWs@ACT/S/rGO. High-resolution (g) B 1s, (h) C 1s, and (i) S 2p XPS spectra of BC-NWs@ACT/S.

of sulfur, which is further verified by energy dispersive x-ray (EDX) spectrum (Fig. 5.5 (b)) and sulfur elemental mapping (the insets of Fig. 5.4 (b)). The primary structural unit cell of B₄C exhibited a rhombohedral arrangement consisting of 12-atom icosahedra and 3-atom linear chains ($R\bar{3}m$ space group, $a = 5.16\text{\AA}$, and $\alpha = 65.7^\circ$). [33] A close-up inspection (Fig. 5.4 (c)) and the corresponding Fast Fourier Transform (FFT) pattern with a zone axis $[12\bar{1}]$ (Fig. 5.4 (d)) indicate that the B₄C nanowires were grown with the perfect rhombohedral crystal lattice, and clearly demonstrate that sulfur particles were homogeneously anchored on the surface of nanowires. The measured crystal plane spacings of B₄C are consistent with the (101) and (012) reflections in the XRD patterns (Fig. 5.5 (a)).

The high-resolution TEM (HRTEM) images (the insets of Fig. 5.4 (c)) and the diffraction rings (broad and narrow) in Fig. 5.4 (d) jointly verify that sulfur existed in both polycrystalline and amorphous phases. The lattice fringe spacing of ~ 0.211 nm is uniquely indexed to the (319) crystal plane of sulfur in the orthorhombic structure, in good agreement with the XRD results in Fig. 5.5 (a) (JCPDS no. 08-0247). X-ray photoelectron spectroscopy (XPS) was performed to detect the elemental composition and the chemical bonding states of BC-NWs@ACT/S. In the B 1s spectra, three peaks centered at 187.7, 188.6, and 193.4 eV were observed, corresponding to B-B, B-C, and B-O bonds respectively (Fig. 5.5 (d)). The C 1s peaks revealed the existence of C-B (282.2 eV), C-C (284.5 eV), and C-S (285.2 eV) bonds (Fig. 5.5 (e)). [47] The S 2p spectrum was deconvoluted into three peaks centered at 163.6 eV (S 2p_{3/2}), 164.8 eV (S 2p_{1/2}), and 169.8 eV (Sulfate) (Fig. 5.5 (f)). The S 2p_{3/2} and S 2p_{1/2} peaks have an energy separation of 1.2 eV and intensity ratio of 2:1, confirming the successful loading of sulfur. [48]

With various functional groups on the surface (epoxy and hydroxyl groups), GO has been reported as a polysulfide immobilizer which can slow down the diffusion and prevent the parasitic reactions on electrodes. [49] Herein, to further mitigate the shuttle effect, the as-obtained BC-NWs@ACT/S nanocomposite was wrapped with partially reduced GO sheets. The SEM image of BC-NWs@ACT/S/rGO (Fig. 5.6 (a)) reveals that the ACT microfiber with radially growing B₄C nanowires as branches was wrapped by the silk-like rGO skin, and the individual nanowire was also uniformly covered by the compact self-assembled rGO sheets (Fig. 5.6 (b)). The enlarged HRTEM images (the insets of Fig. 5.6 (b)) and the corresponding FFT pattern (Fig. 5.6 (c)) present that B₄C nanowires remained well single crystal lattice structure after the heating treatment up at 200 °C and can retain

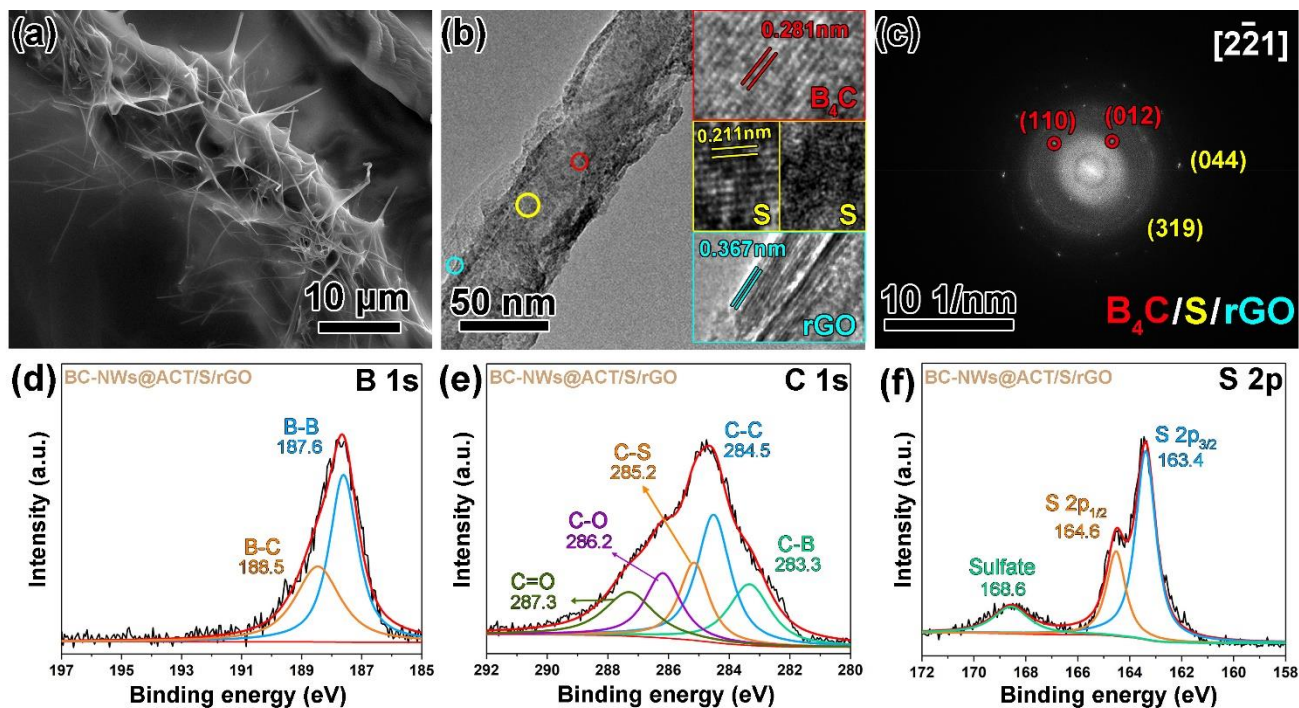


Fig. 5.6. Synthesis and characterization of BC-NWs@ACT/S/rGO composite. (a) SEM image of BC-NWs@ACT/S/rGO. (b) HRTEM image and close-up observations of B₄C, sulfur and rGO, and (c) the corresponding FFT of BC-NW/S/rGO. High-resolution (d) B 1s, (e) C 1s, and (f) S 2p XPS spectra of BC-NWs@ACT/S/rGO.

excellent mechanical properties. Raman spectrum was used to characterize the surface components (Fig. 5.5(c)) of BC-NWs@ACT/S/rGO electrode. For untreated BC-NWs@ACT samples, Raman peaks in the range of 200 to 600 cm⁻¹ are assigned to the vibrations of chain structures of B₄C, and the regions above 600 cm⁻¹ are associated with intraicosahedral and intericosahedral modes.[50] The sharp peaks in the Raman spectrum ranging from 100 to 500 cm⁻¹ appear in the BC-NWs@ACT/S sample and vanish in the BC-NWs@ACT/S/rGO sample, suggesting that sulfur is well dispersed and confined by rGO protective shell. The successful loading of sulfur was further confirmed by high-resolution S 2p XPS analysis of BC-NWs@ACT/S/rGO, showing the S 2p_{3/2} and S 2p_{1/2} peaks with energy separation of 1.2

eV and intensity ratio of 2:1 (Fig. 5.6(f)). In the B 1s spectra, the two dominant peaks centered at 187.6 and 188.5 eV were identified as B-B and B-C bonds, respectively (Fig. 5.6(d)). The C 1s spectrum was deconvoluted into five peaks at 283.3, 284.5, 285.2, 286.2, and 287.3 eV, which can be ascribed to C-B, C-C, C-S, C-O (hydroxyl and epoxy groups), and O=C-O (carboxyl groups) bonds, respectively (Fig. 5.6(e)). The results are consistent with the previous studies. [47,51] In sum, the BC-NWs@ACT scaffold was successfully fabricated, anchored by sulfur and enfolded by rGO skin, which acts as a natural barrier to polysulfide diffusion. The B₄C nanowires and rGO sheets jointly maximize the interfacial contacts between sulfur and the cathode where the electrochemical redox reaction occurs. Furthermore, the mechanically strong B₄C skeleton and rGO skin are expected to buffer the volume variations and thereby enhance the cyclic stability.

5.3 Battery assembly and electrochemical testing

5.3.1 Experimental methods

To characterize the electrochemical properties of the as-synthesized cathode, CR2032 type coin cells were assembled by using MTI MSK-110 crimping machine in an argon-filled glove box (Mbraun, Germany), with BC-NWs@ACT/S/rGO as a cathode, lithium metal as an anode and Celgard 2400 film as a separator, respectively. Specific capacity values and charge/discharge rates were calculated based on the mass of active materials (sulfur). The electrolyte solution was prepared by dissolving 1 M lithium bis(trifluoromethanesulfonyl)imid (LiTFSI) and 0.2 M LiNO₃ in 1,3-dioxolane (DIOX)/1,2-dimethoxyethane (DME) (1:1, by volume). For comparison, the ACT/S, ACT/S/rGO, and BC-NWs@ACT/S cathodes were also assembled into CR2032 type coin cells as the control samples. To

demonstrate the excellent mechanical properties and flexibility of BC-NWs@ACT/S/rGO, the flexible Li-S cell was assembled using the binder-free BC-NWs@ACT/S/rGO nanocomposite directly as the cathode. Galvanostatic charge/discharge measurements were performed at different rates in the voltage range of 1.3-3 V versus Li/Li⁺ using a LAND CT2003A battery tester. A CHI 660E electrochemical workstation was used to measure the cyclic voltammograms (CV) and electrochemical impedance spectroscopy (EIS) in the frequency ranging from 0.01 Hz to 100 kHz with an AC perturbation of 5mV.

5.3.2 Results and discussion

CR2032 type coin cells were fabricated using the BC-NWs@ACT/S/rGO nanocomposite (Fig. 5.7) as the freestanding cathode and Li foil as the anode for electrochemical performance evaluation. Bare ACT/S, ACT/S/rGO, and BC-NWs@ACT/S electrodes were also assembled in coin cells for comparison. The sulfur loading of the cathodes was measured to be ~3.0 mg/cm². Fig. 5.8 (a) shows the galvanostatic voltage profiles of the battery at the current density of 0.6 mA/cm² with a voltage window between 1.3

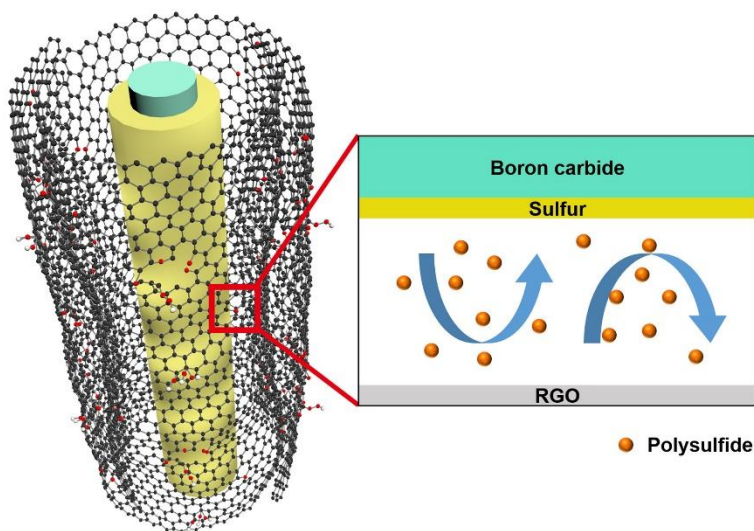


Fig. 5.7. Schematic illustration of a representative volume element of BC-NWs@ACT/S/rGO electrode.

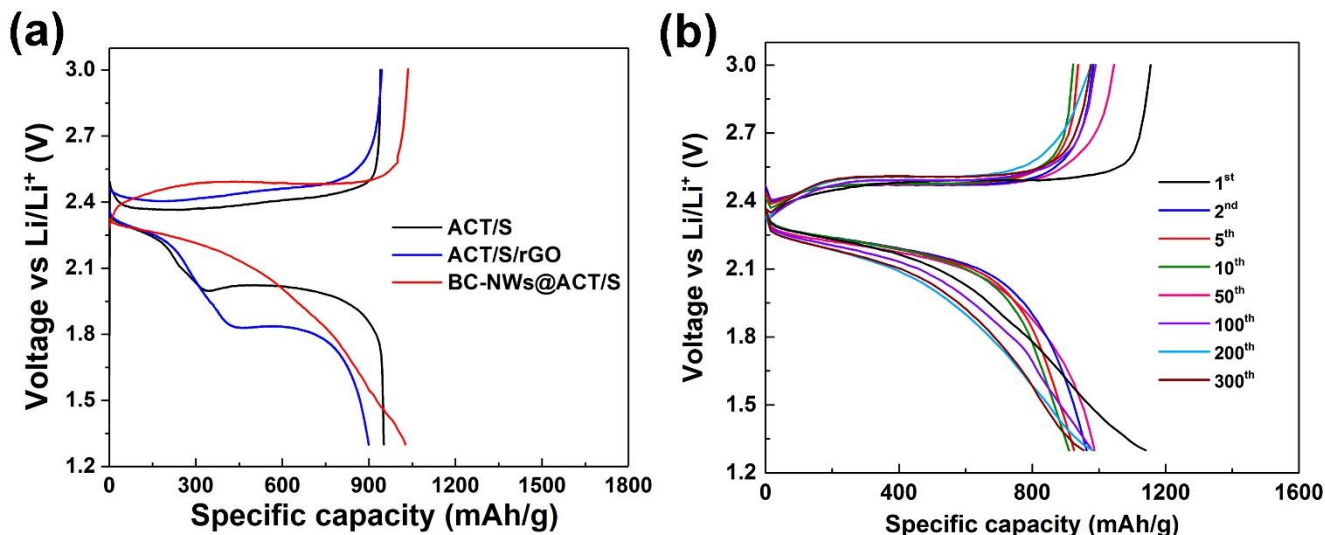


Fig. 5.8. Electrochemical characterization of composite electrodes. (a) Galvanostatic discharge/charge profiles of ACT/S, ACT/S/rGO, and BC-NWs@ACT/S. (b) Galvanostatic discharge/charge profiles of BC-NWs@ACT/S/rGO at the current density of 0.6 mA/cm².

and 3V. The profiles of ACT/S and ACT/S/rGO cells display a typical two-plateau discharging morphology which corresponds to the reduction of S₈ molecule to long-chain dissolved polysulfides (Li₂S_x, 4 ≤ x ≤ 8) and the subsequent formation of short-chain insoluble polysulfides (Li₂S₂, Li₂S), respectively.[14] Intriguingly, BC-NWs@ACT/S and BC-NWs@ACT/S/rGO electrodes (Fig. 5.8(b)) exhibited a sloping discharge plateau in the galvanostatic charge/discharge curves at the current density of 0.6 mA/cm². The cyclic voltammetry (CV) curves obtained at a sweep rate of 0.1 mV/s (Fig. 5.9 (a)) confirmed this finding. Theoretically, the Li-S battery features two cathodic peaks, corresponding to the transformations of S₈ to -S₄²⁻ and -S₄²⁻ to -S₂²⁻, respectively. Unexpectedly, the BC-NWs@ACT/S/rGO cell exhibited a single pair of redox peaks, with the oxidation peak at 2.68 V versus Li⁺/Li and the reduction peak at 2.18 V versus Li⁺/Li, indicating that the dissolution of polysulfides was disrupted by the existence of BC-NWs. During the first 300 cycles, the overall features of the charge/discharge curves

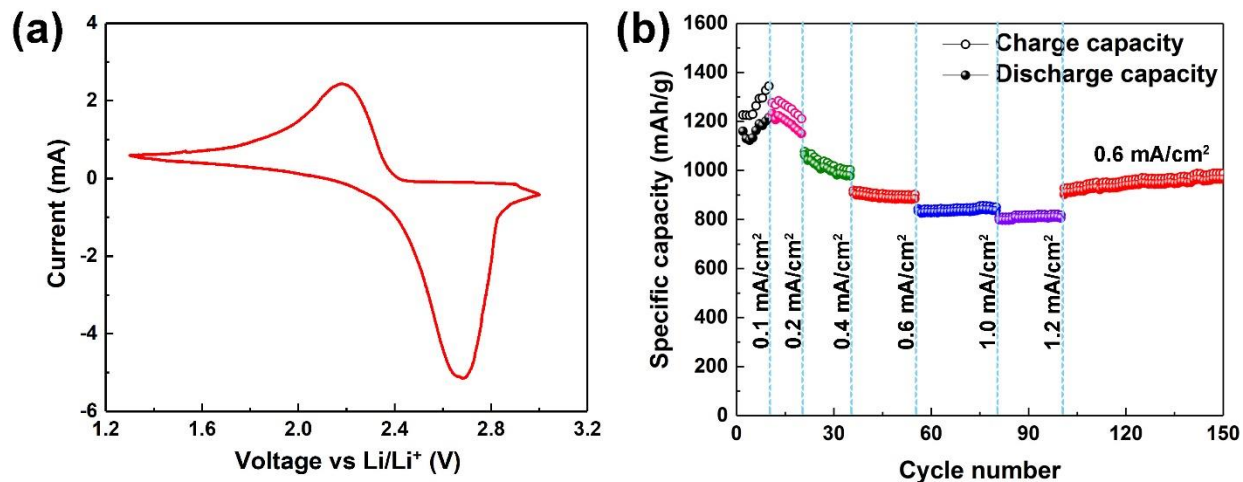


Fig. 5.9. Electrochemical characterization of BC-NWs@ACT/S/rGO composite electrode. (a) Initial cyclic voltammogram profiles at a scan rate of 0.1 mV/s. (b) Rate performance at different current densities.

show no obvious changes, implying good electrochemical stability of the BC-NWs@ACT/S/rGO cathode and highly reversible redox reactions. Comparing with other control samples (Fig. 5.10 (b)), the BC-NWs@ACT/S/rGO electrode showed almost negligible overcharging behavior in the first cycle, indicating that the polysulfide shuttle effect was significantly reduced. [52]

The rate capability of the BC-NWs@ACT/S/rGO composite is displayed in Fig. 5.9 (b). Theoretically, a lower capacity is often obtained at a higher rate due to polarization. Intriguingly, with increasing current rate from 0.1 to 1.2 mA/cm², the capacity of the BC-NWs@ACT/S/rGO cell initially increased and then gradually decreased afterward, because sulfur utilization gradually enhanced in this hybrid structured electrode. The reversible discharge capacities delivered by the battery are 1166, 1195, 1008, 890, 833 and 805 mAh/g at the current rates of 0.1, 0.2, 0.4, 0.6, 1.0 and 1.2 mA/cm², respectively. At the maximum charge/discharge rate (1.2 mA/cm²), the cycling process remained stable with a high specific capacity (~800 mAh/g). Impressively, when the current rate was reversed to 0.6 mA/cm², the

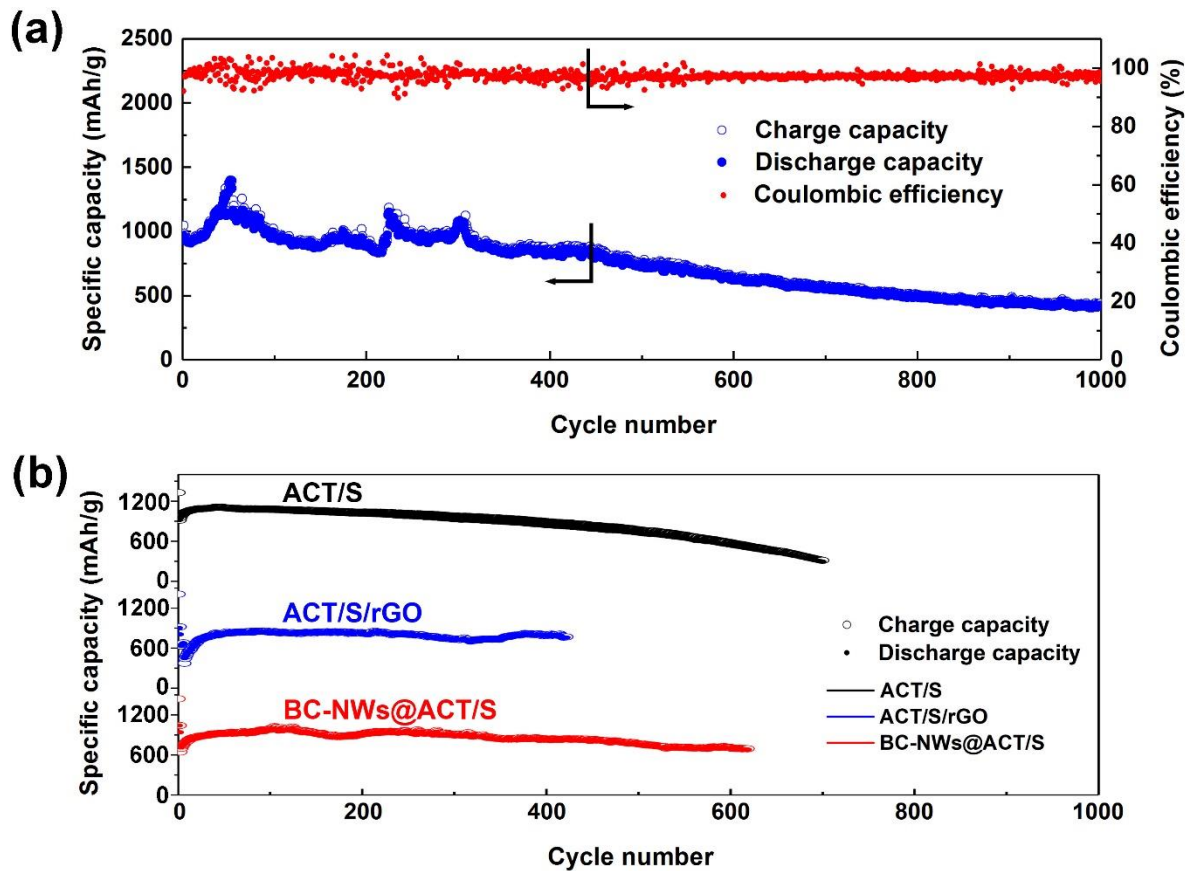


Fig. 5.10. Electrochemical characterization of composite electrodes. (a) Cycling performance and correlated coulombic efficiency of BC-NWs@ACT/S/rGO. (b) Cycling performance of ACT/S, ACT/S/rGO, and BC-NWs@ACT/S.

discharge capacity recovered and even increased continuously up to 965 mAh/g over 50 cycles, demonstrating an excellent rate capability. The long-term cycling test was carried out to further characterize the electrochemical properties of the BC-NWs@ACT/S/rGO electrode, which exhibited an outstanding cycling performance at a high current density of 1.5 mA/cm² for over 1000 charge/discharge cycles (Fig. 5.10 (a)). The initial discharge capacity is 963 mAh/g and the discharge capacity increased gradually up to 1395 mAh/g in the first 50 cycles due to the increasing utilization of sulfur in the 3D hybrid structural electrode. [53] A high specific capacity retention of 89.8% was achieved at the 400th

cycle and an ultralow capacity loss rate of 0.056% per cycle was obtained for 1000 cycles, revealing that the shuttle effect was significantly reduced via the spatial and chemical confinement enabled by the three-dimensional BC-NWs@ACT/S/rGO structure. Additionally, the cell presented a coulombic efficiency as high as 95.4% even after 1000 cycles, and the average coulombic efficiency was calculated to be 97.4%, illustrating superior sulfur utilization and cyclic stability of BC-NWs@ACT/S/rGO. For comparison, the cycling performances of ACT/S, ACT/S/rGO, and BC-NWs@ACT/S were also characterized (Fig. 5.10 (b)). The profile of ACT/S displayed an initial discharge capacity of 914 mAh/g, which is close to that of BC-NWs@ACT/S/rGO electrode due to the same sulfur loading. However, the capacity of ACT/S faded rapidly down to 292 mAh/g after 700 cycles with 0.1% capacity loss per cycle. The specific capacity retention of ACT/S/rGO and BC-NWs@ACT/S electrodes were calculated to be 91.2% and 90.1% at the 400th cycle, respectively, indicating the inhibitory effect of both BC-NWs and rGO on

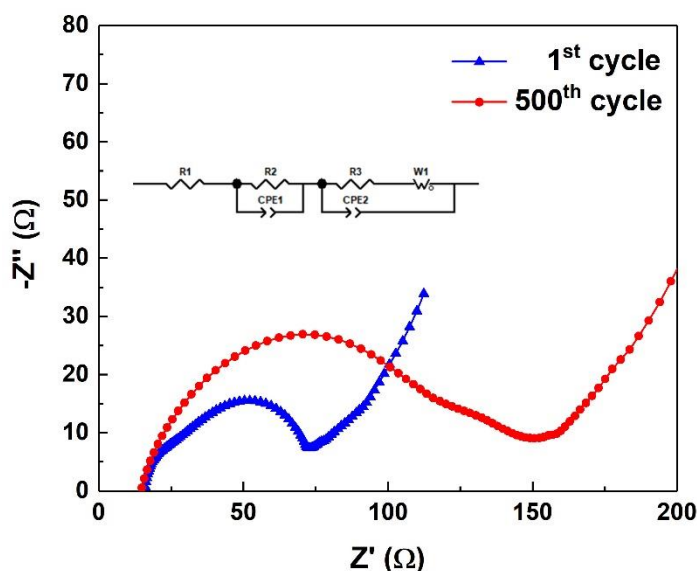


Fig. 5.11. Nyquist plots and the equivalent circuit of the BC-NWs@ACT/S/rGO cathode at the 1st and 500th cycles.

“shuttle effect”. The lifespan verified that hierarchically configured BC-NWs@ACT/S/rGO cathode can largely enhance the cycling stability. The electrochemical impedance spectra (EIS) of the BC-NWs@ACT/S/rGO cell at the 1st and 500th cycles are shown in Fig. 5.11. The Nyquist plots are composed of two depressed semicircles and a straight line. The semicircle in the high-frequency range corresponds to the formation of the passivation layer ($\text{Li}_2\text{S}_2/\text{Li}_2\text{S}$) on the surface of the lithium anode (R_2), and the semicircle in the middle-frequency range attributes to the Li^+ charge transfer (R_3). The straight line in the low-frequency region relates to the diffusion of lithium ions. Based on the equivalent circuit fitting, after cycling, R_2 increased, suggesting the formation of SEI film. Meanwhile, the slight increase of charge transfer resistance after 500 cycles indicated that the BC-NWs@ACT/S/rGO cathode was stable after long time cycling. Impressively, armed with the B_4C nanoskeleton and rGO skin, the BC-NWs@ACT/S/rGO cathode exhibited superior electrochemical performance - higher specific capacity, longer cycling life, and greater rate capability.

5.4 Role of BC-NWs and rGO in Li-S cell

5.4.1 Methods

To characterize the inhibition effect of B_4C on polysulfide dissolution and diffusion, the as-synthesized BC-NWs@ACT/S composite was used as the cathode and assembled in a Li-S battery cell. After the assembled batteries were charged/discharged for several cycles, we stopped the tests during the charging process, and the coin batteries were disassembled manually. The cathodes were taken out and soaked into 1,2-dimethoxyethane (DME) to remove residual electrolyte and part of polysulfides. The as-obtained cathodes were further washed with acetone and dilute water, and then dried at 70 °C for 10 h.

Visualized adsorption of polysulfide test was carried out using 1 mmol/L Li_2S_6 solution in DIOX/DME (1:1, by volume). Li_2S_6 was synthesized by mixing lithium and sulfur at a molar ratio of 1:3 in DIOX/DME

All molecular dynamics (MD) calculations were performed using the Large-scale Atomic/Molecular Massively Parallel Simulator (LAMMPS), [54] to describe the response of BC-NWs@ACT/S/rGO hybrid structure to volume expansion and verify that boron carbide has an inhibitory effect on “shuttle effect”. The initial atomic configurations (boron carbide unit cell, graphene, lithium polysulfide, electrolyte molecules, Fig. 5.12) were optimized using Cambridge Serial Total Energy Package

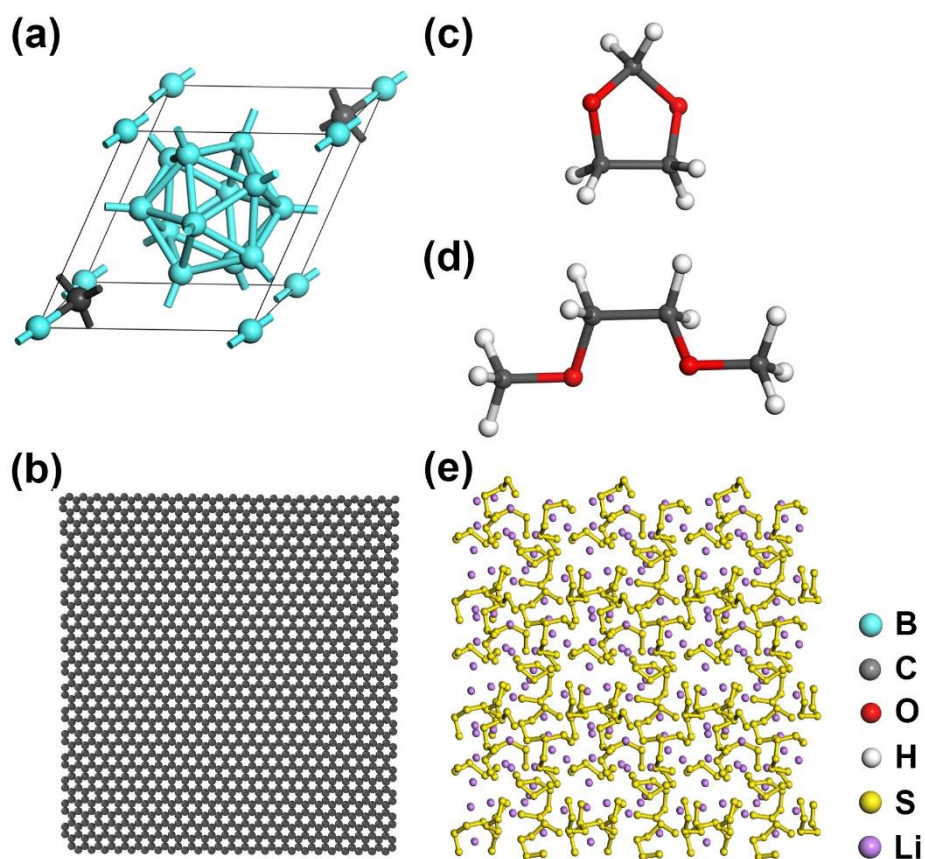


Fig. 5.12. Atomic structures used in MD simulations of (a) Boron carbide, (b) Graphene, (c) 1,3-dioxolane (DIOX), (d) 1,2- dimethoxyethane (DME) and (e) Lithium polysulfides.

(CASTEP) [55] based on density functional theory (DFT). The generalized gradient approximation (GGA-PBE) was selected to describe the exchange and correlation energy. The Broyden–Fletcher–Goldfarb–Shanno (BFGS) minimizer was used to perform cell optimization, and the convergence tolerance of total energy was set to be 1×10^{-6} eV/atom. The as-obtained configurations were replicated, truncated and combined to be the initial input structure for MD simulations. Periodic boundary conditions were applied in all directions. Boron carbide interactions were described by a set of Stillinger–Weber parameters.[56] The canonical ensemble (N, V, T) was applied to relax the structure with a time step of 0.25 fs, and the constant temperature was controlled by a Nose-Hoover thermostat method.

For the MD simulations of volume expansion, a cylindrical core-shell model was constructed with an inner diameter of 5 nm for B₄C core and an outer diameter of 10 nm for polysulfide nanoparticles. To be simplified, the cylindrical system was encapsulated by eight pieces of graphene sheet instead of rGO. Graphene was modeled by the adaptive intermolecular reactive empirical bond order (AIREBO) potential.[57] The non-bond interactions among B₄C, polysulfide nanoparticles and graphene were simply described by the Lennard–Jones (LJ) potential with parameters $\varepsilon = 1$ meV. Volume expansion and shrinkage processes were realized by varying parameter σ in LJ potential from 1 to 5 Å continuously.[25] Simulations temperature was set to be 1 K to ignore the thermal effect. For MD simulations of polysulfide dissolution and diffusion, the reactive force field simulation (ReaxFF),[58] with previously published Li/S ReaxFF parameter sets,[59] was implemented to describe the Li/S interatomic interactions. Solvent molecules (1:1 mixture of DME and DIOX) were modeled using CHARMM force field,[60] and the parameters are obtained from Ref. [61], [62] and [63]. The non-bond interactions were described by the

LJ and Coulomb potential, and LJ parameters were simply set to be $\epsilon = 1$ meV and $\sigma = 3$ Å, which are in the appropriate range for typical materials. After relaxed for 20000 MD steps, the atomic configurations were selected as the reference positions ($x(0)$, Fig. 5.13). The mean square displacement (MSD,

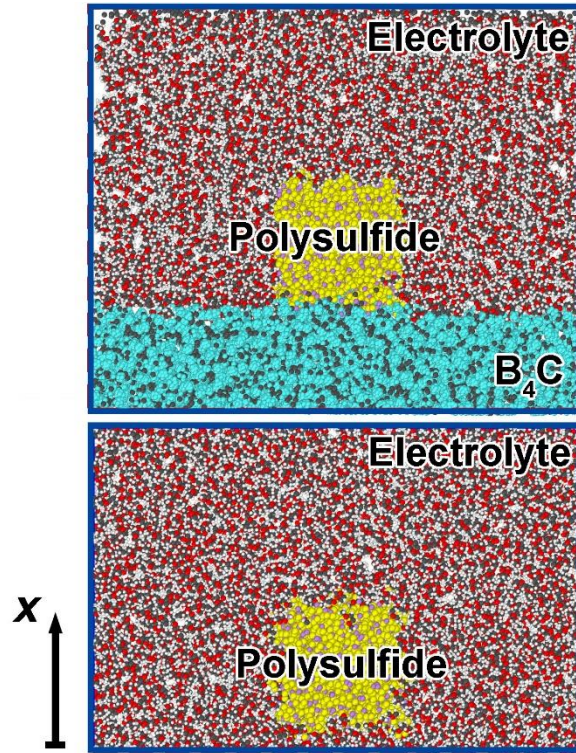


Fig. 5.13. MD models of polysulfide particle diffusion with and without B_4C .

$\langle [x(t) - x(0)]^2 \rangle$) of polysulfide particles was obtained as a function of time and the diffusion coefficient was calculated by linearly fitting the MSD-time curves.

5.4.2 Results and discussion

The immobilizing effect of rGO on sulfur and lithium polysulfides via the reactive functional groups has been extensively studied.[49] However, to the best of our knowledge, no previous studies have been reported on the inhibition effect of B_4C on polysulfide dissolution and diffusion. In this work, both

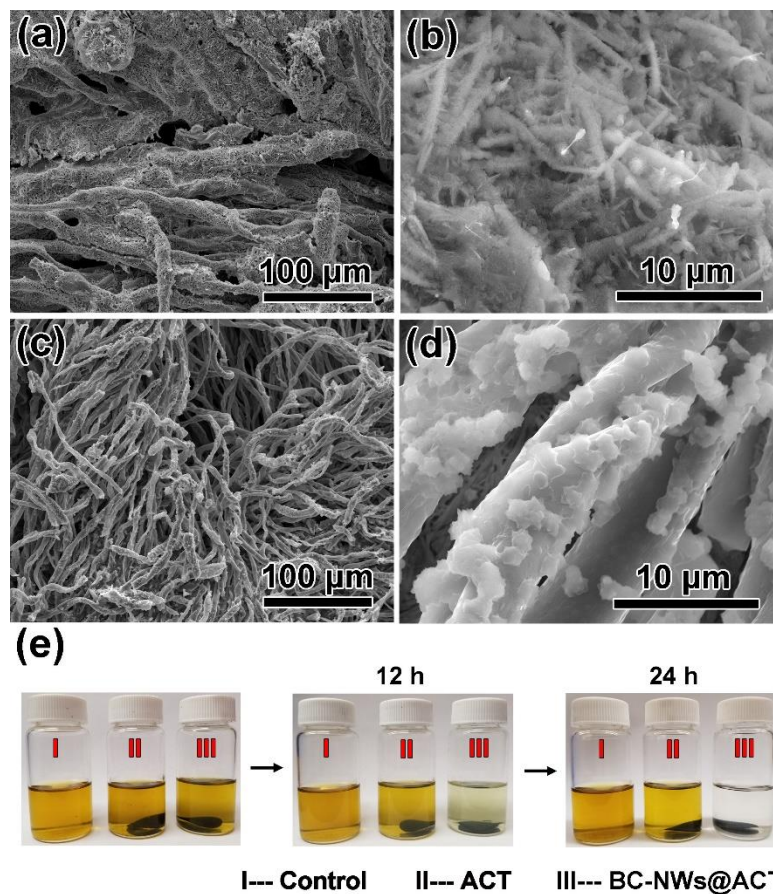


Fig. 5.14. SEM images of (a,b) BC-NWs@ACT/S and (c,d) ACT/S electrodes after cycling. (e) Photographs of Li₂S₆ polysulfide absorption test with ACT and BC-NWs@ACT.

experimental characterizations and molecular dynamics (MD) simulations were carried out to unveil the role of B₄C nanowires in Li-S batteries. To rule out the impact of rGO skin, sulfur powders were loaded onto the bare BC-NWs@ACT plate without coating rGO. The as-synthesized BC-NWs@ACT/S composite was then used as the cathode and assembled in a Li-S battery cell. After 10 cycles of charge/discharge, the cell was disassembled to characterize the morphological changes of the cycled cathode by SEM. The cycled BC-NWs@ACT/S and ACT/S (the control sample) cathodes were rinsed with 1,2- dimethoxyethane (DME), acetone and distilled water to compare the capacities of polysulfide

adsorption. At the same magnification, SEM inspections on the cycled BC NWs@ACT/S (Fig. 5.14 (a)) and ACT/S (Fig. 5.14 (c)) samples present that individual BC-NWs@ACT micro-fibers have an average diameter of 16.5 μm , which is much larger than the pristine ACT fibers (5.4 μm), indicating that large amounts of polysulfides are anchored on the BC-NWs@ACT/S cathode. Compared with the ACT/S sample (Fig. 5.14 (d)), the B₄C nanoskeleton in the BC-NWs@ACT/S cathode largely enhanced the surface area of the cathode, hindering the dissolution of polysulfides (Fig. 5.14 (b)). Static polysulfide absorption test (Fig. 5.14 (e)) was carried out to further evaluate the adsorption capability of B₄C, with the solution of 1 mmol/L Li₂S₆ in 1,3-dioxolane (DIOX)/1,2-dimethoxyethane (DME) (1:1, by volume). No obvious color change was observed for the Li₂S₆ solution with ACT, indicating a weak adsorption capability. Compared with ACT, the significant color fading (brown to colorless) of the Li₂S₆ solution with BC-NWs@ACT suggested the strong interactions between B₄C and polysulfides.

MD simulations were carried out to further uncover how B₄C nanowires affect the polysulfide diffusion process in the electrolyte (Fig. 5.12 and Fig. 5.13). The diffusion coefficient of polysulfide molecules, D_f , was calculated at room temperature through

$$D_f = \lim_{t \rightarrow \infty} \langle [x(t) - x(0)]^2 \rangle / 2t \quad (5.1)$$

where t is time, $\langle [x(t) - x(0)]^2 \rangle$ is the mean square displacement (MSD) of polysulfide molecules in direction x . The drift of the center of mass (COM) of polysulfides was subtracted out before MSD was calculated. At room temperature (300K), D_f of polysulfides in the electrolyte without B₄C was obtained as $1.87 \times 10^{-10} \text{ m}^2/\text{s}$, which is consistent with previous work; [64,65] while the B₄C nanoskeleton successfully reduced the diffusivity down to $1.06 \times 10^{-10} \text{ m}^2/\text{s}$, revealing that the B₄C nanowires can

effectively confine the polysulfide particles around the cathode, and largely limit the shuttle effect, in accord with the experimental results. In our model, the interaction between B_4C and polysulfides is only described by van der Waals forces (LJ potential, Coulombic interaction). In nanowire growth, amorphous carbon coating with functional groups could be generated, which could further absorb polysulfides via chemical bonding.

In addition to the shuttle effect, the large volume variation during the charge/discharge process is another factor that deteriorates the electrochemical performance of Li-S batteries. To simplify the system, for MD simulations graphene sheets were studied instead of rGO. The atomic configuration (Fig. 5.15) represents a cross-section of a typical representative volume element (RVE) of the BC-NWs/S/graphene cylindrical structure, based on which MD simulations were performed to investigate the self-adaptive behavior to the volume change of graphene skin during the discharge/charge process. The MD results

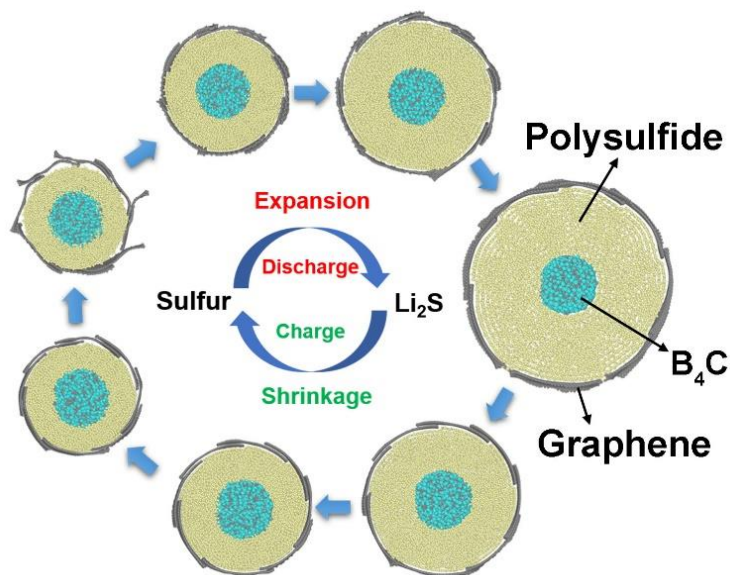


Fig. 5.15. MD snapshots of the atomic configurations representing a cross-section of the BC-NWs/S/graphene cylindrical structure in a cycle of charge/discharge process.

reveal that the B₄C core remains stable while the graphene shell accommodates a large volume change without destructing the structure. In a cycle of polysulfide expansion/contraction, the multilayer graphene unfolds and slides back and forth between layers while maintaining contact with the internal polysulfide structure, which can release strain energy induced by volume variations and enhance the charge transfer kinetics. In reality, the self-adaptive process of the BC-NWs@ACT/S/rGO electrode should be more complicated due to its complex hybrid structure. Therefore, the capacity changes, in the first 300 cycles, were induced by the gradual utilization of sulfur and the complex self-adaptive behavior of cathode (Fig. 5.10 (a)). After the self-optimization process, the BC-NWs@ACT/S/rGO cell became much stable, thus largely increasing its lifespan. Armed with an in-depth understanding of the experimental results and MD simulations, it is concluded that the synergistic effects of B₄C nanoskeleton and rGO skin largely enhance the electrode stability, thereby improving the electrochemical performance. This BC-NWs@ACT/S/rGO configuration demonstrates unprecedented opportunities for designing robust cathodes for Li-S batteries.

5.5 Flexible lithium-sulfur batteries with BC-NWs@ACT/S/rGO cathode

A flexible cell was assembled with the BC-NWs@ACT/S/rGO as a cathode, Celgard 2400 film as a separator and lithium foil as an anode. No external pressure was applied during the assembling process. Charge/discharge cycling tests (Fig. 5.16(a)) were carried out to characterize the electrochemical properties of the flexible BC-NWs@ACT/S/rGO electrode at normal (1st-25th cycles) and bent (25th-50th cycles) states. The flexible cell was cycled in the normal state from the beginning, and the capacity was found to be stabilized at ~500 mAh/g under the bent state, because in the bent state, external pressure was applied, thereby improving the solid-solid interfacial contact. Similarly, the flexible cell displays a

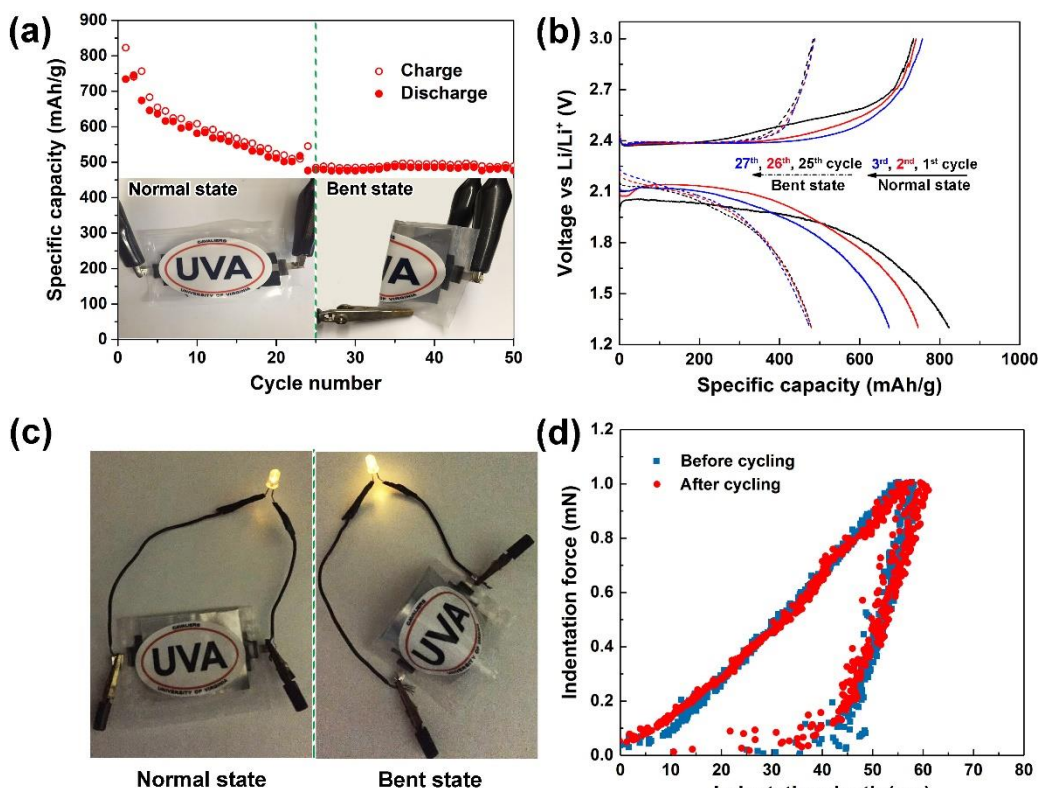


Fig. 5.16. Electrochemical performance and mechanical characterization of the flexible BC-NWs@ACT/S/rGO composite electrode. (a) Cyclic performance of the flexible battery cell under normal and bent states. (b) The charge/discharge voltage profiles under normal (1st, 2nd and 3rd cycles) and bent (25th, 26th, and 27th cycles) states. (c) The photograph of soft package Li-S cell lighting up a light-emitting diode (LED) in normal and bent states. (d) Nanoindentation load-displacement curves of BC-NWs before and after cycling.

sloping discharge plateau in the galvanostatic charge/discharge curves under normal (1st, 2nd and 3rd cycles) and bent (25th, 26th, and 27th cycles) states (Fig. 5.16(b)). The reproducible charge/discharge voltage profiles together with the negligible overcharging behavior in the initial cycle unveil that the flexible BC-NWs@ACT/S/rGO electrode possesses excellent mechanical robustness and electrochemical stability. A light-emitting diode (LED) was lightened up by the as-obtained soft package Li-S cell at flat and folded states (Fig. 5.16(c)), verifying the practicality of the flexible BC-NWs@ACT/S/rGO cathode. To characterize the mechanical properties and chemical stability of BC-

NWs, the flexible BC-NWs@ACT/S/rGO cathodes, before and after cycling, were treated by ultrasonication, to separate and disperse BC-NWs onto the silicon substrate. The nanoindentation force-displacement curves obtained from the BC-NWs before and after cycling are almost identical (Fig. 5.16(d)), demonstrating that battery cycling and complex chemical environment have little effect on the mechanical properties of BC-NWs. The reduced elastic moduli were measured to be 253 and 226 GPa before and after over 1000 cycles, respectively, based on the unloading curves according to the Oliver-Pharr method. [66] Convincingly, BC-NWs@ACT hybrid structure is a promising candidate in the flexible energy storage devices due to the flexibility of ACT, excellent mechanical properties and chemical stability of BC-NWs.

5.6 Conclusion

In summary, the flexible ACT cloth with boron carbide nanowires as the skeleton and reduced graphene oxide as the protective skin was successfully synthesized via low-cost raw materials and employed as a 3D conductive host for sulfur to construct high-performance flexible lithium-sulfur batteries. Compared with the ACT/S electrode, the as-fabricated Li-S battery using BC-NWs@ACT/S/rGO as the cathode demonstrated the combined advantages of ACT, B₄C nanowires and rGO, and yielded significant improvements, in terms of high specific capacity (the initial discharge capacity was 963 mAh/g and after 50 cycles increased to 1395 mAh/g at a high current density of 1.5 mA/cm²), superior cycling stability (over 1000 cycles), ultralow capacity decay rate (0.056% per cycle) and excellent rate capability (current density from 0.1 to 1.2 mA/cm²). The excellent electrochemical performance of BC-NWs@ACT/S/rGO cell was primarily attributed to the outstanding mechanical

properties of the B₄C skeleton, the self-adaptive capability to volume variations of rGO skin, and the synergistic effects of B₄C and rGO on the suppression of polysulfide diffusion. The flexible free-standing BC-NWs@ACT/S/rGO cathode was also assembled into a foldable Li-S cell, presenting a high specific capacity and excellent mechanical stability. Such novel B₄C nanowire enabled electrode system opens up unprecedented opportunities for designing flexible high-performance energy storage devices.

Reference

- [1] Armand, M. & Tarascon, J. M. Building better batteries. *Nature* **451**, 652–657 (2008).
- [2] Dunn, B., Kamath, H. & Tarascon, J.-M. Electrical energy storage for the grid: A battery of choices. *Science* **334**, 928–935 (2011).
- [3] Yan, L., Wang, H., Huang, D. & Luo, H. Electrodes with high conductivities for high performance lithium/sodium ion batteries. *Eng. Sci.* **1**, 4–20 (2018).
- [4] Li, R. *et al.* Advanced composites of complex Ti-based oxides as anode materials for lithium-ion batteries. *Adv. Compos. Hybrid Mater.* **1**, 440–459 (2018).
- [5] Goodenough, J. B. & Kim, Y. Challenges for rechargeable Li batteries. *Chem. Mater.* **22**, 587–603 (2010).
- [6] Lou, X. *et al.* Crystal structure modification enhanced FeNb₁₁O₂₉ anodes for Lithium-ion batteries. *ChemElectroChem* **4**, 3171–3180 (2017).
- [7] Zhao, X.-C. *et al.* Enhanced electrochemical performance of Cu²⁺ doped TiO₂ nanoparticles for lithium-ion battery. *ES Mater. Manuf.* **1**, 67–71 (2018).
- [8] Lin, C. *et al.* Nano-TiNb₂O₇/carbon nanotubes composite anode for enhanced lithium-ion storage. *Electrochim. Acta* **260**, 65–72 (2018).
- [9] Tian, J. *et al.* Bio-template synthesized NiO/C hollow microspheres with enhanced Li-ion battery electrochemical performance. *Electrochim. Acta* **261**, 236–245 (2018).
- [10] Pang, Q., Liang, X., Kwok, C. Y. & Nazar, L. F. Advances in lithium-sulfur batteries based on multifunctional cathodes and electrolytes. *Nat. Energy* **1**, 1–11 (2016).
- [11] Bruce, P. G., Freunberger, S. A., Hardwick, L. J. & Tarascon, J.-M. Li–O₂ and Li–S batteries with high energy storage. *Nat. Mater.* **11**, 172–172 (2011).
- [12] Wang, H. *et al.* Graphene-wrapped sulfur particles as a rechargeable lithium-sulfur battery cathode

material with high capacity and cycling stability. *Nano Lett.* **11**, 2644–2647 (2011).

[13] Yang, Y., Zheng, G. & Cui, Y. Nanostructured sulfur cathodes. *Chem. Soc. Rev.* **42**, 3018–3032 (2013).

[14] Wild, M. *et al.* Lithium sulfur batteries, a mechanistic review. *Energy Environ. Sci.* **8**, 3477–3494 (2015).

[15] Manthiram, A., Fu, Y., Chung, S., Zu, C. & Su, Y. Rechargeable lithium – sulfur batteries. *Chem. Rev.* **114**, 11751–87 (2014).

[16] Zhang, Y. *et al.* Highly efficient Fe-N-C nanoparticles modified porous graphene composites for oxygen reduction reaction. *J. Electrochem. Soc.* **165**, H510–H516 (2018).

[17] Luo, Q. *et al.* Carbon nanotube based inverted flexible perovskite solar cells with all-inorganic charge contacts. *Adv. Funct. Mater.* **27**, 1–8 (2017).

[18] Kirubasankar, B. *et al.* In situ grown nickel selenide on graphene nanohybrid electrodes for high energy density asymmetric supercapacitors. *Nanoscale* **10**, 20414–20425 (2018).

[19] Luo, Q. *et al.* All-carbon-electrode-based durable flexible perovskite solar cells. *Adv. Funct. Mater.* **28**, 1–8 (2018).

[20] Liu, T. *et al.* A graphene quantum dot decorated SrRuO₃ mesoporous film as an efficient counter electrode for high-performance dye-sensitized solar cells. *J. Mater. Chem. A* **5**, 17848–17855 (2017).

[21] Liu, H. *et al.* Lightweight conductive graphene/thermoplastic polyurethane foams with ultrahigh compressibility for piezoresistive sensing. *J. Mater. Chem. C* **5**, 73–83 (2017).

[22] Liu, H. *et al.* Electrically conductive thermoplastic elastomer nanocomposites at ultralow graphene loading levels for strain sensor applications. *J. Mater. Chem. C* **4**, 157–166 (2015).

[23] Gao, Z., Zhang, Y. Y., Song, N. N. & Li, X. D. Towards flexible lithium-sulfur battery from natural cotton textile. *Electrochim. Acta* **246**, 507–516 (2017).

- [24] Guo, J., Xu, Y. & Wang, C. Sulfur-impregnated disordered carbon nanotubes cathode for lithium sulfur batteries. *Nano Lett.* 4288–4294 (2011).
- [25] Zhao, Y. *et al.* Self-adaptive strain-relaxation optimization for high-energy lithium storage material through crumpling of graphene. *Nat. Commun.* **5**, 1–8 (2014).
- [26] Zhang, Y. Y., Heim, F. M., Song, N. N., Bartlett, J. L. & Li, X. D. New insights into mossy Li induced anode degradation and its formation mechanism in Li-S batteries. *ACS Energy Lett.* **2**, 2696–2705 (2017).
- [27] Zhang, Y. Y., Gao, Z. & Li, X. D. Capillarity composited recycled paper/graphene scaffold for lithium-sulfur batteries with enhanced capacity and extended lifespan. *Small* **1701927**, 1–12 (2017).
- [28] Wei Seh, Z. *et al.* Sulphur-TiO₂ yolk-shell nanoarchitecture with internal void space for long-cycle lithium-sulphur batteries. *Nat. Commun.* **4**, 1331 (2013).
- [29] Pang, Q., Kundu, D., Cuisinier, M. & Nazar, L. F. Surface-enhanced redox chemistry of polysulphides on a metallic and polar host for lithium-sulphur batteries. *Nat. Commun.* **5**, 4759 (2014).
- [30] Wang, X. *et al.* Structural and chemical synergistic encapsulation of polysulfides enables ultralong-life lithium–sulfur batteries. *Energy Environ. Sci.* **9**, 2533–2538 (2016).
- [31] Xia, X. *et al.* Tubular TiC fibre nanostructures as supercapacitor electrode materials with stable cycling life and wide-temperature performance. *Energy Environ. Sci.* **8**, 1559–1568 (2015).
- [32] Lee, J. T. *et al.* Sulfur-infiltrated micro- and mesoporous silicon carbide-derived carbon cathode for high-performance lithium sulfur batteries. *Adv. Mater.* **25**, 4573–4579 (2013).
- [33] Lazzari, R., Vast, N., Besson, J. M., Baroni, S. & Dal Corso, A. Atomic structure and vibrational properties of icosahedral B₄C boron carbide. *Phys. Rev. Lett.* **83**, 3230–3233 (1999).
- [34] Gu, Y., Chen, L., Qian, Y., Zhang, W. & Ma, J. Synthesis of nanocrystalline boron carbide via a solvothermal reduction of CCl₄ in the presence of amorphous boron powder. *J. Am. Ceram. Soc.* **88**, 225–227 (2005).
- [35] Tao, X. Y. *et al.* Internal electron tunneling enabled ultrasensitive position/force peapod sensors.

Nano Lett. **15**, 7281-7287 (2015).

[36] Song, S. *et al.* B₄C as a stable non-carbon-based oxygen electrode material for lithium-oxygen batteries. *Nano Energy* **33**, 195–204 (2017).

[37] Grubb, W. T. & Mckee, D. W. Boron carbide, a new substrate for fuel cell electrocatalysts. *Nature* **210**, 192–194 (1966).

[38] Kuzubov, A. A. *et al.* High-capacity electrode material BC₃ for lithium batteries proposed by ab initio simulations. *Phys. Rev. B* **85**, 55–58 (2012).

[39] Minakshi, M., Blackford, M. G., Thorogood, G. J. & Issa, T. B. The effect of B₄C addition to MnO₂ in a cathode material for battery applications. *Electrochim. Acta* **55**, 1028–1033 (2010).

[40] Chen, X. *et al.* Conductive rigid skeleton supported silicon as high-performance Li-Ion battery anodes. *Nano Lett.* **12**, 4124–4130 (2012).

[41] Luo, L., Chung, S. H., Yaghoobnejad Asl, H. & Manthiram, A. Long-life lithium–sulfur batteries with a bifunctional cathode substrate configured with boron carbide nanowires. *Advanced Materials* **30**, (2018).

[42] Wagner, R. S. & Ellis, W. C. Vapor-liquid-solid mechanism of single crystal growth. *Appl. Phys. Lett.* **4**, 89–90 (1964).

[43] Tao, X. Y. *et al.* B₄C-nanowires/carbon-microfiber hybrid structures and composites from cotton T-shirts. *Adv. Mater.* **22**, 2055–2059 (2010).

[44] Song, N. N. & Li, X. D. Unveiling polytype transformation assisted growth mechanism in boron carbide nanowires. *J. Cryst. Growth* **481**, 11–17 (2018).

[45] Hummers, W. S. & Offeman, R. E. Preparation of Graphitic oxide. *J. Am. Chem. Soc.* **80**, 1339 (1958).

[46] Hong, N., Langell, M. A., Liu, J., Kizilkaya, O. & Adenwalla, S. Ni doping of semiconducting boron carbide. *J. Appl. Phys.* **107**, (2010).

- [47] Kolel-Veetil, M. K. *et al.* Substitution of silicon within the rhombohedral boron carbide (B₄C) crystal lattice through high-energy ball-milling. *J. Mater. Chem. C* **3**, 11705–11716 (2015).
- [48] Zu, C. & Manthiram, A. Hydroxylated graphene-sulfur nanocomposites for high-rate lithium-sulfur batteries. *Adv. Energy Mater.* **3**, 1008–1012 (2013).
- [49] Ji, L. *et al.* Graphene oxide as a sulfur immobilizer in high performance lithium/sulfur cells. *J. Am. Chem. Soc.* **133**, 18522–18525 (2011).
- [50] Tallant, D. R., Aselage, T. L., Campbell, A. N. & Emin, D. Boron carbide structure by Raman spectroscopy. *Phys. Rev. B* **40**, 5649–5656 (1989).
- [51] Wang, Z. *et al.* Enhancing lithium-sulphur battery performance by strongly binding the discharge products on amino-functionalized reduced graphene oxide. *Nat. Commun.* **5**, 1–8 (2014).
- [52] Shim, J., Striebel, K. A. & Cairns, E. J. The Lithium/sulfur rechargeable cell. *J. Electrochem. Soc.* **149**, A1321 (2002).
- [53] Elazari, R., Salitra, G., Garsuch, A., Panchenko, A. & Aurbach, D. Sulfur-impregnated activated carbon fiber cloth as a binder-free cathode for rechargeable Li-S batteries. *Adv. Mater.* **23**, 5641–5644 (2011).
- [54] Plimpton, S. Fast parallel algorithms for short-range molecular dynamics. *J. Comput. Phys.* **117**, 1–19 (1995).
- [55] Clark, S. J. *et al.* First principles methods using CASTEP. *Zeitschrift für Krist.* **220**, 567–570 (2005).
- [56] Dugan, N. & Erkoç, Ş. Structural properties of boron carbide nanoparticles: Application of a new set of Stillinger–Weber parameters. *Comput. Mater. Sci.* **50**, 2950–2954 (2011).
- [57] Stuart, S. J., Tutein, A. B. & Harrison, J. A. A reactive potential for hydrocarbons with intermolecular interactions. *J. Chem. Phys.* **112**, 6472–6486 (2000).
- [58] Van Duin, A. C. T., Dasgupta, S., Lorant, F. & Goddard, W. A. ReaxFF: A reactive force field for hydrocarbons. *J. Phys. Chem. A* **105**, 9396–9409 (2001).

- [59] Islam, M. M. *et al.* ReaxFF molecular dynamics simulations on lithiated sulfur cathode materials. *Phys. Chem. Chem. Phys.* **17**, 3383–3393 (2015).
- [60] MacKerell, A. D. *et al.* All-atom empirical potential for molecular modeling and dynamics studies of proteins. *J. Phys. Chem. B* **102**, 3586–3616 (1998).
- [61] Yu, C. H., Cukierman, S. & Pomès, R. Theoretical study of the structure and dynamic fluctuations of dioxolane-linked gramicidin channels. *Biophys. J.* **84**, 816–831 (2003).
- [62] Cinacchi, G., Ingrosso, F. & Tani, A. Solvation dynamics by computer simulation: Coumarin C153 in 1,4-dioxane. *J. Phys. Chem. B* **110**, 13633–13641 (2006).
- [63] Smith, G. D. & Jaffe, R. L. A force field for simulations of 1,2-dimethoxyethane and poly(oxyethylene) based upon ab initio electronic structure calculations on model molecules. *J. Phys. Chem* **97**, 12752–12759 (1993).
- [64] Lu, Y. C., He, Q. & Gasteiger, H. A. Probing the lithium-sulfur redox reactions: A rotating-ring disk electrode study. *J. Phys. Chem. C* **118**, 5733–5741 (2014).
- [65] Fan, F. Y., Carter, W. C. & Chiang, Y.-M. Mechanism and kinetics of Li₂S precipitation in lithium-sulfur batteries. *Adv. Mater.* **27**, 5203–5209 (2015).
- [66] Oliver, W. C. & Pharr, G. M. An improved technique for determining hardness and elastic modulus using load and displacement sensing indentation experiments. *J. Mater. Res.* **7**, 1564–1583 (1992).

Chapter 6 Summary and suggestions

6.1 Summary of contributions and significance

In this dissertation, the growth mechanisms, properties, and applications of biomass-derived boron carbide nanowires were systematically studied. The research tasks are listed as follows: (1) investigate the mass transportation process during the boron carbide nanowire growth by coupled experimental characterization and theoretical analysis with the goal to explain the growth mechanisms; (2) develop and simplify the synthesis processes of boron carbide nanowires; (3) explore low-cost biomass as raw materials for boron carbide nanowire production; (4) edit the surface of boron carbide nanowires using graphene sheets for various applications; (5) design and fabricate multiscale boron carbide fillers to reinforce polymers; (6) construct boron carbide nanoskeleton enabled flexible Li-S batteries.

In Chapter 2, a polytype transformation assisted growth mechanism was proposed to explain boron carbide nanowire growth. The growth mechanisms of boron carbide nanowires remain, to a large extent, unknown due to the complex crystal structure and widely varied composition. The density functional theory (DFT) calculations were performed to calculate the formation enthalpies and lattice parameters of polytypic boron carbide. Then the lattice strain fields induced by boron carbide stoichiometry were measured via coupled high-resolution transmission electron microscopy (HRTEM) and digital image correlation (DIC) methodology. The energy barriers to boron migration along the nanowire were obtained by the Nudged Elastic Band (NEB) method to study the mass transportation process during the boron carbide nanowire growth. Based on the DFT calculations and the experimental observations, it is proposed that boron migration in the nanowire growth is realized via polytype transformation assisted

volume diffusion. Furthermore, to better describe the growth process of nanowires, a theoretical model of mass transport was established. The as-calculated growth rate is consistent with the experimental results. Guided by the boron carbide nanowire growth mechanisms, more biomass materials, such as cotton, flour, corn silk, fallen leaf, and paper towel were explored to reduce the nanowire production cost and achieve at scale production.

In Chapter 3, graphene sheets were utilized to tailor the interface between B₄C nanowire and epoxy. The graphene wrapped B₄C nanowires (graphene@B₄C-NWs) were directly synthesized by shear mixing the mixture of graphite powders and B₄C nanowires in dilute water. The as-obtained graphene@B₄C-NW suspension exhibited homogeneous dispersion in both water and epoxy, and enhanced load transfer efficiency from the matrix to reinforcements, leading to the overall improved mechanical performance of the composites. In addition, graphene@B₄C-NWs enabled hybrid toughening effects in the epoxy matrix via crack pinning and deflection, debonding of graphene@B₄C-NWs from matrix, void formation around the nano-fillers, and nano-filler pull-out. The 0.2 vol% graphene@B₄C-NW composite exhibited an exceptional combination of mechanical properties in terms of flexural strength (144.2 MPa), elastic modulus (3.5 GPa), and fracture strain (15.0%).

In Chapter 4, inspired by biological materials, lightweight yet strong and tough boron carbide reinforced epoxy composites were produced. Biological materials, like nacre, often possess superlative properties which are still beyond the reach of man-made materials. One reason is that nature employs multiple multiscale reinforcing principles in nacre to achieve such exceptional mechanical prowess. The micro reinforcements (the aragonite bricks) act as in-plane load carriers while the nano-reinforcements

(the nanoasperities/nanobridges on nacre's brick surfaces) lift the out-of-plane performance. Such hierarchical architecture facilitates the filler/matrix interfacial load transfer. However, the development of engineering biomimetic composites has been largely hampered by the lack of micro/nano hybrid reinforcements. Simultaneously adding both micro- and nano-reinforcements in a matrix material remains challenging since nano-fillers tend to loosely adhere (agglomerate) onto micro-fillers, decreasing their reinforcing effects. In this chapter, under the guidance of the nanowire growth mechanisms, boron carbide micro/nano-fillers (boron carbide nanowires radially aligned on the microplatelets) were designed and synthesized to mimic the exceptional mechanical performance of biological materials. Epoxy composites reinforced by multiscale hybrid boron carbide fillers (functionalized by PANI) were fabricated and characterized by scanning electron microscopy (SEM) and digital image correlation (DIC). The composites exhibited an exceptional combination of mechanical properties in terms of elastic modulus (~ 3.47 GPa), toughness (2026.3 kJ/m³), and fracture strain ($>3.6\%$). Furthermore, an analytical model was built to explain the multiscale reinforcing effects of boron carbide in polymer matrix.

In Chapter 5, boron carbide nanoskeleton enabled, flexible lithium-sulfur batteries were fabricated and characterized, extending the applications of boron carbide nanowires to the field of energy storage. Lithium-sulfur (Li-S) battery is now considered as one of the most promising energy storage devices for electric vehicles, portable electronics, and even grid-scale storage devices. Coupling with lithium metal, the assembled Li-S battery has a specific energy of 2600 W h/kg, which is more than five times higher than that of state-of-the-art lithium-ion batteries. Despite the obvious advantages of Li-S batteries, many challenges need to be addressed before practical implementation, by and large, due to severe capacity

decay, poor cycle life, low utilization of sulfur, and bad coulombic efficiency. Boron carbide with exceptional properties is a promising electrode material for batteries to increase the sulfur utilization, immobilize polysulfides, and enhance battery's structural stability. In this chapter, we demonstrated a flexible, free-standing cathode for Li-S batteries with the flexible activated cotton textile (ACT) cloth as the substrate, boron carbide nanowires as the skeleton, reduced graphene oxide (rGO) as the protective skin. The as-obtained composite (BC-NWs@ACT/S/rGO) was employed as a 3D conductive host for sulfur. The BC-NW@ACT/S/rGO cathode demonstrated the combined advantages of ACT, boron carbide nanowires and rGO, and yielded a significant improvement, in terms of high specific capacity (the initial discharge capacity was 963 mAh/g and after 50 cycles increased to 1395 mAh/g at a high current density of 1.5 mA/cm²), superior cycling stability (over 1000 cycles), ultralow capacity decay rate (0.056% per cycle) and excellent rate capability (current density from 0.1 to 1.2 mA/cm²). The excellent electrochemical performance of BC-NWs@ACT/S/rGO cell was primarily attributed to the outstanding mechanical properties of boron carbide skeleton, the self-adaptive capability to volume variations of rGO skin, and their synergistic effects on the suppression of polysulfide diffusion.

6.2 Suggestions for future research

6.2.1 How does boron carbide transform from brittle materials to ductile ones when reducing the size to nanoscale?

Bulk boron carbide materials are essentially brittle. Many efforts have been focused on studying the failure mechanisms of boron carbide. Bourne [1] reported that during uniaxial compressive shock-loading, boron carbide, a polycrystalline ceramic, showed a behavior similar to an amorphous glass.

Chen *et al.* [2] revealed that nanoscale intragranular amorphous bands were generated in shock-loaded boron carbide by high-resolution electron microscopy observation, which decreased the ballistic performance of boron carbide. Reddy *et al.* [3] characterized the atomic structure of the amorphous shear bands in boron carbide by state-of-the-art aberration-corrected transmission electron microscopy, and provided direct experimental evidence that the formation of amorphous shear bands in boron carbide results from the disassembly of the icosahedra, driven by shear stresses. Fanchini *et al.* [4] used Gibbs free-energy calculations based on density functional theory to determine the possible source of glasslike failure of boron carbide at lower than expected impact pressures. It was proposed that the origin of amorphous bands that accompany the collapse of the structure was the occurrence of the B₁₂(CCC) polytype. In addition, the amorphization transition in boron carbide under compression and shear loading was simulated by the first-principle calculations and large-scale molecular dynamics [5-7].

Unlike bulk materials, boron carbide nanowires possess ductile properties, as reported in Ref. [8-10]. Why does boron carbide behave so differently at different scales? Based on the abovementioned studies of bulk boron carbide, the size effect on the mechanical performance of boron carbide can be investigated via both experimental observation and theoretical simulations.

6.2.2 Explore various applications of boron carbide nanowires

In this dissertation, boron carbide nanowire reinforced polymer composites have been systematically studied. Other matrix materials such as metals and ceramics should be explored for boron carbide reinforced composites. The interaction between boron carbide nanowires with different matrix materials needs to be investigated, in order to better utilize the outstanding mechanical properties of

boron carbide nanowires. In addition, boron carbide nanowires can be applied in the composites together with other nano-reinforcements, like graphene.

Boron carbide nanowires have been successfully applied in lithium-oxygen batteries [11] and lithium-sulfur batteries [12,13], due to their large surface area, efficient catalytic activity, polysulfide absorption ability, and exceptional mechanical performance. With these eminent properties, boron carbide nanowires open up unprecedented opportunities for energy storage applications. For example, it is worthy studying boron carbide nanowire enabled supercapacitors.

Reference

- [1] Bourne, N. K. Shock-induced brittle failure of boron carbide. *Proc. R. Soc. A Math. Phys. Eng. Sci.* **458**, 1999–2006 (2002).
- [2] Chen, M., McCauley, J. W. & Hemker, K. J. Shock-induced localized amorphization in boron carbide. *Science* **299**, 1563–1566 (2003).
- [3] Reddy, K. M., Liu, P., Hirata, A., Fujita, T. & Chen, M. W. Atomic structure of amorphous shear bands in boron carbide. *Nat. Commun.* **4**, (2013).
- [4] Fanchini, G., McCauley, J. W. & Chhowalla, M. Behavior of disordered boron carbide under stress. *Phys. Rev. Lett.* **97**, 1–4 (2006).
- [5] Aryal, S., Rulis, P. & Ching, W. Y. Mechanism for amorphization of boron carbide B₄C under uniaxial compression. *Phys. Rev. B - Condens. Matter Mater. Phys.* **84**, 1–12 (2011).
- [6] An, Q., Goddard, W. & Cheng, T. Atomistic explanation of shear-induced amorphous band formation in boron carbide. *Phys. Rev. Lett.* **113**, 1–5 (2014).
- [7] An, Q. & Goddard, W. A. Atomistic Origin of Brittle Failure of Boron Carbide from Large-Scale Reactive Dynamics Simulations: Suggestions toward Improved Ductility. *Phys. Rev. Lett.* **115**, 105501 (2015).
- [8] Tao, X. *et al.* B₄C-nanowires/carbon-microfiber hybrid structures and composites from cotton T-shirts. *Adv. Mater.* **22**, 2055–2059 (2010).
- [9] Tao, X. *et al.* Internal electron tunneling enabled ultrasensitive position/force peapod sensors. *Nano Lett.* **15**, 7281–7287 (2015).
- [10] Huang, Y. *et al.* Fabrication of patterned boron carbide nanowires and their electrical, field emission, and flexibility properties. *Nano Res.* **5**, 896–902 (2012).
- [11] Luo, W. Bin, Chou, S. L., Wang, J. Z. & Liu, H. K. A B₄C nanowire and carbon nanotube composite

as a novel bifunctional electrocatalyst for high energy lithium oxygen batteries. *J. Mater. Chem. A* **3**, 18395–18399 (2015).

[12] Luo, L., Chung, S. H., Yaghoobnejad Asl, H. & Manthiram, A. Long-life lithium–sulfur batteries with a bifunctional cathode substrate configured with boron carbide nanowires. *Advanced Materials* **30**, (2018).

[13] Song, N. N., Gao, Z., Zhang, Y. Y. & Li, X. D. B₄C nanoskeleton enabled, flexible lithium-sulfur batteries. *Nano Energy* **58**, 30–39 (2019).